PROGRESS TOWARDS A PRECISION MEASUREMENT OF THE NUCLEAR ANAPOLE MOMENT IN CESIUM

by

Amy Damitz

A Dissertation

Submitted to the Faculty of Purdue University

In Partial Fulfillment of the Requirements for the degree of

Doctor of Philosophy

Department of Physics and Astronomy

West Lafayette, Indiana

May 2024

THE PURDUE UNIVERSITY GRADUATE SCHOOL
STATEMENT OF COMMITTEE APPROVAL

Dr. Daniel S. Elliott, Chair

Department of Physics and Astronomy and the School of Electrical and Computer Engineering

Dr. Francis Robicheaux

Department of Physics and Astronomy

Dr. Andrew Mugler

University of Pittsburgh: Department of Physics and Astronomy

Dr. Chen-Lung Hung

Department of Physics and Astronomy

Approved by:

Dr. Csathy Gabor

To Sephy.

ACKNOWLEDGMENTS

I am grateful for the guidance from Professor Elliott to be able to complete this PhD. I am also thankful to the other graduate students I have worked with for their advice and help with work in the lab; George Toh, Jungu Choi, Ian Stevenson, and Jonah Quirk. I acknowledge the machining advice and help from Jim Corwin at the physics machine shop and Randy Replogle from the chemistry precision machine shop that helped me design a machinable rf cavity. They also helped with other machining projects for the lab. I am thankful for my friends who helped give me support and advice over the course of my PhD. I am particularly thankful for my family and Sephy who provided love and support throughout the PhD.

TABLE OF CONTENTS

LIST OF TABLES

LIST OF FIGURES

LIST OF SYMBOLS

E_{pnc}	PNC amplitude
$M1$	magnetic dipole amplitude
Q_W	weak charge
β	vector polarizability
α	scalar polarizability

ABBREVIATIONS

AR coating	anti-reflective coating
ECDL	external cavity diode laser
NAM	nuclear anapole moment
NSD	nuclear spin dependent
NSI	nuclear spin independent
PNC	parity non-conservation
PV	parity violation
PZT	piezo-ceramic element
rf	radio-frequency

ABSTRACT

Parity non-conversation experiments provide a method to explore the weak interaction. Precision measurements of the weak interaction will lead to more limitations on beyond the standard model theories. Our lab will use a two-color coherent control to help us to extract the small amplitude of the weak interaction between the nucleons of the cesium nucleus. In this dissertation, I will discuss how our lab is investigating the anapole moment in cesium using rf and laser fields, along with future steps to finish the measurement.

1. INTRODUCTION

1.1 Physics Beyond the Standard Model

The standard model of physics has been very successful at describing our world and predicting the existence of particles that we have subsequently found. It was developed over the mid-1900's through the work of multiple theorists trying to understand the properties behind the weak and strong forces and to form a stronger theoretical picture of these two forces [1]. The final developments of the standard model occurred in the 1970's. They were successful in bridging electromagnetic and weak interactions in the electro-weak interaction. Later they unified the strong interaction to the electro-weak interaction within the framework of the standard model. Currently, unifying gravity into the rest of the fundamental forces, strong, weak, and electromagnetic, has been unsuccessful. The model also predicted a variety of particles, like the Z^0 boson, $W^{\pm}$ bosons, and Higgs Boson, that have not only been found, but their properties have been verified to agree with the model's predictions. Despite the model's many glowing successful answers to how our world works, it still leaves many questions on the table that it has no answers for. For example, the imbalance of matter and anti-matter and our lack of understanding dark matter/energy, are just two of the troubling problems the standard model does not have the answer to [1]–[3].

Theorists have developed a wide range of different theories that could potentially answer some of the remaining questions the standard model has not been able to describe, like different super symmetry theories. So far many of these theories are not widely accepted or verified, though many strides are being taken to test beyond the standard model theories. Additionally, experiments are being conducted to identify where the standard model is inconsistent with our current understanding. Probes at different energy levels are sensitive to different quantities of the standard model and of models beyond the standard model. The Large Hadron Collider (LHC) and other particle colliders are able to probe higher energy levels for new particles or processes. Another route is at lower energies with atomic, molecular, and optical (AMO) methods. These tests are particularly sensitive when looking at effects that violate fundamental symmetries (parity or time symmetry), like those found in the weak interaction. More precise knowledge of the known quantities understood in the

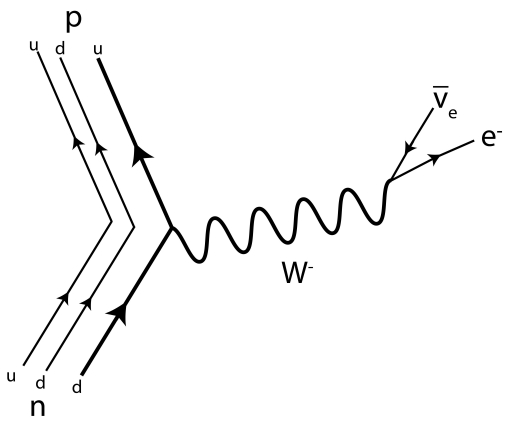

Figure 1.1. Feynman diagram of the beta decay where the down quark becomes a up quark by the W^- mediating boson [3], [9]–[12].

standard model would provide boundaries for new theories. In particular it could place constraints on theories of a massive Z' boson, Z_d boson, a light boson, or searches for potential dark matter candidates [1]–[8].

1.2 Weak Interaction

The idea of a weak interaction was first proposed in 1933 by Enrico Fermi, when he proposed that beta decay could be explained by a four-fermion interaction using a contact force with very short-range [9]. We now know beta decay, as shown in Fig. 1.1, is when an up quark turns into a down quark or vice versa. This ends up with a neutron transforming into a proton by emission of an electron and anti-neutrino or a proton transforming into a neutron by emission of a positron and neutrino. The weak interaction is mediated through an exchange of a Z^0 or $W^{\pm}$ boson. The $W^{\pm}$ boson mediates a charged-current interaction, where the interacting particle changes identity, like the proton turning into a neutron. The Z^0 boson has no charge, only allowing the interacting particles to exchange momentum, spin, and energy, mediating a neutral current where the interacting particle retains the same identity [3], [9]–[12].

The Z^0 boson signature was first discovered experimentally in 1973 at CERN [13], at the Gargamelle Bubble Chamber. The Gargamelle Bubble Chamber held 1000 tons of heavy-liquid freon. It was placed in the path of CERN's muon-neutrino beam, produced by the CERN Proton Synchrotron, where the paths made from neutrino interactions could be observed. Even though the bubble chamber could not create paths of the neutrino's trajectories that we could observe, it was sensitive to the paths of other charged particles that could interact with the neutrino. The experimentalists discovered the first direct evidence for neutral currents when they observed electrons that would seemingly move on their own in the traces, with no other charged particle to explain the movement. This movement was attributed to the interaction of a neutrino and electron by way of a Z^0 boson [13].

It was only in 1983, at CERN's proton-antiproton collider, that direct evidence of the bosons themselves was found and their approximate masses. The weak interaction's mediator bosons are both massive in comparison to the size of a proton, at around 80 to 90 GeV/c^2, in comparison to the protons less than 1 GeV/c^2 mass. The size of the mediator boson limits the distance over which the weak interaction can occur to being less than the diameter of a proton, becoming essentially a contact interaction on atomic scales [3], [9]–[11].

1.3 Parity Violation

Through the first half of the 20^{th} century, physicists believed parity was conserved in each of the fundamental laws of nature, or more simply that the laws did not distinguish between actions that were mirror images of each other (like going left instead of right) [14]. Different quantities transform differently under parity inversion. For a parity-odd quantity, a mirror reflection flips the sign and for a parity-even quantity, a mirror reflection does not change the sign of the quantity. Examples of parity-odd quantities are position, linear momentum, and electric field. Spin and orbital angular momenta along with the magnetic field are parity-even quantities [3], [15].

In the mid-1950's, Chen Ning Yang and Tsung Dao Lee proposed that, unlike the strong, gravity, or electro-magnetic interactions in which parity was conserved, the weak interaction violates this symmetry. This parity violation (PV), or parity non-conservation (PNC), was

posited to mix different parity states for the weak interaction, like in a beta decay or meson and hyperon decay [16]. Madam Chien-Shiung Wu experimentally verified in 1957 that the weak interaction did in fact violate parity through an observation of beta decay in Cobalt-60 [17]. She measured the angular distribution of electrons coming from the beta decay of Cobalt-60. An asymmetry was found in the distribution coming from a mirror-reversed orientation of the nuclear spin of the parent nucleus of Cobalt and the momentum of the electron, providing unequivocal proof that parity is not conserved in beta decay [17]. After Madam Wu's discovery, the Nobel Prize in physics was awarded to Yang and Lee in 1957.

Initially, the weak interaction was determined to not be strong enough to be observable in experiments in atomic systems, due to the knowledge that its effects were weak in comparison to the electro-magnetic effects at the scales of investigation. In addition, only the $W^{\pm}$ bosons were understood to mediate the weak interaction at this time. A $W^{\pm}$ exchange in the atom would not cause a steady-state modification, but instead would cause a decay of the nucleus, changing the atom into a different species. When the Weinberg-Salam-Glashow theory was proposed in the 1960's, they predicted another mediating boson of the weak force, the Z^0 boson, which was neutral. The Z^0 boson's neutral current would just modify the electronic wave function of the atom and not change the atomic species like the $W^{\pm}$ bosons [1], [18].

PNC effects that could be observed in atoms would be a useful tool to probe the weak force in atoms. This is mainly due to the fact that the other three fundamental forces are known to not violate parity, so any PNC effect would solely be due to the weak force. Additionally in atoms, the electric dipole transitions between states with the same parity (like 6s to 7s transition in cesium) are forbidden by the electromagnetic interaction. With the weak force in play, the same parity states in the atom are mixed with the opposite parity state (in the 6s to 7s transition in cesium, the mixing of s and p states is on the order of 10^{-11}), and the transition between the same parity states becomes slightly allowed as an electric dipole transition. Therefore any atom undergoing an electric dipole transition between same parity states would be due to the weak interaction (there are other interactions that can drive the transition, but they can be weakened). Though, due to the size of the Z^0 boson causing the weak interaction to be contact-like, this means that only electronic states that overlap with the nucleus will be affected by the electron-nucleon weak force [1], [3], [18]–[21].

Precision measurements of parity violation in atoms allow us to determine the weak charge, Q_w, of the nucleus of different atoms. Q_W of the atom is the sum of the weak charges of all the constituents of the neutrons and protons in the atomic nucleus, the up and down quarks. The equation is in the form of, $Q_W = (2Z + N)Q_W(u) + (Z + 2N)Q_W(d)$, where N is the number of neutrons in the nucleus, Z is the number of protons in the nucleus, $Q_W(u)$ is the weak charge of the up quark (coupling of the electron axial-vector currents to the up quark-vector currents), and $Q_W(d)$ is the weak charge of the down quark (coupling of the electron axial-vector currents to the down quark-vector currents). Then with the weak charge known, one is able to obtain the electro-weak mixing angle θ_W from the relationship of $Q_W \approx -N + Z(1 - 4sin^2(\theta_W))$. Obtaining a precise value would lead to being able to place bounds on the standard model of physics and models beyond the standard model. In addition, the measurement in atoms would be at lower energies than those found at particle accelerators that are also trying to measure the electro-weak mixing angle. Over different energy scales, the standard model has predicted variation of the weak mixing angle as seen in Fig. 1.2 and Fig. 1.3 [1], [3], [18]–[21]. Fig. 1.3 is a more recent version of Fig. 1.2, illustrating the effort over 4 years of the field to further fill in this picture.

Zeldovich [22] originally brought forth the idea that the PNC effect could be observed in atoms two years after Madam Wu's experiment, but predicted that the effect would be too tiny to observe when he studied the effect in hydrogen. It was in 1974 that Bouchiat and Bouchiat [23] determined that the PNC effect would be amplified in heavy atoms, as the PNC amplitude would scale as roughly Z^3, where Z is the number of protons and thus the nuclear charge. The PNC signal can be further amplified through an interference technique, beating the PNC against a stronger signal. Then the total transition is the sum of the two signals plus an interference term of the two signals multiplied together. The weaker term can be extracted from the interference term which is bigger than just the weaker term. The prediction of Bouchiat and Bouchiat [23] was successfully observed by Novosibirsk's group in 1978, using bismuth as the heavy atom and interference between the PNC signal and the magnetic dipole transition signal. It was followed up in the early 1990's with similar measurements in lead and thallium, both of which have similar masses to bismuth [1], [3], [18]–[20].

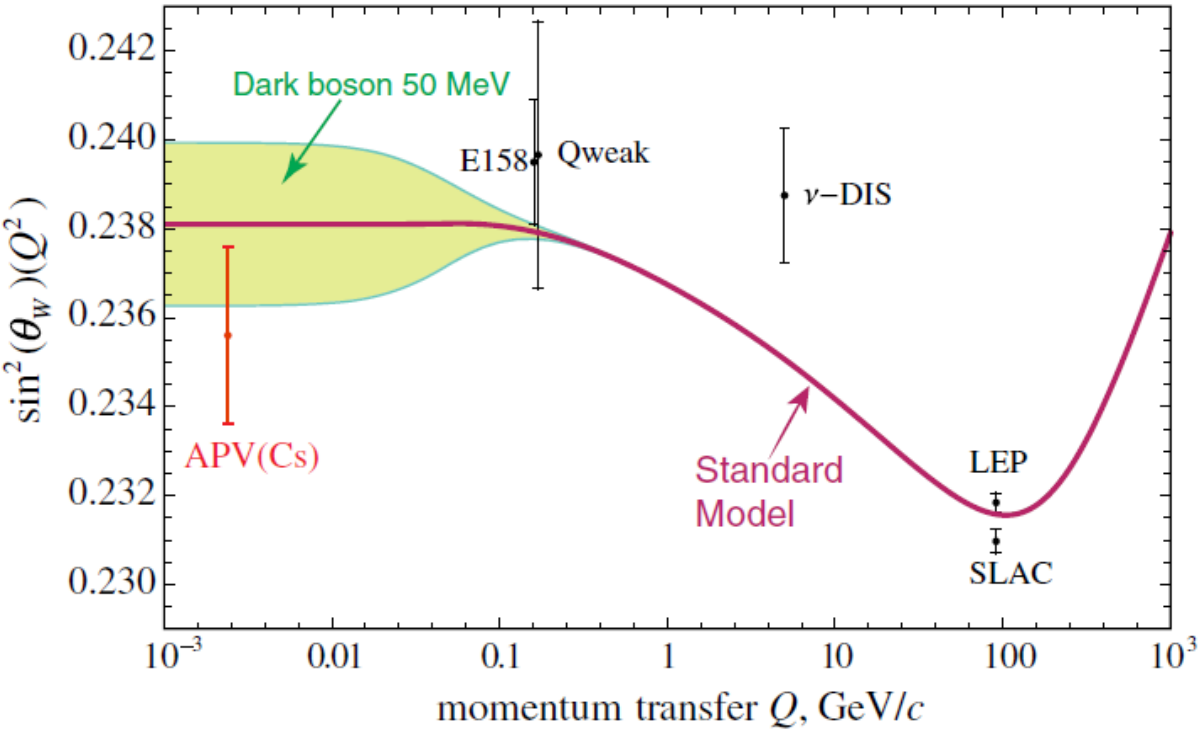

Figure 1.2. A plot of $sin^2(\theta_W)$ vs. collision energy. The data points indicate the results of various measurements that are identified in the figure while the solid line is the standard model. Figure from Ref. [3] from 2018.

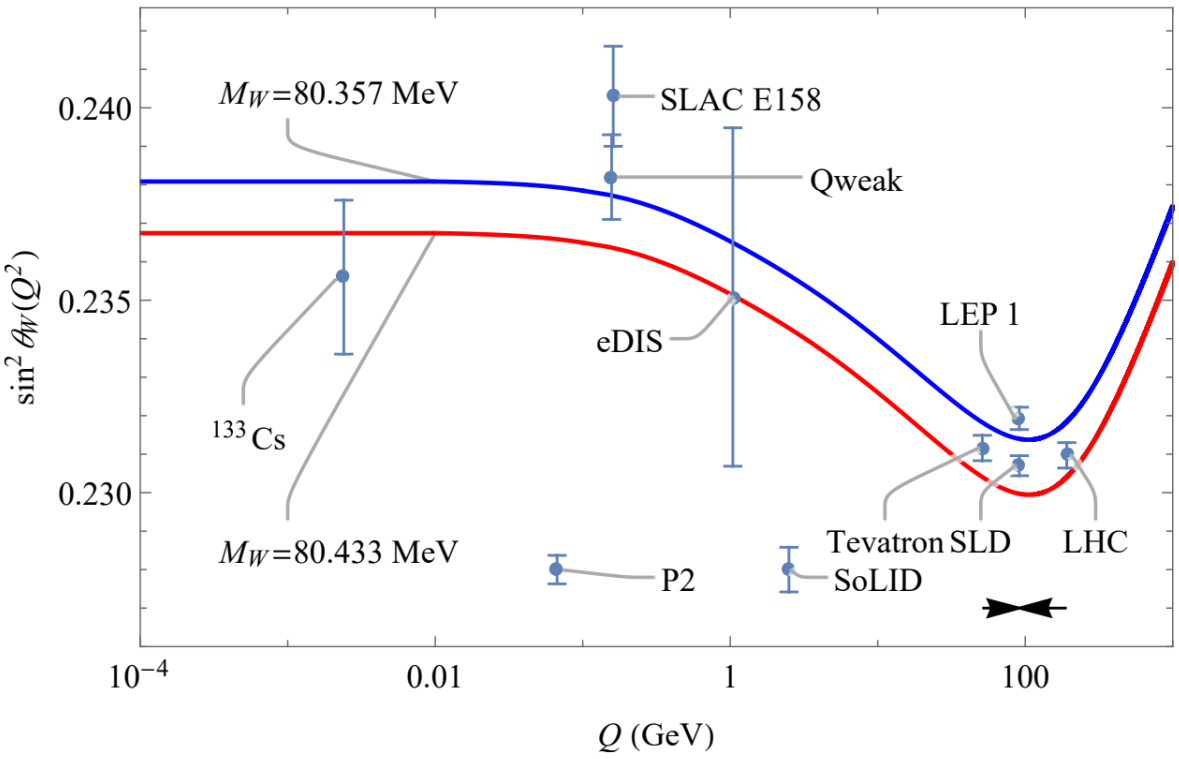

Figure 1.3. A plot of $sin^2(\theta_W)$ vs. collision energy. The data points indicate the results of various measurements that are identified in the figure while the solid line is the standard model. Figure from Ref. [21] from 2022. The red line is the standard model prediction using the new value of the W-boson mass while the blue line is the previous value as seen in Fig. 1.2

Table 1.1. Measurements of E_{PNC} in different atomic systems (with the current lowest experimental uncertainty achieved).

Atom	Ref	Uncertainty	Year
Cesium	[24]	0.35%	1997
Ytterbium	[25]	0.5%	2019
Thallium	[26]	1.1%	1995
Lead	[27]	1.1%	1995
Bismuth	[28]	2%	1991

1.4 Atomic PNC

So far the most accurate PNC amplitude measurement E_{PNC} was performed in cesium in 1997 by Wood, to a 0.35% uncertainty [3], [14]. There are a variety of other measurements to determine E_{PNC} in different atomic systems, seen in Table. 1.1.

While a PNC signal was found in bismuth, lead, and thallium, there is difficulty in extracting different parameters of interest due to the complexity of the atoms, causing difficulties in theory. Theorists have had the most success in understanding the structure of hydrogen and other 'hydrogen-like' atoms in the alkali family, due to the simplicity in the interactions of having only one valence electron. Therefore rubidium, cesium, and francium make attractive candidates to observe a large PNC signal due to their high Z value, and have accurate theory to back it up [3].

1.4.1 Cesium PNC

One of the more important quantities of interest that can be obtained from atomic PNC experiments is the extraction of the weak charge of the atom from E_{PNC}. So far, the weak charge of cesium has been the most precisely measured weak charge of an atom. This is mainly due to cesium's well understood properties, which enable experimental and theoretical values outcomes to be precise. For example the energy levels of cesium found experimentally and theoretically match well, the low level's energies can be seen in Figure 1.4.

The cesium experiment, done by Wood and Wieman in the 1990's, experimentally measured the amplitude of the PNC signal E_{PNC} as the ratio to a known quantity, the vector

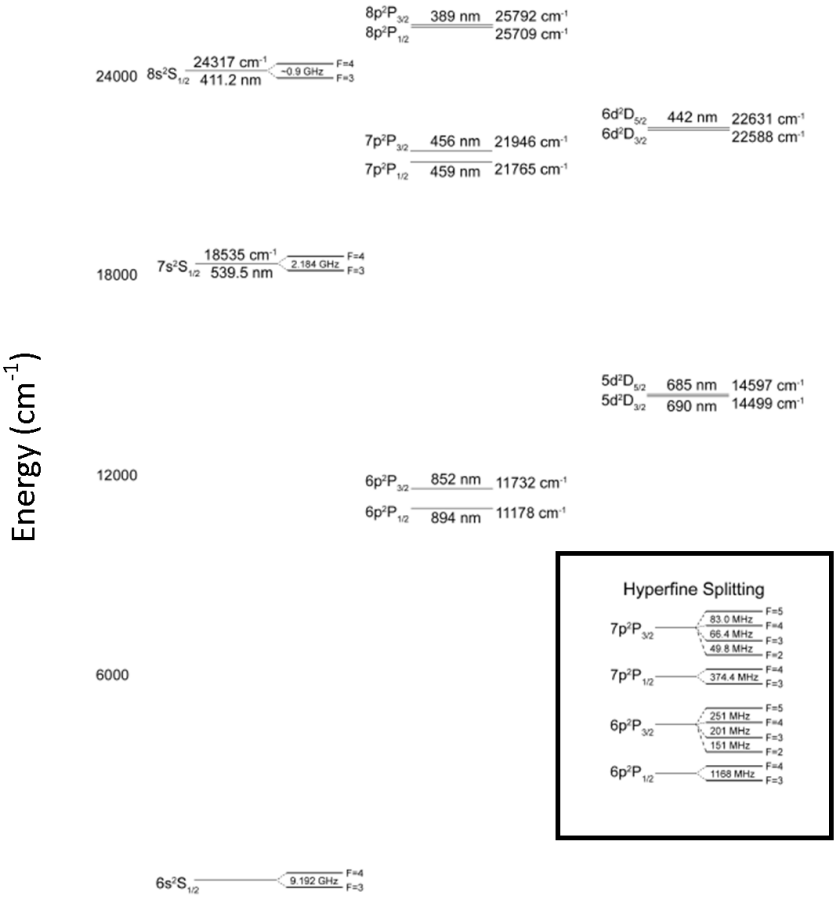

Figure 1.4. Cesium energy levels showing the lowest energy levels of Cs-133. Numbers are from the NIST database [29], except for the hyperfine splitting data, which are from a variety of sources [30]–[36]. The hyperfine splitting of the $6P_j$ and $7P_j$ states are in the lower right corner instead of in the figure due to simplicity. Figure from George Toh's thesis [37].

polarizability of the 6s to 7s transition, β. To extract the E_{PNC} from the experimental quantity, they multiplied by the known quantity β. To determine the weak charge (Q_W) from E_{PNC}, theorists must calculate the ratio of E_{PNC} and Q_W. This is where having a simple atomic structure comes in handy, as theorists are better able to calculate Q_W/E_{PNC} precisely, therefore allowing the extracted Q_W to be more precise. The equation then to extract Q_W is:

$$Q_W = \frac{E_{PNC}}{\beta} * \beta * \frac{Q_W}{E_{PNC}}. \tag{1.1}$$

After Wood's measurement in cesium, the extraction of the weak charge was limited by the uncertainty in the theoretical value of Q_W/E_{PNC}. This spurred theorists to improve their value over the next decade, until their value was as precise as experiment.

Wood's Experimental Details

The process to obtain E_{PNC} is detailed and precise. To get E_{PNC}, Wood used a cesium atomic beam experimental setup, as shown in Fig. 1.5. The atomic beam is useful to be able to pass the atoms through a sequence of actions, while still having a continuous signal. For Wood's experiment, the atomic beam passes through three regions, each with a different purpose. The first region is the preparation region, which uses lasers to optically pump the majority of the atoms into one specific state (F,m), while emptying out each of the other ground hyperfine levels. (F is the quantum number for the total angular momentum of the atomic state and m for the projection of F on the z axis.) The next region is the interaction region, where a resonant laser drives the 6s -> 7s transition via the weak-force induced transition, as well as a Stark-induced transition When the atoms decay from this state there is a fraction that decay to the emptied ground hyperfine level. In the detection region, a probe diode laser probes the once emptied ground hyperfine level, so the amount of signal detected tells us how many atoms were excited in the interaction region. Wood used an interference technique as proposed by Bouchiat, where the E_{PNC} amplitude is interfered

with a Stark amplitude to be able to have a larger signal to measure than just the weak amplitude. The transition rate of interest is:

$$R = \mid A_{PNC} + A_{M1} + A_{Stark} \mid^2 = A_{Stark}^2 + A_{PNC}^2 + 2 * A_{PNC} * A_{Stark}^* + c.c., \tag{1.2}$$

where A_{Stark} is the amplitude of the Stark transition, A_{PNC} is the amplitude of the PNC transition, and A_{M1} is the amplitude of the magnetic dipole transition for the 6s to 7s state. Surrounding the interaction region there are electric field plates that induce a strong A_{Stark} transition that scales with the size of the electric field caused by the field plates. A_{M1} is small due to the change in principal quantum number and by the use of counter-propagating the laser beams. Therefore the transition rate has a strong DC offset from A_{Stark} and the only other significant term is $2 * A_{PNC} * A_{Stark}^*$. During the experiment, Wood reversed the direction of the laser polarization and fields in the interaction region, which causes A_{PNC} to switch signs as parity reverses. Therefore, as the direction reverses there is a modulation on R due to A_{PNC}. Wood was able to very precisely obtain E_{PNC}, but also discovered many new systematic effects and had to characterize and eliminate these systematic errors to isolate the PNC effect [38].

1.4.2 NSI and NSD Contributions to E_{PNC}

Wood et al. [24], [38] measured E_{PNC}/β on two different components of the $6s - 7s$ transition to determine the nuclear spin dependent (NSD) and nuclear spin independent (NSI) components. Wood measured the PNC amplitude on both of the hyperfine changing transitions (6s F=3 to 7s F′=4 and 6s F=4 to 7s F′=3). The average of the two amplitudes is the NSI term, while the difference is the NSD term.

Fig. 1.6 shows the major diagrams that contribute to parity violation in atoms. There is only one nuclear spin independent effect diagram, Fig. 1.6.(a), where a Z^0 boson is exchanged between the electron and nucleus with the nucleon-vector and electron axial-vector currents.

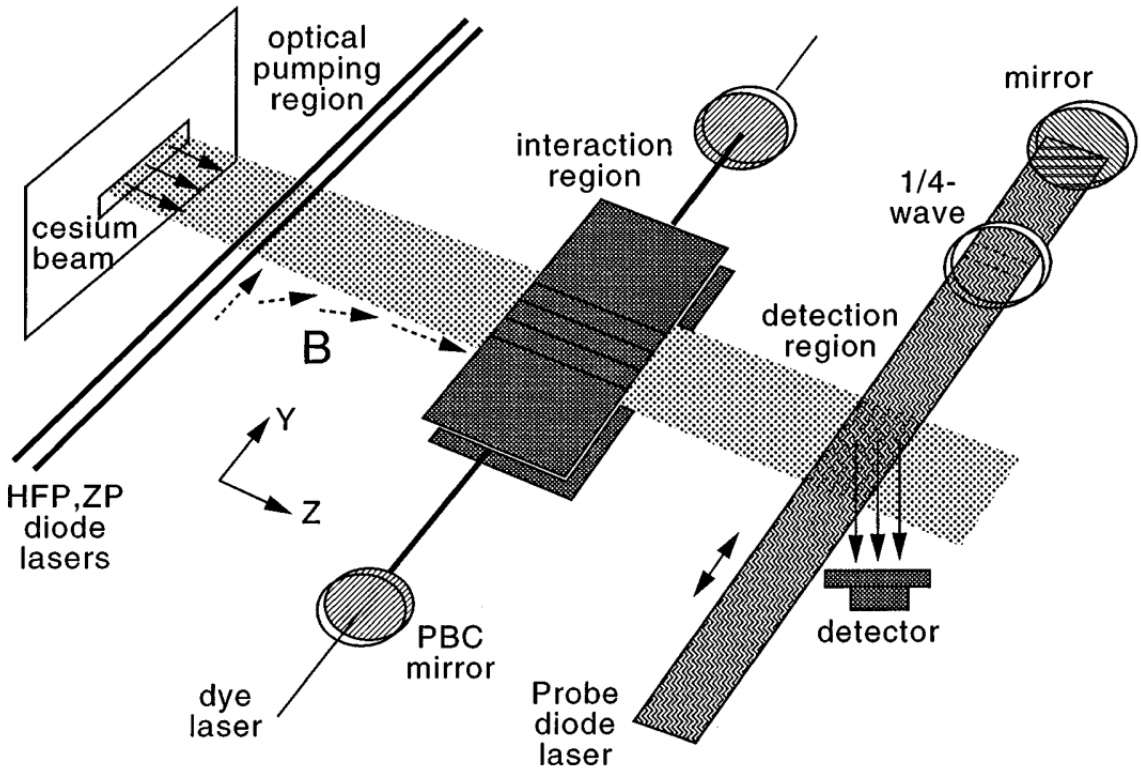

Figure 1.5. The experimental apparatus for Wieman and Wood's PNC experiment from Ref. [38]. The atoms first pass through the optical pumping region which moves a majority of the atoms into one particular state. The interaction region houses a power build up cavity which helps to amplify the PNC amplitude. The detection region houses a detector system that can be used to determine the final state of the atom after the interaction

The NSI diagram is the dominant contribution to the PNC signal in atoms and its effective weak Hamiltonian is

$$H_W = Q_W * \frac{G_F}{\sqrt{8}} * \gamma_5 * \rho(r), \tag{1.3}$$

where G_F is the Fermi constant, γ_5 is a Dirac matrix, and $\rho(r)$ is the nuclear density.

The other three diagrams are due to NSD effects. The two most important NSD effects are due to the anapole moment in Fig. 1.6.(c), that is an electromagnetic interaction whose contribution to the PNC Hamiltonian is

$$H_{NAM} = 1.15 \times 10^{-3} \ * \ \frac{\kappa_N}{I(I+1)} \ \mu_N \ g_N \ A^{2/3} \ * \ \frac{G_F}{\sqrt{2}} \ (\vec{\alpha} \cdot \vec{I} \,) \ \rho(r), \tag{1.4}$$

and a Z^0 boson exchange between electron-vector and nucleon axial-vector currents in Fig. 1.6.(b) whose contribution to the PNC Hamiltonian is

$$H_{axial} = -C_N^{(2)} \ * \ \frac{\kappa_N - 1/2}{I(I+1)} \ * \ \frac{G_F}{\sqrt{2}} \ (\vec{\alpha} \cdot \vec{I} \,) \ \rho(r), \tag{1.5}$$

where I is the nuclear spin of the atom, α is the velocity operator of the atomic electrons, and $\rho(r)$ is the nuclear density [3]. Therefore NSD contributions only occur in atoms whose nuclear spin, I, is not zero. (The nuclear spin on ^{133}Cs is $I = 7/2$.) A is the atomic number and κ_N is the relativistic angular quantum number for the unpaired nucleon that is equal to $(I + 1/2) * (-1)^{I+l+1/2}$, where l is the orbital angular momentum of the atomic state. $C_N^{(2)}$ is the weak interaction coupling constant associated with valance nucleon, and N represents either a p (proton) or n (neutron) depending on the nucleus. μ_N is the magnetic moment of the unpaired nucleon expressed in units of the nuclear magneton and g_N is the weak coupling constant. Experimentally determining this term precisely is of interest to provide a sensitive window into the electron-vector and nucleon axial-vector currents that are typically only studied with deep inelastic scattering. The last diagram in Fig. 1.6.(d), is a combined action of hyperfine interaction and NSI interaction, which is usually dominated by the anapole moment and nucleon axial-vector contributions of the NSD effect. In heavier atoms, the anapole moment in general dominates the nucleon axial-vector, while the nucleon

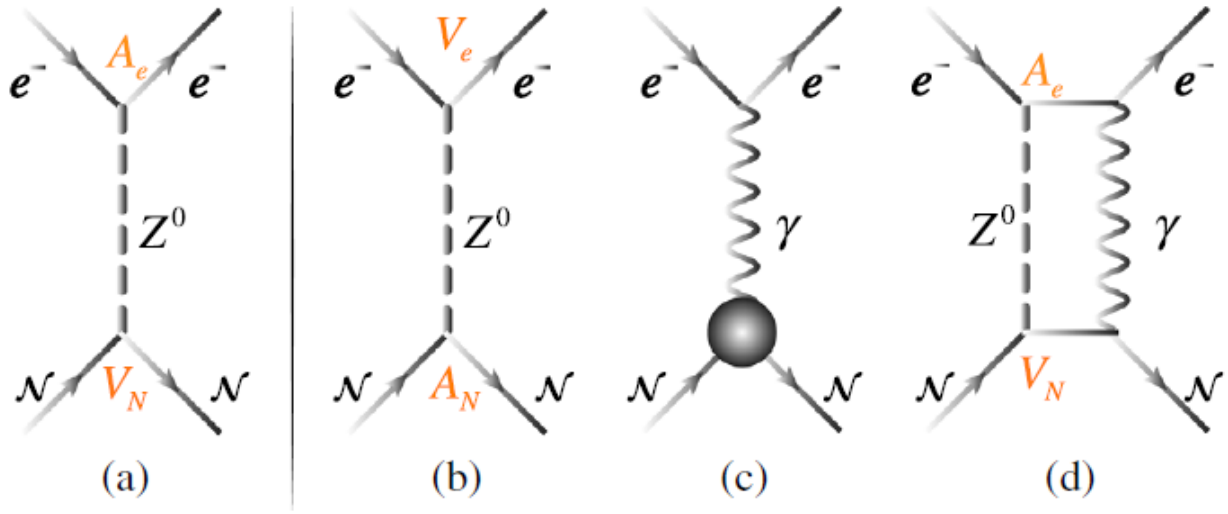

Figure 1.6. From Ref. [3]. These are the four major diagrams involved in the parity violating amplitude in atoms. N is the nucleon, e^- is the atomic electron, A_i is the axial-vector current, and V_i is the vector current, where $i = N$ or e^-. The vertical line between (a) and (b) separates the NSI (a) from the NSD (b), (c), and (d) diagrams. The main diagram of interest for this thesis is (c) where it represents the anapole moment (sphere) electromagnetically interacting with the atomic electrons.

axial vector dominates the anapole moment in lighter atoms, mainly due the $A^{2/3}$ factor in the anapole moment Hamiltonian [3], [14], [38].

Nuclear Anapole Moment

As seen in the equations above, there are different types of interactions that come into play that contribute to the spin dependent effect. There is the axial coefficient that is associated with the exchange of the Z^0 boson from nucleon axial vector currents, the nuclear anapole moment (NAM) that couples the nucleus to the atomic electrons electromagnetically, and the nucleon-vector currents that come from the combined action of the hyperfine and spin-independent Z^0 boson exchange interaction. Cesium is a heavy atom, where the NAM term is the primary contributor to the NSD effect.

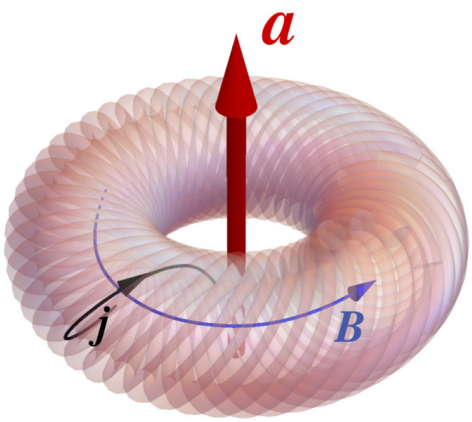

Figure 1.7. A visual representation of the nuclear current distribution that generates the nuclear anapole moment (from Ref. [3]). **a** is the anapole moment, **j** is the current, and **B** is the magnetic field. (The figure shows a corkscrew winding of **j** where it is only the azimuthal component of **j** that generates **a**. The rest of **j** generates the conventional dipolar magnetic field which is not illustrated in the figure.)

The NAM is configured with a toroidal current density, where the current density, **j**, produces the anapole ("up-pole") moment, a, and the magnetic field is contained within the 'toroid' as seen in Figure 1.7. The only electrons that are part of the NAM interaction are in the region of the toroid. The NAM is proportional to the nuclear spin, I, and to the square of the nuclear radius, the nuclear radius is proportional to the atomic number to the one-third power, therefore the NAM is proportional to $A^{2/3}$ as seen in Eq. 1.4. The NAM is due to the nucleon-nucleon interaction and is brought about by a meson exchange. The meson exchange is characterized by one of the nucleon-meson vertices being strong and the other being weak and parity violating. Better understanding of this meson exchange would give us a better understanding of hadronic PNC and thus increase our understanding of the nucleus [3].

The NAM is parity-odd and time-reversal even quantity. Parity-odd is when a mirror reflection flips the sign of the quantity and time-reversal even is when reversing time does not change the quantity (time-reversal odd the quantity will change sign). The NAM cannot be probed by real photons, instead it must be probed through virtual photons, like those

Table 1.2. Anapole moment constant of ^{133}Cs from theoretical calculations. *was derived from the results of Wood et al.'s experiment [24]

Ref	Anapole Moment constant	Year
[39]	0.25	1984
[40]	0.24	1991
[41]	0.33(analytic) 0.26 (numerical)	1994
[42]*	0.364(62)	1997

seen in Fig 1.6 (c). Therefore one cannot measure the NAM with a static electric field, unlike the similar situation of being able to measure a magnetic moment with a static magnetic field [3].

There have been theoretical calculations of the anapole moment constant in cesium, seen in Table 1.2. The final entry in this table was derived from Wood et al.'s experiment, Ref [42]. Wood et al.'s experiment was the first experiment, and so far only, that has been able to extract the anapole moment from the NSD effect with statistical significance in an atom. Additionally, they obtained the meson coupling constants from the anapole term. Interestingly, the extracted meson coupling constants are inconsistent with those derived from high energy scattering experiments. It is therefore of great interest to explore the anapole moment of cesium, and its derived meson coupling constants, to understand why the values are different from all of the other experiment's determinations [3].

1.5 Our Goals

Our group plans to remeasure both the the NSI and NSD components of E_{PNC} on the $6s-7s$ transition in cesium along with an independent measurement of the anapole moment of cesium on the ground state hyperfine transition, $6sF = 3 \longrightarrow 6sF = 4$. I have lead the latter effort.

In the next sections I will discuss the current status of the shared experimental setup for both of the main efforts, along with what has been built up by Dionysis Antypas, George Toh, and Jungu Choi before my involvement. In addition, I will discuss the theory and experimental setup behind the anapole experiment. Finally, I will discuss the details and

results of the anapole moment as of now. In particular, all of the steps done to characterize and minimize the systematics in the system and what is preventing the measurement. To further the experiment, I will also discuss what progress can be done for the anapole moment measurement setup.

2. LABORATORY FACILITIES

Our group has made previous measurements using a two-color coherent control technique [43]–[47]. We were inspired by Wood et al.'s [24], [38] measurement of the weak interaction as another quantity that could benefit from the use of the two-color coherent control technique. Other PNC investigations in different atoms and molecules also drove home the importance of measuring the NSI and NSD effects in atomic and molecular systems precisely. In particular the efforts in francium by the TRIUMF collaboration [48]–[52], efforts in ytterbium [53], and efforts in molecules, particularly $^{138}Ba^{19}F$ [54]–[56]. In particular for cesium, over the years the related theory's uncertainty [57]–[59] has caught up with the uncertainty from Wood et al.'s [24], [38] experiment. To truly benefit from more precise theory and produce more stringent bounds on beyond the standard model physics, a more precise experiment is needed in cesium. Additionally, new efforts into PNC theory have taken place and are sparking more effort and interest into understanding the effect of the PNC amplitude in measurements with atoms [21], [60]–[64], in particular with more efforts into understanding the hyperfine structure and electric dipole moments of atoms of interest [65]–[69]. Our analysis of the experiment, and some related measurements, indicate that the two-color coherent control technique can help improve on the uncertainty from Wood et al.'s [24], [38], and therefore improve the limits that the weak charge in cesium can place on beyond the standard model physics. The two main efforts in our group are to measure the NSI and NSD components of the PNC amplitude of the $6s - 7s$ transition, like Wood et al.'s [24], [38] measurement, and one to solely measure the NSD component on the hyperfine ground state transition (anapole moment). For the particular experiment I have been leading, the anapole moment measurement, Wood et al.'s [24], [38] experiment served as motivation to find another method to obtain the anapole moment in cesium more precisely. This was mainly due to the fact that Wood et al.'s [24], [38] determination of the anapole moment was dependent on a small difference between two large numbers, leading to difficulties on improving the uncertainty to below 10%. Though some of the methods we are planning to use to obtain the anapole moment in cesium have changed, we were motivated by Wood et al.'s [24], [38] methods.

For remeasuring the NSI and NSD components of the PNC amplitude we are planning to use an interference method, similar to that proposed by Bouchiat and Bouchiat [19], [20] and used by Wood et al.'s [24], [38] experiments. The transition probability is

$$R = \mid A_{weak} \pm A_{\mathrm{j}} \mid^2 \approx \mid A_{\mathrm{j}} \mid^2 \pm 2R\mathrm{e}(A_{\mathrm{j}} A^*_{weak}), \tag{2.1}$$

where A_{weak} is the PNC transition amplitude and A_{j} is a strong transition. The choice of A_{j} depends on the necessary interactions for the experiment. For the anapole moment measurement I am leading, we are still using interference to amplify the PNC amplitude but the transition probability equation above does not fully describe the transition rate. This will be discussed further in the next chapter. Both of our labs proposed experiments approaches differ in comparison to Wood et al.'s [24], [38] method by using a two-color coherent control technique. This is unique in that it uses two distinct but mutually-coherent fields to drive the weak interaction (A_{weak}) and the strong interaction (A_{j}). This enables both of the interactions to be driven coherently and thus their interference is coherent. This helps reduce the importance of different systematics faced by Wood et al.'s [24], [38] as we will only need to care about systematics that are at the same rate as the interference. For each of the efforts, we are mainly working towards improving on one of Wood et al. [24], [38] experimental results of the NSI or anapole moment of cesium. Jonah Quirk is leading the improvement of the NSI measurement in cesium, while I have lead the anapole moment measurement.

Over the years, our lab has built up a setup to be able to sensitively use our two-color approach to measure weak amplitudes in cesium. This system has already allowed previous graduate students to measure a weak amplitude using an interference method in our measurement of the magnetic dipole moment (M1) [70].

2.1 General Setup

The setup of our experiment consists of a beam of cesium atoms generated in a vacuum chamber, multiple diode lasers, and a multitude of mirrors and other necessary optics to shape the diode laser beams' specifications.

Our laboratory's vacuum chamber has external magnetic field coils surrounding it. The magnetic field coils are set up to be able to zero the magnetic field due to the Earth in the center of the vacuum chamber. The path of the atom beam in the vacuum chamber first brings the atoms to the preparation region. This prepares the atoms into a specific state by passing lasers through the atom beam. Then the atoms pass through the interaction region for the experiment. The specifics of the setup depend on the which interaction we are interested in studying. Finally, the atoms pass into the detection region, where we can observe the final state of the atoms. We use an atom beam to be able to have a continuous signal in comparison to trapping the atoms.

2.1.1 Atomic Beam Setup

For our experiments, an atom beam geometry is used and set up as later seen in Fig. 2.8. The beam is generated in the vacuum chamber through the use of an oven attached to the side of the vacuum chamber, as seen in Fig. 2.1 and Fig. 2.2. This setup was designed and put into place by a previous graduate student in the lab, Dionysios Antypas.

The main chamber was designed to be able to hold additional magnetic field coils and other equipment that could be necessary for the PNC experiments and other future works. The chamber was made from aluminum to help not introduce stray magnetic fields. For the PNC experiments, the main goal of the group, stray magnetic fields will cause systematic effects that must be minimized. Additionally, there are multiple sets of optical windows on opposite sides of the chamber to allow lasers to go through in both directions. Each set of windows was manufactured with appropriate anti-reflection (AR) coating for the laser beams that go through the windows, 852 nm coating for the preparation, cleanup, and detection beam windows and dual 1079-540 nm coating on the interaction beam window, seen in Fig. 2.1. If necessary, we can exchange the windows to other coatings if our needs change.

To form the atomic beam, we must first lower the pressure in the vacuum chamber. This is partly due to cesium's volatile reaction to water/air, along with reducing contaminants/air particles that would scatter the cesium atoms from the atom beam's trajectory. To get down to the appropriate pressure level we first use a roughing pump to get the pressure down to

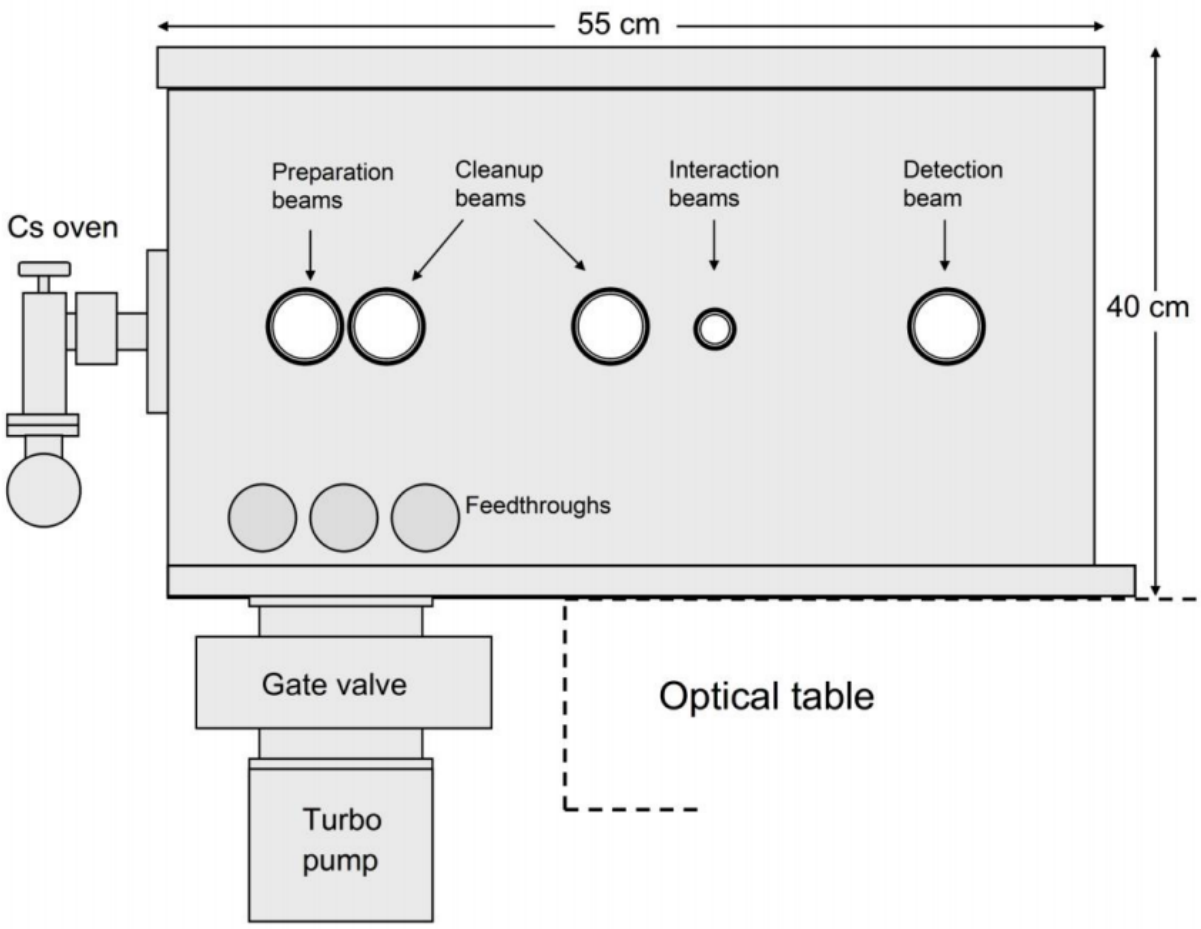

Figure 2.1. Drawing of vacuum chamber that holds the atom beam. From [71]. The feedthroughs are for any electrical connections needed inside the chamber and the gate valve is to there to close the turbo pump from the vacuum chamber for when we need to open up the vacuum chamber

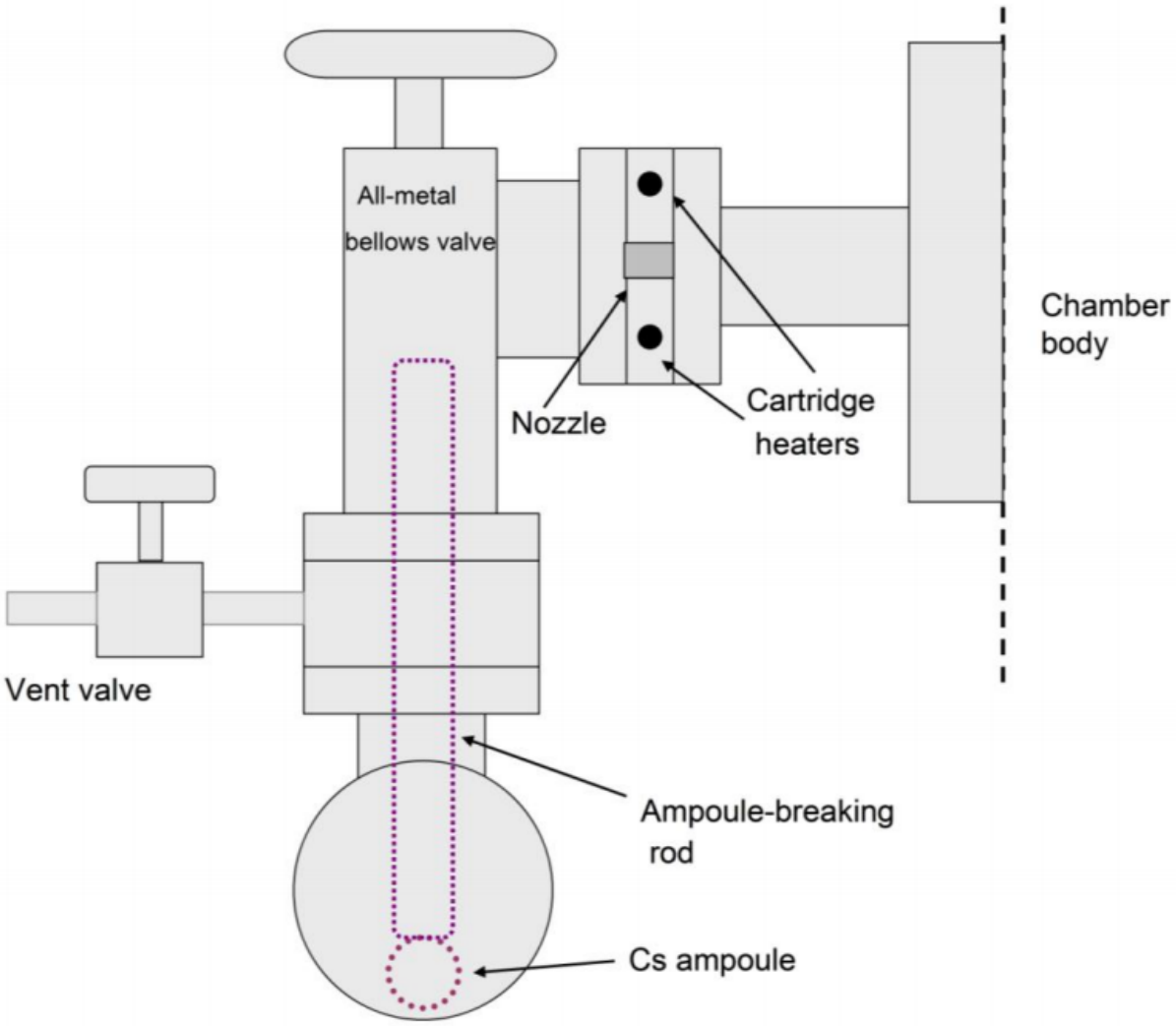

Figure 2.2. The cesium oven setup, to produce the cesium atom beam. From [71].

about 50 mTorr. Then the Edwards STP-451 turbo pump can be turned on to pump down to 1e-6 Torr level. After the whole vacuum chamber is brought down to pressure in the range of 1e-6 Torr, the rod can then be pushed down to break the cesium ampoule to release cesium into the system. When we heat the oven, a cesium cloud is formed in the chamber before the nozzle. These cesium atoms are able to escape through the nozzle and into the main chamber, forming a relatively collimated and dense beam of cesium atoms.

For the appropriate heating of the oven, the nozzle is heated higher than the rest of the body of the oven through use of the cartridge heaters to prevent clogging. The rest of the chamber is wrapped in heat tape, with the bottom chamber holding the cesium wrapped with slightly less heat tape. In general, the whole chamber is heated to about $140°C$ with the nozzle around $170°C$. After heating up for about 2 hours, the atom beam density is stable on time scales of interest, with slight drifts in the hour time frame due to small temperature changes. The changes are slight enough that no active temperature stabilization is needed. More details of the vacuum chamber construction are available in Anytpas's thesis [71].

2.1.2 Diode Lasers

The vacuum chamber layout is split up roughly into three general regions for the PNC experiments. Each region holds magnetic field coils and other equipment to support the function of each region inside the vacuum chamber. After the cesium atoms exit the oven they travel through the first region, the preparation region, where we pass laser beams that optically pump atoms into the state we desire. The second region is the interaction region, where we pass laser beams and house other necessary equipment to run the interaction of interest. The last region is the detection region, where we pass a 852 nm detection laser beam to observe the final state of the atoms after the interaction region using a photodiode.

The lasers used for detection and optical pumping are homemade 852 nm external cavity diode lasers (ECDL) that output around 15-30 mW in Littrow configuration, as seen in Fig. 2.3. We house the laser diode in a collimation tube that allows us to collimate the outgoing light into a beam that does not diverge significantly in the distance it takes the laser beam to reach the atomic beam. Once out of the collimation tube, the laser light hits

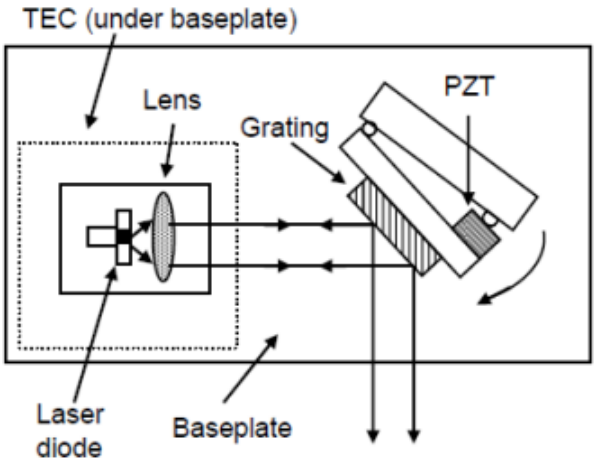

Figure 2.3. Our homemade ECDL setup. From [71].

a diffraction grating (1800 lines/mm), whose angle can be controlled with a piezo-ceramic transducer (PZT). We angle the grating such that the first-order diffraction from the grating goes back on the incoming laser, generating optical feedback that enhances the tunability and stability of the laser. The Littrow configuration also narrows the linewidth of the laser to around a couple of MHz, instead of around 30 MHz.

We stabilize and tune the frequency of the ECDL's through temperature, current, and angle of the diffraction grating. The temperature is stabilized for the laser with a thermoelectric cooler (TEC) and a temperature sensor (AD590). We have designed and built homemade temperature controllers, and have also used commercial units to set and hold the desired temperature for the laser diode, using the AD590 signal to control the TEC with a PI (proportional/integral) control system. To have fine control of the angle of the grating we apply a voltage to the PZT (where a change in voltage changes the length of the PZT), which will therefore change the angle. Finally we have also built a homemade current controller that is able to drive the diode laser with around 50-100 mA of current. By tuning all three of our controllers, we are able to precisely tune the laser to the necessary transition wavelength and also able to ramp the diode laser's frequency by ramping the PZT's voltage.

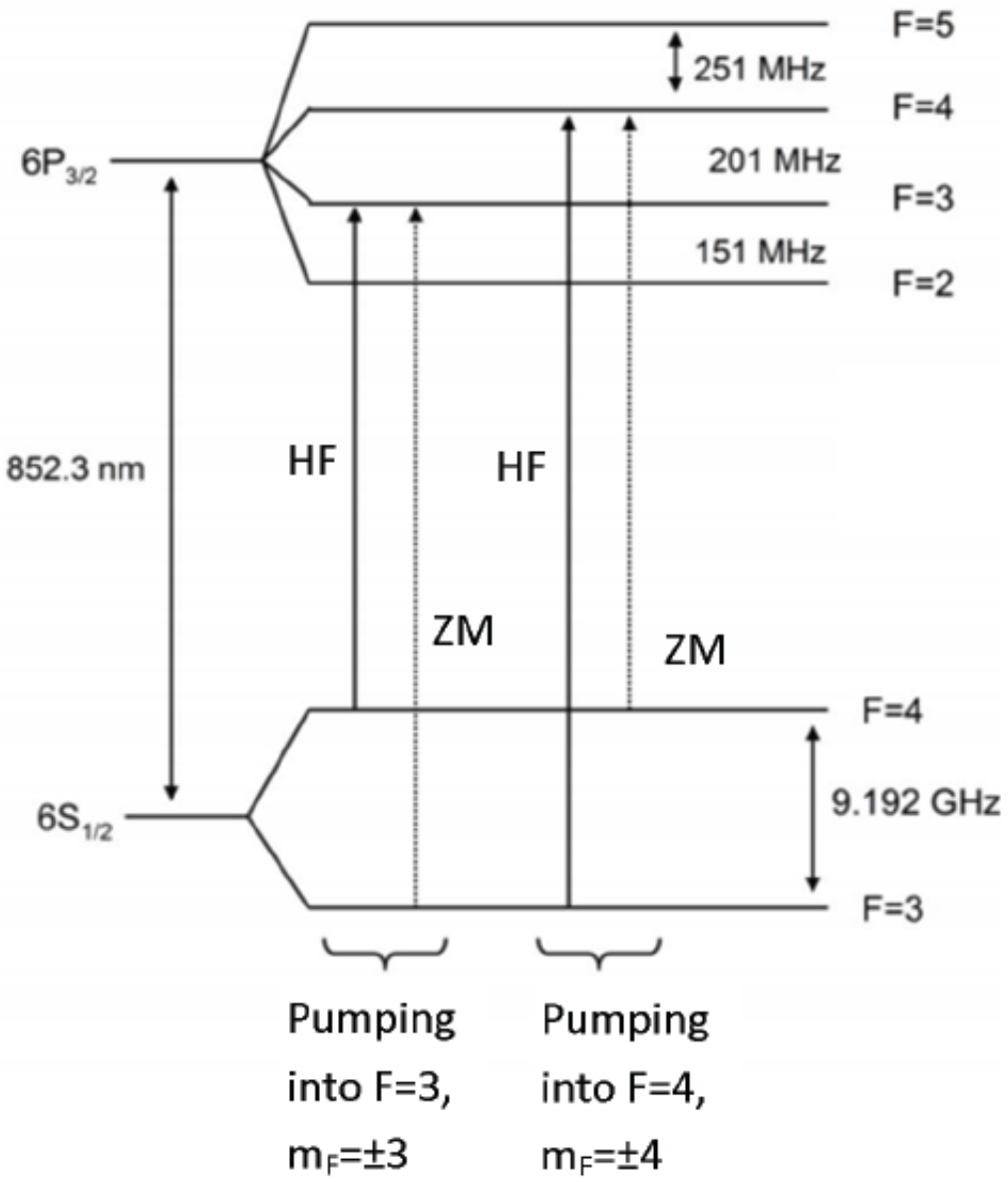

Figure 2.4. Energy level transitions for optically pumping atoms into one hyperfine m state. ZM=the Zeeman laser wavelength, HF= the hyperfine laser wavelength. From [71].

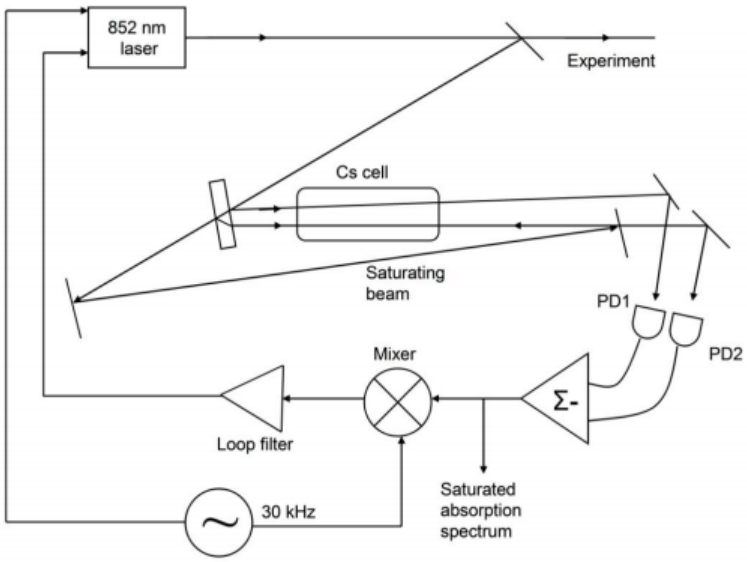

Figure 2.5. Typical setup of saturated absorption measurements. From [71].

For both PNC experiments, the cesium atoms need to be prepared into one state (F,m), where F = 3 or 4 is the total angular moment of the hyperfine level and m is the angular momentum projection quantum number. The m levels are all degenerate until a magnetic field is present to split the levels. To prepare the initial state we use two different lasers to optically pump the atoms into one atomic state. In addition, there are magnetic field coils in place to split the m levels to help optimize the state preparation. The first laser used is called the hyperfine laser, as it lases at the appropriate wavelength to push the atoms into only one of the hyperfine levels, as seen in Fig. 2.4. The second laser is called the Zeeman laser, as it pushes all of the atoms towards one side of the Zeeman sub-level, $m = +F$ or $m = -F$. The hyperfine laser is linearly polarized at the vacuum chamber to pump atoms out of one state, while the Zeeman laser is circularly polarized to drive the atoms to one extreme m state. In general, our set-up is able to push around 90% of the atoms into one state, (F, m), with the exact value depending on the dimensions of the atom beam and restrictions on magnetic fields for the experiment.

We lock the lasers to one frequency using a saturated absorption setup, seen in Fig. 2.5. A small part of the main beam is deflected before it goes to the experimental setup to be used

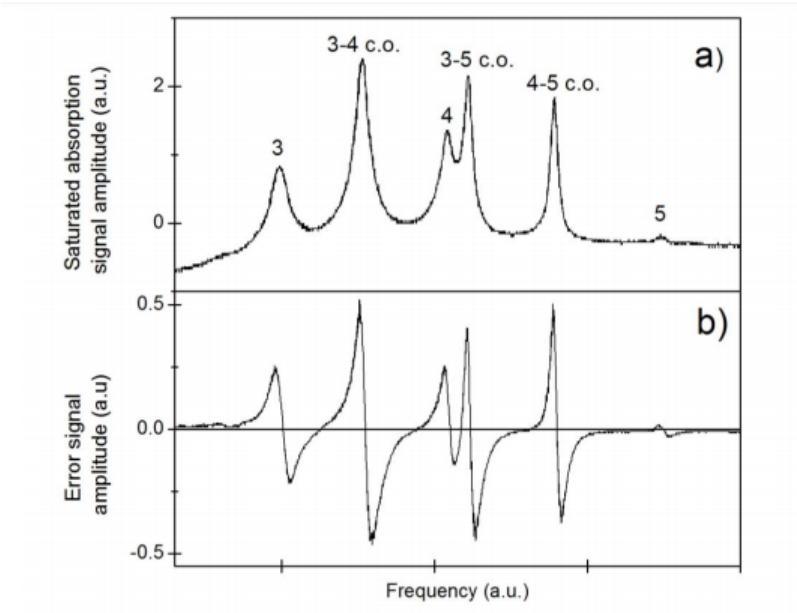

Figure 2.6. Typical saturation peaks of our homemade diode laser. The c.o. stands for cross over peaks between the two states. (a) The absorption spectrum directly from the photodiode. (b) The error signal from the absorption spectrum after being passed through our lock-in circuit. As seen when the absorption spectrum goes through the peak the error signal passes through zero. From [71].

to lock the laser. The beam used to lock the laser passes through a window that transmits most of the beam through to a mirror, but picks off two beams. These two picked-off beams pass through a cesium cell and onto their own photodiode. The beam that was transmitted through the window crosses the cell in the opposite direction to the two picked-off beams. It is aligned such that it overlaps one of the two picked off beams going through the cesium cell. This produces Doppler-free absorption dips inside the Doppler broadened background for one of the picked off beams, while the other beam is just a Doppler-broadened absorption. When the two photodiode signals are subtracted from each other, they give saturated absorption peaks that have no Doppler-broadened background, as seen in Fig. 2.6 (a).

The error signal in Fig. 2.6 (b) is obtained by dithering the laser current. We use the error signal to lock the laser frequency to the peak of one of the saturated absorption peaks. With just the photodiode signal, the laser frequency we want is at the top of the peak, and on both sides of the peak the amplitude of the signal decreases. The control loop is unable to lock to the top of the peak as it is not able to distinguish between negative and positive frequency drifts, as both ways result in a decrease in signal. To lock to the peak of absorption, we need an error signal that increases on one side of the peak and decreases on the other. To achieve this we dither the laser current at about 25 kHz in our laser current controller. This will therefore dither the laser beam output which then means the photodiode signal will also have the 25 kHz modulation on it. We can then mix a 25 kHz reference signal with the photodiode signal in an analog multiplier, which results in an error signal where the peak is at zero amplitude, with a slope that allows us to lock to the peak at zero amplitude. We mix the signal in a homemade lock-in circuit, originally designed by Dionysios Antypas [71]. This circuit also allows us to tune the PZT and send the dither signal to the laser current controller.

The detection laser is setup similarly to the hyperfine and Zeeman lasers. This laser is linearly polarized at the vacuum chamber. We tune the detection laser to the transition frequency from the initially-empty hyperfine state up to a state in the $6p_{3/2}$. We chose the hyperfine component of the $6p_{3/2}$ level such that the atoms will only decay back to the emptied ground hyperfine state. This way when we have nothing going on in the interaction region, the detection laser will not excite any atoms. Only when there is an interaction

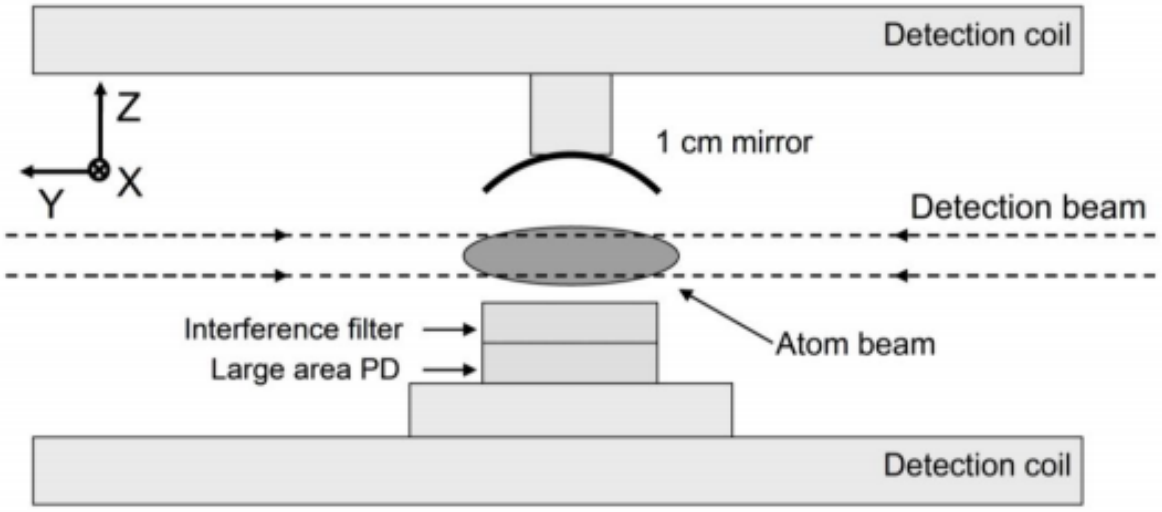

Figure 2.7. The detection region setup. The atom beam is in the +x direction, or into the page. From [71].

that excites atoms to a state that subsequently decays to the initially-empty state will the detection laser be able to excite the atoms. Of course our preparation of the cesium atoms is not perfect, so there is some background signal due to the imperfect preparation. Additionally, there can be background cesium around the chamber that is leftover after the atom beam hits the back wall and is not removed by the vacuum pump. We have a liquid nitrogen-cooled baffle (two copper plates) that we can cool down to trap and collect the background cesium to reduce the effects of the background cesium on the system.

In the detection region, we use a large-area photodiode (Hamamatsu # S3204-08), setup like shown in Fig. 2.7, with an interference filter above it that only allows 852 nm light through. The interference filter helps eliminate noise from entering the signals as other frequencies of light are blocked. Therefore, when the detection laser excites an atom and the atom decays, the photodiode has a chance of picking up the emitted light. Not all of the photons will be captured by the photodiode due to the atom decaying in all directions, not just towards the photodiode. To improve the chance of detecting more of the emitted photons, we place a mirror above the photodiode to help in reflecting some more of the

emitted light from the atoms back onto the photodiode. Additionally, due to the fact that we use multiple 852 nm lasers in the vacuum chamber, there will be scattered light from them adding a background to the detection signal since the interference filter will not block their light.

2.2 Measurement of E_{PNC} on the $6s - 7s$ Transition

One of the main efforts in the lab using this setup is to improve on the measurement of Wood et al. [24], [38] of E_{PNC} on the $6s - 7s$ transition, led by Jonah Quirk. The experimental measurement done by Wood et al. found that the NSI component is $E_{PNC}/\beta = 1.5935(56)$ mV/cm, which has a 0.35% uncertainty, from the average of their two measurements [24]. Our lab hopes to reduce the uncertainty to $\simeq$0.1%, which we believe is possible due to potentially lower systematic errors with the two-color measurement technique in comparison to Wood's. This measurement will also be able to yield the NSD component, but our measurement of the NSD component on the ground state hyperfine transition will end up being more precise, rendering the extraction of the NSI component the main purpose of this experiment.

These efforts are being led by Jonah Quirk. Additionally, along with George Toh, I helped make measurements of electric dipole matrix elements in cesium that have helped produce a more precise value of α and β, seen in Appendix A.

2.3 Anapole Moment

Our next major experiment is to measure the anapole moment/NSD component in cesium on the ground state hyperfine transition, which I have led. Wood et al. [24], [38] were able to extract the NSD component from their measurement of E_{PNC} of the $6s - 7s$ transition and found that the NSD component of E_{PNC} was $E_{PNC}/\beta = 0.077(11)$ mV/cm, which has a 14% uncertainty [24]. The sizable error was due to the fact that the NSD component was the difference between the two measurements. Our lab plans to drastically reduce the uncertainty (and verify the value due to discrepancy with theory and Wood et al.'s value) with a different method than Wood et al. Our method uses the interference between interactions

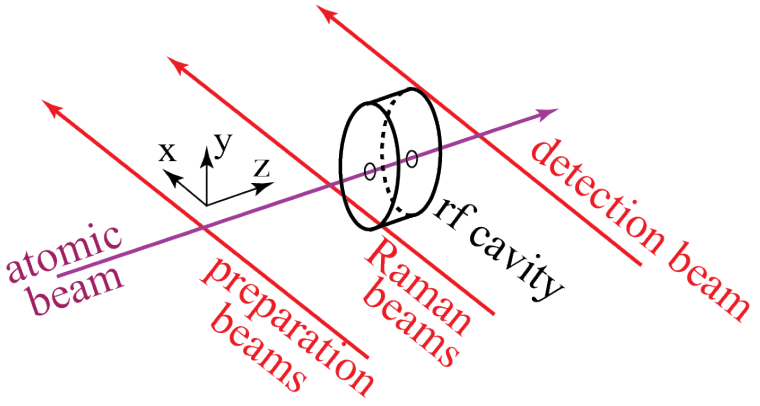

Figure 2.8. Experimental setup for the anapole moment experiment.

driven by laser fields and radio frequency (rf) fields, to directly measure the NSD component in cesium. We use a similar setup as the $6s - 7s$ transition measurement but with changes in the interaction region to support the rf and laser fields, found in the experimental setup in Fig. 2.8.

The basic setup of the atom beam and lasers discussed in this chapter will be used for both the anapole moment measurement and E_{PNC} on the $6s - 7s$ transition measurement. I will discuss the exclusive setup and theory in greater detail in Chapter 3 for the anapole moment measurement.

3. ANAPOLE MOMENT EXPERIMENTAL SETUP

3.1 Introduction

The anapole moment measurement has been led by me and is the main goal of the work described in this thesis. This is a long term project that I have made significant progress on, but a future student in the lab will need to complete it. There has been only one measurement of the anapole moment in an atom, the experiment done by Wood et al. [24], [38] in cesium. The meson coupling constants extracted from the NSD component of E_{PNC} do not agree with those from related high energy measurements [42]. Therefore it is of great interest to verify the anapole moment in cesium, along with reducing the error bars to see if there is disagreement between different measurement methods. Our goal is to measure the anapole moment in cesium using a two-color interference technique to extract the weak interaction with an uncertainty of around 3%. In this chapter I will describe the setup I used to attempt to measure the anapole moment. In Chapter 4, I will discuss the current experimental progress and results I have made towards measuring the anapole moment, along with the roadblocks that have prevented the successful measurement of the anapole moment.

3.2 Fields

In the interaction region we have two different fields separated by ∼1 cm, a rf field and a laser field. We apply a static B_z field at ∼7 G to define the quantization axis and to Zeeman split the ground state to tune the interactions' transition frequency to be at the resonance of the rf cavity. The general setup can be seen in Fig. 2.8 for the experiment. We use the interference of the rf and Raman laser field-induced interactions to obtain the modulation amplitude that is large enough to be precisely detected. The use of our two-color coherent control technique necessitates careful control over the mutual coherence of the two fields to create the modulation signal. This means that the atoms will have to be coherent across both of the fields in the interaction region for us to see the modulation signal. The Raman laser field interaction is the strong interaction in comparison to the two rf interactions. It will populate a coherent mixed state of the F=3 and F=4 ground state in cesium. The

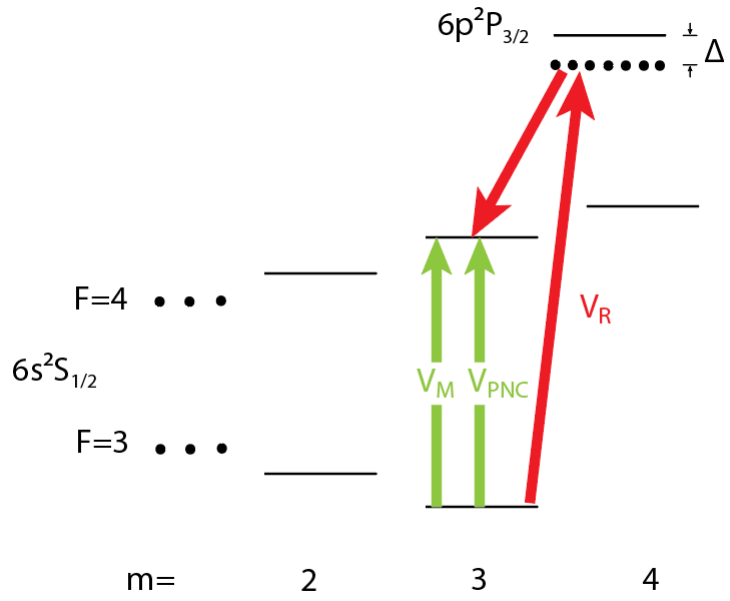

Figure 3.1. Energy level diagram for the NSD experiment. The red lines are the Raman interaction of two lasers. The green arrows are the rf interactions. V_R is the Raman interaction, V_M is the magnetic dipole interaction, V_{PNC} is the PNC amplitude, and Δ is the detuning from directly exciting the $6p_{3/2}$ state.

rf field interaction is the weak interaction for the interference technique, a combination of the M1 and PNC interactions. The diagram of the energy levels for the experiment can be seen in Fig. 3.1, along with labeling the interactions' transitions. We must minimize the M1 interaction to be smaller than the PNC interaction amplitude and calibrate the experiment by experimentally determining the size of the rf field amplitude inside the rf cavity at a given input rf power. More details on how we will be able to achieve this will follow in the chapter.

3.2.1 Raman Field

The Raman laser field is generated by two lasers whose frequencies differ by the approximate difference between the hyperfine components of the ground state ($6s_{1/2}$) in cesium, about 9.2 GHz. The lasers are both linearly polarized parallel to one another and along the

z-axis (parallel to the atomic beam direction) to drive a $\Delta m = 0$ Raman transition. The Raman interaction can be written as

$$V_R = \tilde{\alpha}\ \varepsilon_z^{R1}\ \varepsilon_z^{R2}\ \mathrm{e}^{\mathrm{i}(\omega^{rf}t - \Delta k y - \phi^R)}\ C_{Fm}^{F'm}, \tag{3.1}$$

where $\tilde{\alpha}$ is the Raman polarizability that depends on the detuning from the exact transition frequency between the hyperfine components of the ground state. ε_z^{R1} and ε_z^{R2} are the electric field amplitudes of each of the individual lasers with parallel polarization. $\omega^{rf} = \omega^{R1} - \omega^{R2} = 2\pi\nu^{rf}$, where ν^{rf} is ≈ 9.2 GHz, the approximate difference between the hyperfine components of the ground state in cesium (9.192631770 GHz) and ω^{R1} and ω^{R2} are the laser frequencies. The difference between the phases of the two components, $\phi^{R1} - \phi^{R2}$, is equal to ϕ^R and the difference between the propagation numbers of the two lasers is Δk. t is the time, y is the distance of the interaction region, and $C_{Fm}^{F'm}$ are factors that are proportional to the respective Clebsch-Gordan coefficients. $C_{Fm}^{F'm}$ are defined in Ref. [72] and seen in Table 3.1. V_R increases as the detuning of the lasers from $6s_{1/2} - 6p_{3/2}$ transition frequency decreases, but if the detuning is too small there could be direct excitation of the atoms to the $6p_{3/2}$ state. Additionally, the more power there is in the Raman lasers, the stronger the Stark effect is, which changes the resonant frequency of the transition. We need the transition resonance of the rf and Raman interactions to occur near the same frequency such that the interactions are both strong and near the peak. Thankfully the two different Raman lasers shift the resonant frequency in the opposite directions, such that we can effectively cancel out the Stark effect shift. After some tests in the setup, discussed in the next chapter, we decide upon a detuning of 230 MHz away from exciting directly to the $6p_{3/2}$ F=3 state.

3.2.2 RF Field

The rf field's frequency is ≈ 9.2 GHz, approximately the difference between the hyperfine components of the ground state ($6s_{1/2}$) of cesium. The rf and Raman amplitudes both excite atoms from one ground hyperfine state to the other in cesium, as seen in Fig. 3.1. The rf

Table 3.1. $C_{Fm}^{F'm'}$ from Ref. [72].

F	m	F'	m'	$C_{F,m}^{F',m'}$
4	m'	4	m'	$\frac{1}{4}(m')$
4	m'-1	4	m'	$-\frac{1}{8}[(5-m')(4+m')]^{1/2}$
4	m'+1	4	m'	$\frac{1}{8}[(5+m')(4-m')]^{1/2}$
4	m'	3	m'	$\frac{1}{4}[16-m'^{\,2}]^{1/2}$
4	m'-1	3	m'	$-\frac{1}{8}[(5-m')(4-m')]^{1/2}$
4	m'+1	3	m'	$-\frac{1}{8}[(5+m')(4+m')]^{1/2}$
3	m'	4	m'	$\frac{1}{4}[16-m'^{\,2}]^{1/2}$
3	m'-1	4	m'	$\frac{1}{8}[(3+m')(4+m')]^{1/2}$
3	m'+1	4	m'	$\frac{1}{8}[(3-m')(4-m')]^{1/2}$
3	m'	3	m'	$-\frac{1}{4}(m')$
3	m'-1	3	m'	$\frac{1}{8}[(3+m')(4-m')]^{1/2}$
3	m'+1	3	m'	$-\frac{1}{8}[(3-m')(4+m')]^{1/2}$

field is contained and amplified in a rf cavity that supports 9.2 GHz. The PNC interaction is in the form of

$$V_{PNC} = -\ E_{PNC}\ \varepsilon_z^{rf}\ C_{Fm}^{F'm}, \tag{3.2}$$

where E_{PNC} is the quantity we wish to measure and ε_z^{rf} is the electric field amplitude of the rf wave. We will assure the coherence between the rf and laser fields by using stable rf sources and using state-0f-the-art phase locking techniques. Additionally, the other interac-

tion driven by the rf fields, the magnetic dipole interaction V_m, will need to be addressed due to it being stronger by several orders of magnitude compared to the PNC interaction.

The basic magnetic dipole moment Hamiltonian is

$$H_{M1} = -\frac{\mu_B \mu_0}{\hbar}(g_S \vec{S} + g_L \vec{L} + g_I \vec{I}) \cdot \vec{h}^{rf}$$

where μ_B is the Bohr magneton, μ_0 is the vacuum magnetic permeability, g_S is the electron spin g-factor, g_L is the electron orbital g-factor, and g_I is the nuclear g-factor. $\vec{h}^{rf}$ is the rf magnetic field while $\vec{L}$ is the orbital angular momentum, $\vec{S}$ is the spin angular momentum, and $\vec{I}$ is the total nuclear angular momentum [73]. In our case since we are in the ground state, we can use $\vec{L} = 0$ and $g_S \gg g_I$ to simplify to

$$H_{M1} = -\frac{\mu_B \mu_0}{\hbar}(g_S \vec{S} \cdot \vec{h}^{rf})$$

To then obtain the magnetic dipole transition amplitude, we can use

$$V_m = \langle 6S_{1/2} F m \mid \mu_B \mu_0 (g_S \vec{S} \cdot \vec{h}^{rf}) \mid 6S_{1/2} F' m' \rangle$$

Specifically, the magnetic dipole transition amplitude contribution for the $\Delta m = 0$ transition in the ground state of cesium is

$$V_m = \frac{\sqrt{16 - m^2}}{8} g_s \mu_B \mu_0 \left\{ h_z^{\mathrm{rf}} + \left(\frac{h_x^{\mathrm{rf}} B_x + h_y^{\mathrm{rf}} B_y}{B_z} \right) \right\}. \tag{3.3}$$

B_{i} are the external static magnetic field components and h_{i}^{rf} are the magnetic field components in the rf cavity. As a note the $C_{Fm}^{F'm}$ values are already included in the amplitude value. As long as the external B_x and B_y magnetic fields are well controlled then for the $\Delta m = 0$ transition, the only rf magnetic field that contributes is the h_z^{rf} field. For the TM_{010} mode of an ideal cylindrical rf cavity, the h_z^{rf} field is identically zero. Along the central axis of the cylinder, h_x^{rf} and h_y^{rf} are at their smallest value and e_z^{rf} is at its largest, seen in equations:

$$\mathrm{e}_z^{rf}(\rho) = \mathrm{e}_0^{rf} J_0 \left(\frac{2.405 * \rho}{R_0} \right) \tag{3.4}$$

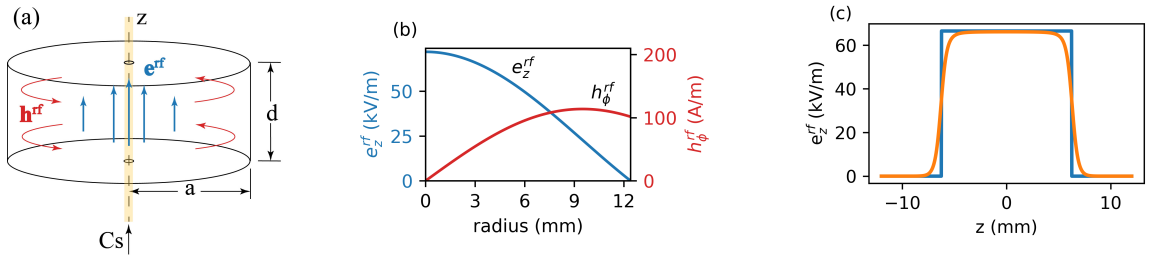

Figure 3.2. (a) perfect cylindrical rf cavity field modes, $\mathbf{e}^{\mathrm{rf}}$ is the axial electric field and $\mathbf{h}^{\mathrm{rf}}$ is the azimuthal magnetic field of the TM_{010} mode. (b) $\mathrm{e}_z^{\mathrm{rf}}$ and h_φ^{rf} vs. the radial distance to show the variation in magnitude across the radius of a perfect cylindrical cavity. (c) COMSOL data with necessary holes simulated (orange) of $\mathrm{e}_z^{\mathrm{rf}}(z)$ vs. z (along the atom beam) compared to perfect cavity with no holes (blue).

and

$$h_\phi^{rf}(\rho) = -\mathrm{i}\sqrt{\frac{\epsilon}{\mu}}\,\mathrm{e}_0^{rf} J_1\left(\frac{2.405 * \rho}{R_0}\right) \tag{3.5}$$

[74]. e_0^{rf} is the magnitude of the electric field on the axis, ρ is the radius out from the center of the rf cavity, and R_0 is the radius of the rf cavity. ϵ is the permittivity and μ is the permeability of the medium inside the rf cavity (in our case the medium is vacuum). $J_1(2.405 * \rho/R_0)$ and $J_0(2.405 * \rho/R_0)$ are the first-order and zero-order Bessel functions of the first kind respectively. The atom beam traverses the rf cavity along the central axis to capitalize on this feature to minimize V_m in comparison to V_{PNC}. Figures of the magnetic and electric fields of the chosen design of a perfect cylindrical rf cavity can be seen in Fig. 3.2, which illustrate the strong electric field and small magnetic field at the central axis of the cavity. I will discuss the necessary adjustments to the rf cavity to design the cavity in real life later in this chapter.

3.2.3 Potential Miscellaneous Fields

The electric quadrupole (E2) transition can also be potentially driven by the rf cavity's field, in the region when e_z^{rf} turns on or off as the atoms enter and exit the rf chamber. Derevianko has calculated permanent E2 moments for each ground state hyperfine compo-

nent [75]. They are reported as $Q^{\mathrm{HFI}}_{F=3} = 8.4 \times 10^{-6}\ \mathrm{e}a_0^2$ and $Q^{\mathrm{HFI}}_{F=4} = -1.6 \times 10^{-5}\ \mathrm{e}a_0^2$. In order to verify this effect should be minimal, we estimate $Q \sim 1 \times 10^{-5}\ \mathrm{e}a_0^2$. This leads us to estimate that

$$\frac{A_{E2}}{A_{PNC}} \sim \frac{Q\,(\partial \mathrm{e}_z^{\mathrm{rf}}/\partial z)}{E_{PNC}\mathrm{e}_z^{\mathrm{rf}}} \sim \frac{Q}{E_{PNC}\Delta z} \sim 0.3. \tag{3.6}$$

$\Delta z (\sim 1$ mm) is the distance over which $\mathrm{e}_z^{rf}(z)$ turns on/off as the atoms enter or leave the cavity, as illustrated in Fig. 3.2(c). As a further note for the experiment, the E2 interaction is applied over a much shorter region that the PNC interaction, so it should be lower than this. Even if this signal is as large as our pessimistic value, E2 changes sign when reversing m while the PNC signal does not. We will be able to identify if E2 is active in our system by observing this signal on both the m = 3 and m = -3 starting states [76]. Differences can be attributable to the E2 moment and we will be able to average the two signals to identify just the PNC signal.

Another possible field which can cause an unwanted interaction, is a static electric field in the region. This would cause a Stark-induced interaction in the interaction region. For a $\Delta F = \pm 1$ transition, the Stark transition's amplitude is related to the vector polarizability β. β can be calculated using a sum over states expression, which can be found in Refs. [77], [78]. The simplified expression with just the most impactful intermediate states is

$$\beta \sim \frac{1}{6}\left[\frac{|\,\langle 6p_{1/2}\,||\,r\,||\,6s_{1/2}\rangle\,|^2}{(E_{6s_{1/2}} - E_{6p_{1/2}})^2} + \frac{1}{2}\frac{|\,\langle 6p_{3/2}\,||\,r\,||\,6s_{1/2}\rangle\,|^2}{(E_{6s_{1/2}} - E_{6p_{3/2}})^2}\right] \times \Delta E_{6s_{1/2},\mathrm{hfs}}. \tag{3.7}$$

$\langle np_{\mathrm{j}}\,||\,r\,||\,ms_{1/2}\rangle$ are the reduced dipole matrix elements, $E_{6s_{1/2}}$ and $E_{6p_{\mathrm{j}}}$ are the state energies, and $\Delta E_{6s_{1/2},\mathrm{hfs}}$ is the hyperfine splitting. For the hyperfine transition of interest we approximate $\beta = 0.0035\ a_0^3$. We don't believe this interaction will be of concern for the experiment, as using a static electric field of 0.1 V/cm in the interaction region, which is overly pessimistic for how big a static electric field should be in the region, the ratio of the Stark amplitude to the PNC amplitude is at most

$$\frac{\beta E_0}{E_{PNC}} \sim 0.033. \tag{3.8}$$

We also consider that our atom beam has width. h_y^{rf} and h_x^{rf} are only zero at the very center of the rf cavity and increase moving off center. Therefore part of the atom beam will travel through regions of the rf cavity with h_y^{rf} and h_x^{rf}. The interference between the Raman interaction and the rf field due to h_y^{rf} and h_x^{rf} is spatially averaged over the atom beam to zero when the atom beam is centered on the rf cavity. The is due to the sign flipping for the value of h_y^{rf} and h_x^{rf} over the appropriate x- or y-axis of the rf cavity, as seen when converting cylindrical coordinates to rectangular coordinates in Eq. 3.5. It is impossible to 'perfectly' center the rf cavity to the atom beam or zero the B_x and B_y magnetic field. Therefore there will be a small V_m signal due to h_y^{rf} and h_x^{rf}. For the atom beam somewhat off center (in the range of 10's of nm), the average magnetic dipole signal, normalized to the PNC signal and with the factor of a small transverse magnetic field, is roughly

$$\frac{\mid V_m(\rho_0) \mid 4\rho_0\Delta x}{\mid V_{\rm PNC} \mid \pi\rho_0^2} \approx \frac{\sqrt{7}}{2\pi}\left(\frac{g_s\mu_B\mu_0}{E_{\rm PNC}}\right)\left(\frac{h_y^{\rm rf}(\rho_0)}{{\rm e}_z^{\rm rf}(0)}\right)\left(\frac{B_y}{B_z}\right)\left(\frac{\Delta x}{\rho_0}\right). \tag{3.9}$$

For our setup, $\rho_0 \sim 0.5$ mm is the radius of the atomic beam, $h_y^{\rm rf}(\rho_0) \sim 10$ A/m is the magnetic field amplitude maximum in the atomic beam at a distance ρ_0 from the axis of the science chamber, ${\rm e}_z^{\rm rf}(0) \sim 70$ kV/m is the electric field amplitude along the central axis, and Δx is the distance from the center of the atom beam to the science chamber axis. For perfect alignment, $\Delta x = 0$. For this calculation the atoms are just moving in the z-direction for simplicity. Using $B_y = 3$ mG, $B_z = 7$G, and $\Delta x = 30$ nm (smallest resolution of the positioner we use and best current estimate for how low we can get the B_x and B_y magnetic field using the rf only signal), we estimate the transverse magnetic signal is a factor 2 times larger than the PNC signal. We cannot use the rf only signal to reduce the B_x and B_y fields small enough to observe E_{PNC}. As an important note, since $h_x^{\rm rf}$ and $h_y^{\rm rf}$ are $\pi/2$ out of phase with ${\rm e}_z^{\rm rf}$ and $V_{\rm PNC}$ is imaginary, V_m and $V_{\rm PNC}$ are in phase with one another. Therefore these amplitudes add directly, which increases the importance of reducing the magnetic dipole contribution through spatial averaging and B_x and B_y magnetic field reduction. More importantly, this means that we must reduce the magnetic dipole signal to a level much smaller than V_{PNC}, otherwise V_m modifies the V_{PNC} signal.

Lastly, we considered the idea that the $\Delta m = 1$ transition amplitude could have a small effect on the $\Delta m = 0$ transition due to the width of the transitions. The Zeeman splitting from $B_z \sim$ 7G would end up placing the two transitions about 2-3 MHz away from each other and the transitions' line-widths are about 10-20 kHz. Since there is a small amount of h_y^{rf} and h_x^{rf} causing a V_m interaction as discussed above, the $\Delta m = 1$ transition can be excited in the rf cavity. For our rf signal generator and amplifiers of the rf cavity's frequency, the spectral intensity of the rf signal 2.5 MHz from line center is about -100 dBc/$\sqrt{Hz}$. Even if these transitions occur, they are expected to only add to the dc atomic signal, not to the sinusoidal interference signal, as the $\Delta m = 1$ transition signal would not depend on the relative phase difference, $\Delta\phi$, between the rf field and the Raman beams. This is relaxed if the Raman beams also excites the $\Delta m = 1$ transition. The Raman beams could minimally excite the $\Delta m = 1$ transition as the spectral density in the wings of the beat signal are small at -50 dBc/$\sqrt{Hz}$. Additionally, the Raman interaction has minimal signal for the $\Delta m = 1$ transition peak due to the laser's polarization being along the z-axis and parallel to each other. For these reasons, we expect the interference from $\Delta m = 1$ transitions to be negligible.

3.3 Interference of the Raman and Weak Interactions

For our experiment we want to have the Raman and weak interaction interfere with each other. We ensure their interference due to the fact that we use two rf sources that have the same reference clock to drive both of the generators. To vary the phase between the Raman and rf interactions and observe changes in the interference, we control the relative phase difference between the two rf sources. We have developed two techniques for achieving this. One method uses a saw-tooth scan to linearly change the relative phase of one rf source while the other stays constant. We use this method for comparison of different magnetic field value configurations at the same relative phase difference. In the other method we set the two sources to slightly different rf frequencies, which will cause the relative phase difference to change at a continuous rate, where the rate is the frequency difference of the

two interactions. This method is preferable when working with the lock-in amplifier, as it allows a continuous scan with no breaks.

A difference between the interference here and that done by Wood et al. [24], [38] is the coherence between the two states in the transition. This is due to the fact that the lifetime of the ground state in cesium is much longer in comparison to the $7s$ state in cesium, making the coherence of the $6s - 7s$ transition much more limited than between the two hyperfine components of the ground state ($6s$). Due to the long lifetime of the ground hyperfine states, we had to take special care with the coherence between our two interactions and the two states. Additionally the simple interference equation 1.2 Wood et al. used does not adequately describe the interference in our system, which will be discussed below.

To describe the evolution of the atomic state, the system will be treated as a two-level system, where the state of the atoms is

$$\psi = c_g(t)\psi_g \mathrm{e}^{-\mathrm{i}\omega_g t} + c_\mathrm{e}(t)\psi_\mathrm{e}\mathrm{e}^{-\mathrm{i}\omega_\mathrm{e} t}. \tag{3.10}$$

$c_g(t)$ is the time-varying probability amplitude of the ground state and $c_\mathrm{e}(t)$ is the time-varying probability amplitude of the excited state. The interaction Hamiltonian is

$$V = V_R + V_m + V_{PNC}. \tag{3.11}$$

When the atoms leave the interaction region the excited state becomes

$$\mid c_\mathrm{e}(\infty) \mid^2 = sin^2(\mid \sum \Theta_\mathrm{i} \mid), \tag{3.12}$$

where Θ_i is the integrated interaction strength from V. Θ_i can be represented by the Rabi frequencies (Ω) from the individual interactions as the integration over all time as

$$\Theta_\mathrm{i} = \int \Omega_\mathrm{i}(t)dt, \tag{3.13}$$

where $\Omega_{\mathrm{i}}(t) = V_{\mathrm{i}}(t)/\hbar$. The Rabi frequency is the frequency of oscillations in the populations of the initial and final states over time. As the atoms are moving over the region in time, we can also represent Θ as an integration over distance instead of time as

$$\Theta_{\mathrm{i}} = \frac{1}{v}\int \Omega_{\mathrm{i}}(z)dz. \tag{3.14}$$

We can numerically calculate the evolution of the atoms in the final or initial state as the atoms transverse through the Raman and rf fields sequentially in our setup, which are separated by about 1 cm. The equations used for the numerical calculation are below.

$$\frac{dc_{\mathrm{e}}(t)}{dt} = c_g(t)(-\frac{\mathrm{i}}{\hbar}V\mathrm{e}^{\mathrm{i}\Delta\omega t}) \tag{3.15}$$

$$\frac{dc_g(t)}{dt} = c_{\mathrm{e}}(t)(-\frac{\mathrm{i}}{\hbar}(V)^*\mathrm{e}^{-\mathrm{i}\Delta\omega t}) \tag{3.16}$$

$\Delta\omega$ is the difference in frequency away from the exact transition frequency, from the rotating wave approximation.

To investigate the evolution of the atoms as they transverse through the interaction region we looked at the evolution between the ground and exited states represented by the Bloch sphere. A Bloch sphere is a useful way to represent the state space of a two-level quantum system, with an example of a layout in Fig. 3.3. The arrow on the Bloch sphere represents the complex value of the quantum state. The arrow will point either up or down depending on which of the two levels the quantum system is in.

We theoretically investigated the optimal Raman interaction's strength. We varied the strength of the interaction such that the average-velocity atoms ended up in different mixtures of the ground and excited states. We then had the rf field interact with the atoms and change the mixture between the excited and ground states, with the same rf interaction strength for the different mixtures. In simulations we found that having the rf interaction start with a 50-50 mixture maximized the final measured amount population change due to the rf interaction strength.

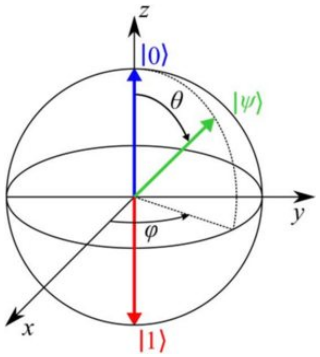

Figure 3.3. Layout for the Bloch sphere with spherical coordinates. If all of the atoms are in the excited state then the arrow will be on the $|\ 1\rangle$ arrow and if all of the atoms are in the ground state then the arrow will be along the $|\ 0\rangle$ arrow.

We used the TM_{010} mode from a perfect cavity for the rf field for our simulations in the initial planning stage. In the end, our rf cavity will have imperfections due to necessary holes to get the rf field and atoms into the cavity, but this should be sufficient for understanding the basic setup. The phase difference between the two interactions and its effect on the final state will be examined in the simulations. We numerically integrate Eq. 3.15 and Eq. 3.16 to calculate the value of c_{e} and c_g throughout the time the atom spends in the rf field.

There is an example of the Bloch sphere representation in Fig. 3.4, where I increased the size of the rf interaction by 1e5 times in order for the trail to be seen easily. Without the increase, the amount of change due to the transition is not apparent on the sphere. For better clarity of what the arrow is doing over time, I have included different components of the arrow in the included illustrations of real and imaginary parts of c_{e}, in the top of Fig. 3.5. Additionally, using traditional spherical coordinates for physics, the value of the ϕ and θ angles of the arrow on the sphere are shown in the bottom of Fig. 3.5. One can see the general evolution of the mixture of the final state due to the rf interaction.

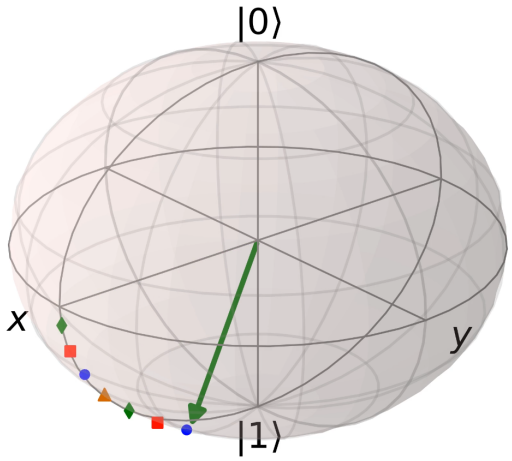

Figure 3.4. Example of Bloch sphere image simulation. The trail of dots represents where the arrow was at earlier times. The starting state is pointing along the x-axis on the equator of the sphere. The arrow is at the final position after the interaction. The PNC interaction's strength is increased by 1e5 in this figure to improve visibility. Illustrations of real and imaginary parts of c_e are shown in Fig. 3.5 on the bottom and the angles ϕ and θ for the Bloch sphere in Fig. 3.5 on the top. The trail shows the evolution of the atomic state as the atom traverses through the interaction region. The calculation is through the center of the rf cavity with no B_x and B_y magnetic fields, therefore the M1 interaction has no effect on the sphere. The Raman interaction prepares the atom in a fifty-fifty mix between the excited and ground states, straight along the positive x-axis.

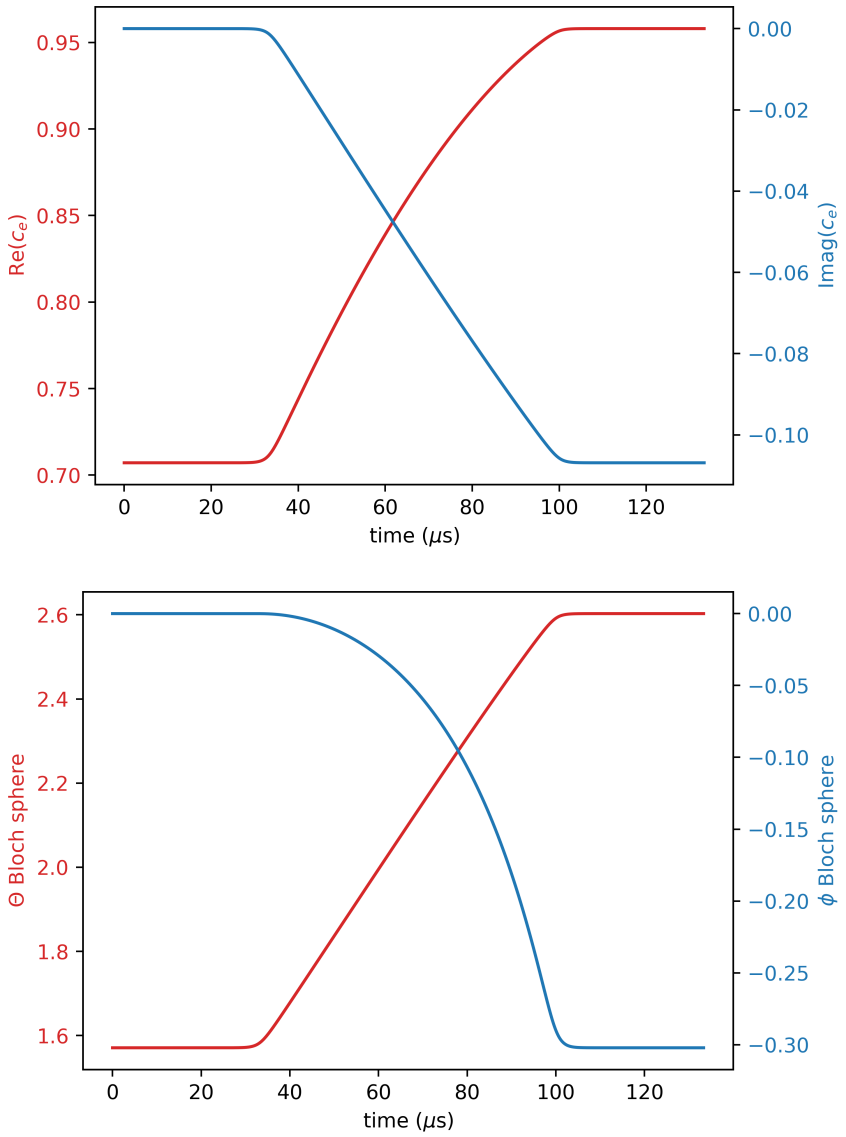

Figure 3.5. (Top) The real and imaginary parts of c_e over time for the Bloch sphere illustrated in Fig. 3.4. The rf interaction is increased by a factor of 1e5 times a realistic value to improve visibility on the Bloch sphere. (Bottom) Θ and ϕ over time for the Bloch sphere illustrated in Fig. 3.4. The rf interaction is increased by a factor of 1e5 times a realistic value to improve visibility on the Bloch sphere.

The more applicable variable of interest that I will be using from here on out is the fractional change in population on the excited state from the initial 50-50 mixture due to the rf field as the phase changes,

$$\Delta P = \frac{\mid c_{\rm e}(max) \mid^2 - \mid c_{\rm e}(min) \mid^2}{2}. \tag{3.17}$$

$c_{\rm e}(max)$ is the maximum final $c_{\rm e}$ value and $c_{\rm e}(min)$ is the minimum final $c_{\rm e}$ as the phase between the rf and Raman fields changes. ΔP is the amplitude of the sinusoidal variation of the atomic population in the excited state due to the phase. This will be the value that we can experimentally measure. The evolution of ΔP over time through the rf interaction, after the Raman interaction already initialized the 50-50 mixture, is seen in Fig. 3.6 for the interactions in phase and out of phase. We will change the phase between the Raman and rf interactions in this experiment to obtain the PNC interaction magnitude. A simulation of ΔP vs phase can be seen in Fig. 3.7. For this calculation we have assumed that V_m is zero for simplification. The Raman lasers interaction is only seen in this figure as the initial starting condition. The rf field starts to interact at time = 40 μs and stop at time= 100 μs. We used 270 m/s as the velocity of the atoms through the interaction region. The value of 270 m/s is the peak velocity in the equation from Ramsey's equation of the velocity distribution coming out of an atomic beam oven [79]. For later calculations we use COMSOL simulations of all of the fields of interest to obtain more realistic accounts for our rf cavity, along with averaging over the full velocity distribution from the atomic beam oven.

3.4 Measurement Plan

Our method to measure the NSD PNC effect is to interfere the PNC interaction from the rf cavity with the Raman interaction from the two Raman lasers. We need plans to reduce V_m to well below V_{PNC}. We also need a plan to calibrate the obtained experimental signal to the PNC amplitude, E_{PNC}. In this section I will detail the methods we have to isolate the NSD PNC effect in the experiment.

The first step to reduce V_m was to minimize the external magnetic field in the interaction region due to the Earth. One method to identify if an external magnetic fields exist in the

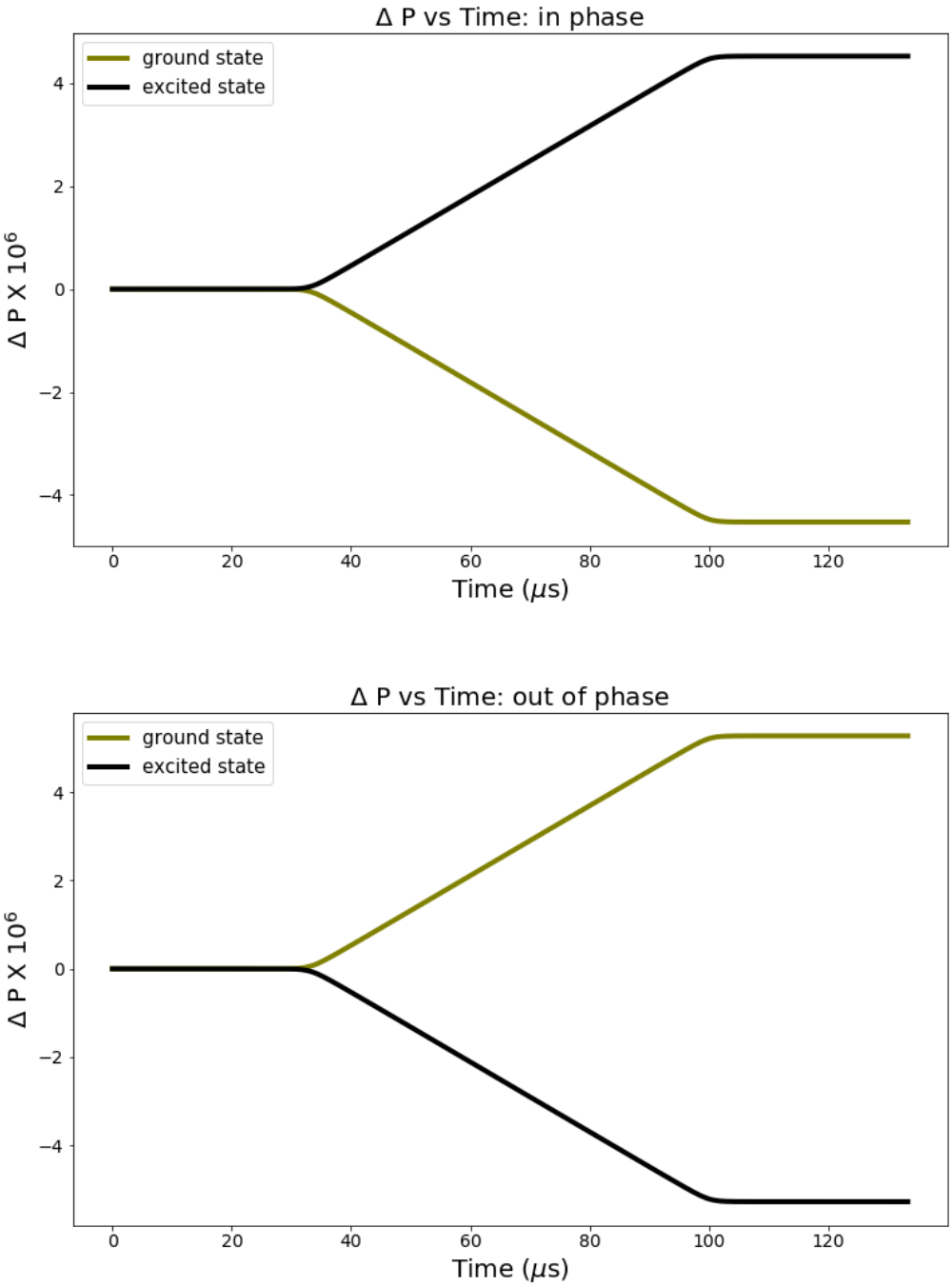

Figure 3.6. The evolution of the change in population (ΔP) as atoms pass through the interaction region. Top picture: the Raman and weak interactions are in phase (phase=0): Bottom picture: the Raman and weak interactions are out of phase (phase=π). The Raman fields give the initial state, half the population in the excited (black) and ground (olive) state. The rf field interaction starts at t≈40 μs and ending at t≈100 μs.

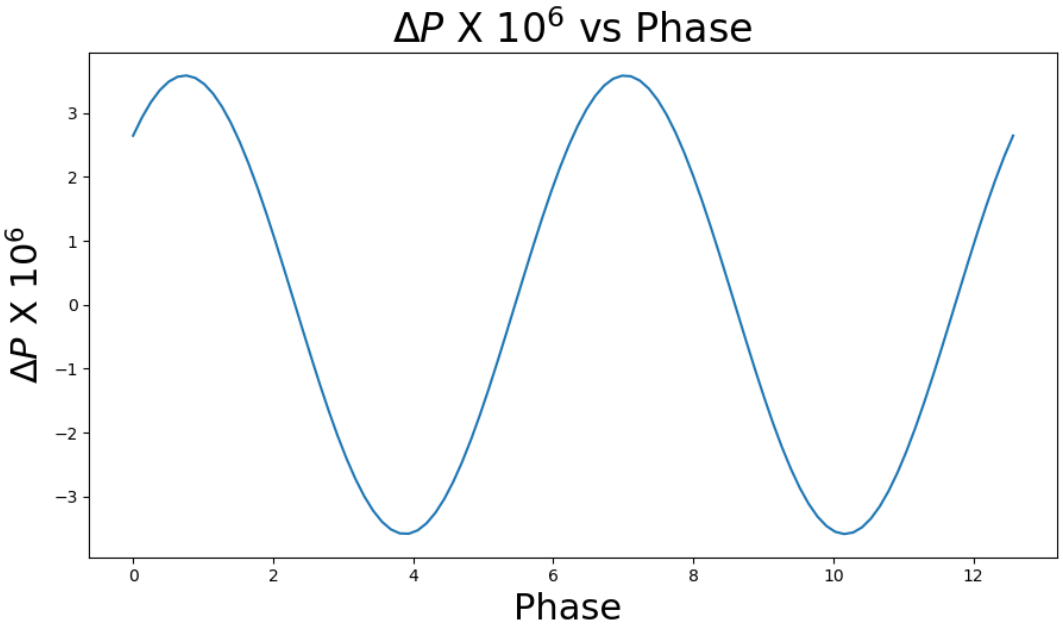

Figure 3.7. The variation of the change in population (ΔP) vs phase difference ($\Delta\phi$) between the Raman interaction and rf interaction.

interaction region is by sweeping the rf frequency over either of the interaction's peak at 9.1926 GHz. A single peak is expected when the magnetic field is near zero since all of the $\Delta m = 0$ and $\Delta m = 1$ transitions from different m states are degenerate. Any extra peaks or broadening of the peak are indicative of a non-zero magnetic field for the interaction. For this test, the optical pumping Zeeman beam should be off while the hyperfine laser is on, to not have all of the atoms pushed to just one extreme m value in the ground state. We can then optimize the magnetic field coil's current to zero the field in the interaction region by correcting the peak to just a single narrow peak. One can do this with either the Raman beams or rf cavity to minimize the external magnetic field across the whole interaction region.

We then introduce the 7 G B_z field to find and isolate the $\Delta m = 0$ transition peak for the experiment. This introduced a small B_x and B_y into the interaction region. As discussed before, we will be able to reduce V_m for a $\Delta m = 0$ transition peak, due to h_y^{rf} and h_x^{rf} with a small B_x and B_y value, by centering the rf cavity to the atom beam and zeroing the transverse magnetic fields. This is achievable by iterating magnetic coil's current values and rf cavity position while minimizing the rf only signal (no interference) for the $\Delta m = 0$ transition. If there is h_z^{rf} along the path of the atom beam, we will not be able to reduce its associated V_m. During COMSOL investigations into different rf cavity shapes, we found that h_z^{rf} can be introduced to the rf cavity through the holes in a perfect cylindrical rf cavity (or in general any imperfection from a perfect cylinder). We need holes to input the rf power and, more importantly, the atom beam. Therefore, atoms will potentially experience h_z^{rf} in the atom entry and exit hole. Thankfully, due to the fact that e_z^{rf} is strong over the whole rf cavity's length and h_z^{rf} is most likely introduced around the entry/exit holes for the atom beams, the two interactions will have different spatial shapes across the rf cavity, seen in Fig. 3.8. Since the spatial shape of the interaction is different, the spectral shape of the two interactions peak will differ as well. The PNC interaction over frequency will be one narrow peak while a possible magnetic dipole interaction due to the h_z^{rf} on the holes would be wider and dual peaks. We will use this fact to verify if h_z^{rf} has been produced by the entry/exit holes for the experiment.

To calibrate the experimental signal, we need to convert the voltage signal measured by the detection system to the fractional change in population of the atom beam. We also

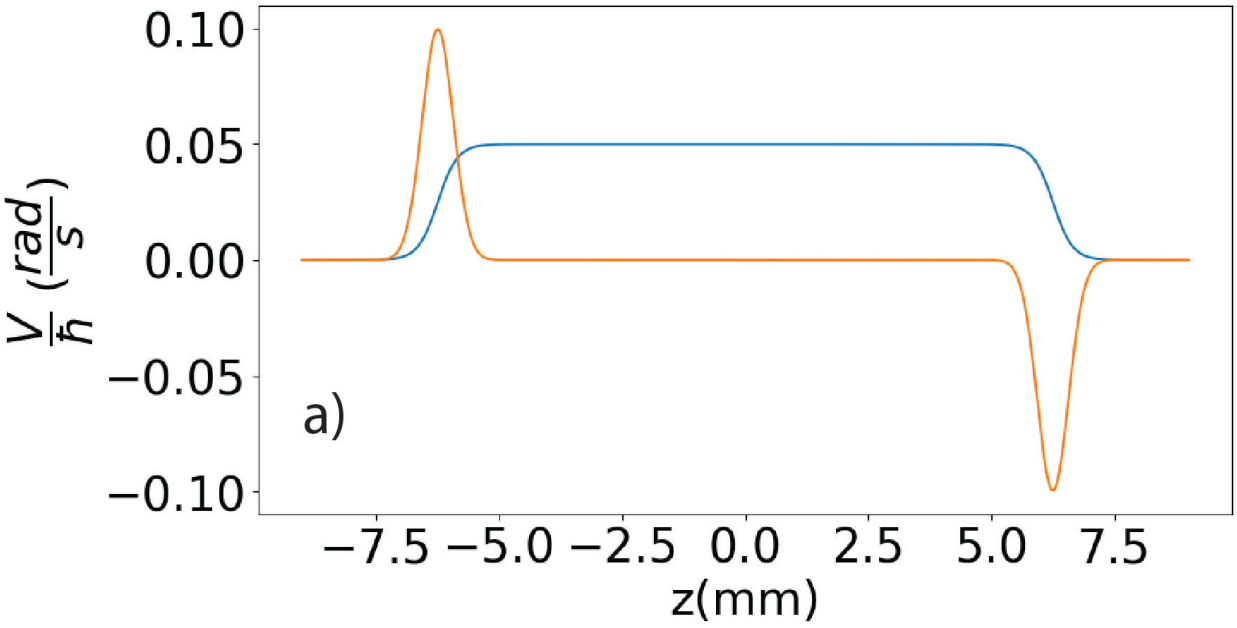

Figure 3.8. The interaction amplitudes V_m and $\mid V_{\mathrm{PNC}} \mid$ across the rf cavity along the atom beam's path.

need to convert the input rf power to the associated rf field amplitudes inside of the the rf cavity. For the fractional change in population, we first need to obtain the voltage signal for the total number of atoms in the system. We measure the detection system's voltage signal when the preparation lasers are turned off and when the preparation lasers are on. When the preparation lasers are off, the atomic beam is unpumped, and the detectable population is 9/16 of all atoms in the system (9/16 is from the degeneracy of the ground $F = 4$ and $F = 3$ states), plus background signal from scattered light. With the preparation lasers on, the $F = 4$ level is empty so only the background signal remains. The difference between these two voltages, multiplied by a factor 16/9, is the voltage of the total number of atoms in the system. To then obtain the fractional change in population, we can take the voltage amplitude of the interference of the two interactions and divide it by the voltage of the total number of atoms in the system. To calibrate the rf cavity's rf field amplitudes, we use the $\Delta m = 1$ transition peak for the rf cavity. This transition is relatively strong compared to the $\Delta m = 0$ transition and it's strength does not overly depend on the size of the transverse magnetic field or rf cavity's position, as it is mainly driven by the h_x^{rf} and h_y^{rf} field components of the TM_{010} mode. The magnetic dipole interaction for the $\Delta m = \pm 1$ transition is

$$V_m = \frac{\sqrt{(4 \pm m)(5 \pm m)}}{16} g_s \mu_B \mu_0 \left\{ [h_x^{rf} \mp \mathrm{i} h_y^{rf}] - \left(\frac{h_z^{\mathrm{rf}} [B_x \mp \mathrm{i} B_y]}{B_z} \right) \right\}. \tag{3.18}$$

We need to first tune the $B_z \sim 7G$ field to shift the peak of the $\Delta m = 1$ transition to the same rf frequency we will use for the $\Delta m = 0$ transition. This will help to ensure the shape and power of the rf fields in the rf cavity do not vary between this measurement and the final measurement of E_{PNC}. There are concerns that at a different input rf frequency, the rf equipment would react slightly different, potentially varying the rf field amplitude size due to etalon type effects in the rf equipment. We then stay at that rf frequency and ramp the rf power going to the rf cavity. The detection signal voltage is translated into the fraction of atoms in the excited state vs. input rf power. We take the experimental result for the fraction of atoms excited at different rf powers and compare it to theoretical calculations. For the theoretical calculations, we use COMSOL data of the designed rf cavity's rf fields at different rf input powers in dBm, along with averaging over the width of the atom beam

and the atomic velocity spread. We are then able to simulate the fraction of atoms excited at different input rf powers on the fraction of atoms excited. We can then verify that the theory and experiment match to be confident in converting the power output from the rf signal generator to the size of the rf fields inside the cavity. In the next chapter, one will find the experimental results of this scan, in Fig. 4.6, that match relatively well to theory.

3.4.1 Systematic Effects and Noise

A major challenge of precision experiments is identifying and controlling possible systematic effects that can impact the results of the experiment. Using our two-color coherent control technique, we expect to be less susceptible than Wood et al. [24], [38] to many systematics and other sources of noise. Our sensitivity to any noise or systematic that is not modulating at the same rate as the phase modulation between the Raman field and rf field is significantly lessened. This is due to the fact that if it is not at the same rate it will add to the dc background, whose total is of minor importance to the experiment.

There are multiple systematic effects and noise sources we considered. Some possible systematic effects that we have already discussed are the positioning of the rf cavity and the alignment of the external magnetic field with respect to the atom beam, along with the effect of the width of the atom beam. Another systematic effect of concern is possible divergence of the atom beam. If the beam is diverging, then some of the atoms would be traveling at an angle to the rf cavity mode pattern. This would cause a similar effect to the rf cavity physically being at an angle to the atom beam. Both of these effects would increase the size of the M1 interaction, with minimal changes to the PNC interaction. Additionally, we needed to consider small changes in the current of the magnetic field coils and how that will effect the system. When magnetic field in the z-direction changes, it changes the Zeeman splitting, therefore changing the peak frequency of the $\Delta m = 0$ peak. The rf frequency input for the rf cavity and the Raman lasers remain constant for the experiment. Therefore, when the peak frequency shifts it will change the relative frequency difference between the $\Delta m = 0$ transition peak and the constant rf frequency input. This will change the size of the Raman, M1, and PNC interactions. When the magnetic field coil's current vary for

the x- and y-direction, that will mainly change the amount of B_x and B_y in the interaction region. This will cause variation in size of just the M1 interaction. Additionally, we needed to consider the uncertainty of how polarization imperfections of the Raman lasers effect the size of the transition peak due to the Raman interaction. We worked hard throughout the experiment to understand and minimize all of these effects on our system.

Additionally, we worked to optimize the signal-to-noise in our system. To optimize the signal size we optimized the optical pumping into one (F, m) level. This would allow us to obtain a higher amount of usable atoms from the atoms coming out of the oven. (Though as a note over the course of the experiments done in the next chapter, we found that this optimization depended heavily on the magnetic field in the pumping region. We sacrificed the optimal magnetic field in the pumping region to maintain the optimal magnetic field in the interaction region.) To observe the pumping, we can use the Raman lasers to scan the rf frequency spectrum and observe how much of the population is pushed to one of the states on the scan with the Zeeman laser on versus off. One can then optimize the position of the Zeeman laser and the magnetic field value to reduce all of the peaks except the edge state peak. The scan of the rf frequency will end up being on the order of 10's of MHz to see a sufficient number peaks (the peaks are separated by about 2 MHz for $B_z \sim 7$ G). The rf cavity is of limited use for this particular measurement due to the full-width half-max of the resonant frequency peak being about 5 MHz. Therefore over the whole rf scan one will observe the change in rf cavity's power along with the change in peak height due to better optical pumping, making it hard to differentiate between the two. We also changed the nozzle on the atom beam oven to a 1 mm aperture instead of an array of capillaries (0.8 mm inner diameter) that is in $\sim$1 cm aperture used previously [71]. This reduced the amount of atoms making it into the vacuum chamber. This reduced the background level the detection signal, therefore most of the detection signal to be due solely to atoms from the interaction region. This helped to reduce the shot noise for our system. We were able to increase the signal-to-noise in our system.

3.5 Physical Setup

In this section, I will explain the experimental setup for the anapole moment measurement. I will go into more detail of the required setup for the Zeeman and hyperfine lasers to pump to the appropriate state of interest. I will discuss the magnetic field coils used to set up of the necessary magnetic fields. Additionally, I will describe the setup needed for implementing the Raman and rf fields. Finally, I will discuss the sources of noise for the system.

3.5.1 Optical Pumping and Detection Setup

For our experiment we need to carefully select the initial hyperfine state using the optical pumping lasers as described earlier. There are two possible initial F=3 states that our optical pumping lasers will 'push' most of the atoms into, the extreme m = ± 3. Over the course of the experiment we planned to use both starting states to explore different systematic effects and assure ourselves we have successfully reduced them. We can change the polarization/frequency of the Zeeman and hyperfine lasers to select the initial state. We are not able to use the starting state of F=4, as our pumping technique pushes all of the atoms to the extreme m state, and there is no F=3 m=±4 state for the Δm=0 transition.

3.5.2 Magnetic Fields

We use a variety of magnetic field coils in different regions for our experiment to setup different magnetic fields in each region, seen in Fig. 3.9. Some of the field coils were fabricated by previous graduate students.

Jungu Choi, the previous graduate student working on the experiment, built two dc magnetic field coils in order to create a uniform dc magnetic field in the z-direction (atomic beam direction) in the interaction region. The set of square magnetic field coils in a Helmholtz-esque setup help create a uniform magnetic field in the z-direction over both the Raman and rf interactions. The length of each side of the square is 23 cm and each coil has 560 windings of 26 AWG magnetic wire. Three-quarters of those windings were added after he left to ob-

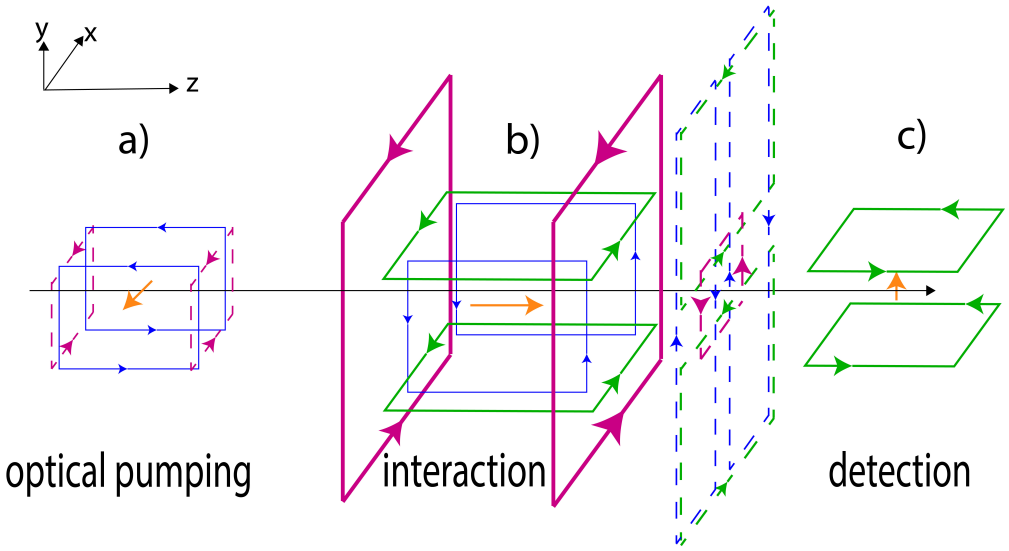

Figure 3.9. Magnetic field coil configuration in the vacuum chamber. The black arrow line through the center is the direction and rough placement of the atom beam. Not pictured are three pairs of coils outside of the chamber to cancel the earth's magnetic field in the x-, y-, and z-direction. The color of the coil represents the direction of magnetic field it produces: magenta is for a magnetic field in the z-direction, green is for a magnetic field in the y-direction, and blue is for a magnetic field in the x-direction. A solid line in the coil means it's main purpose is to produce an offset field in that direction and a dotted line coil means it's main purpose is to produce a gradient field in that direction. The direction of the arrows of the coils is the direction of current. The orange arrow is the wanted direction of the magnetic field in that region.

tain a stronger magnetic field. More details on their construction can be found in Ref. [80]. The magnetic field in the z-direction in the interaction region will lift the degeneracy of the Zeeman sublevels, which will cause the state energies to shift by:

$$\Delta E = m * g_F * \mu_B * B_z \tag{3.19}$$

g_F is the Lande g-factor, μ_B is the Bohr Magneton, m is the Zeeman sublevel, and B_z is the magnetic field applied. This results in a -0.35 MHz/G splitting between consecutive Zeeman levels for the F=3 ground state hyperfine level and +0.35 MHz/G for F=4 ground state hyperfine level. A figure of the Zeeman splitting, along with the different allowed transitions, is seen in Fig. 3.10. This splitting enables us to target a single transition, for example from the F=3, m= +3 state to the F'=4, m'= +3 state, depending on the driving rf frequency.

Dionysios Antypas constructed the earth-canceling, optical pumping, and detection field coils. The field coils are all sets of rectangular magnetic field coils similar to the interaction field coils constructed by Jungu Choi. The earth-canceling coils help make the job of all the magnetic field coils easier by only having to produce a magnetic field in one direction. The earth-canceling coils are outside of the vacuum chamber and zero the magnetic field in the interaction region. They zero the magnetic fields due to the earth's magnetic field and other external magnetic fields outside of the vacuum chamber. In the pumping region we have field coils that create a magnetic field in the x-direction in order to increase the optical pumping efficiency into the wanted state. There are an additional two coils in the z-direction to help reduce the interaction region's field in the optical pumping region. In the detection region we have magnetic field coils that create a field in the y-direction to help improve detection. As a note of concern, the magnetic fields being used for the detection and optical pumping regions could leak into the interaction region, and vice versa. We spaced out ($\sim$ 20 cm) the optical pumping and interaction regions in order to allow the atoms to adiabatically go between the two different magnetic field directions. Between the detection and interaction region we spaced them as close as possible in order to give as much space as possible between the pumping and interaction region. A z-field in the detection region helps

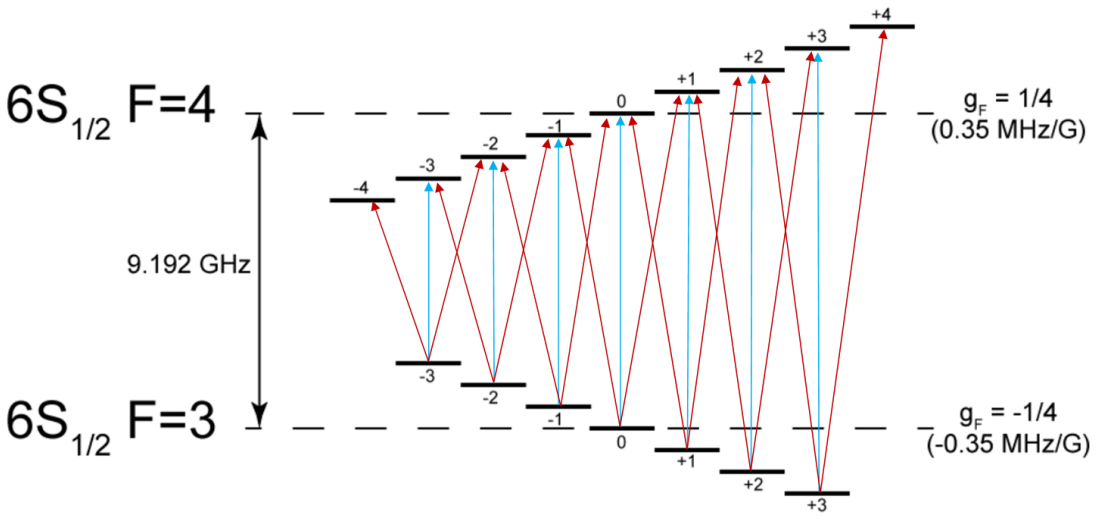

Figure 3.10. Energy level diagram of the ground state of cesium with $\Delta m = 0$ and $m = \pm 1$ transitions shown. The blue vertical lines are the $\Delta m = 0$ transitions and the diagonal red lines are the $\Delta m = \pm 1$ transitions. There are 15 unique transition frequencies due to the fact that some of the $m = \pm 1$ transitions have the same frequency, such as $m = -1$ to $m' = 0$ and $m = 0$ to $m' = -1$.

drive additional transitions and does not negatively impact the detection in comparison to the pumping region.

In the interaction region, I constructed small, controllable magnetic fields in the x- and y-direction, that were used to explore and minimize the M1 interaction. We have four coils, two for creating B_x and two for creating B_y. The coils are 15cm by 15cm, spaced about 15 cm apart. We made a box from the four coils such that they will be able to support small magnetic fields in the x-direction and y-direction in the interaction region. These coils are placed inside the bigger B_z magnetic field coils in the interaction region and mounted to the platform supporting the rf cavity. To give us the control we need, we built coils with 10 loops and used a current-controlled source. We use a source that we typically use as a laser diode current controller, as we needed control over the current on the 0.01 mA to 0.1 mA regime. Our typical laser diode current controllers can provide the necessary control. (In the current configuration a 1 mA change in current will give a 1 mG change in field.) As a note for the future experiment, it was decided that the four coils would need to be bigger in order to produce less of an arch in the profile of B_x and B_y fields over the rf cavity as we were finding it cumbersome to get rid of those gradients across the cavity.

Finally, in between the interaction and detection region we have B_x and B_y tweaking field coils that I constructed. We use 4 coils to be able to create a gradient B_x and B_y field to correct the gradient, such that B_x and B_y are uniformly zero throughout the rf cavity. Two are placed side by side with a spacing of 4 cm between the two coils to allow the atom beam to go through. Each coils was made as big as possible within limitations of space inside the vacuum chamber. Therefore, the far side wires have minimal impact and the side closest to the atom beam can create a gradient B_x or B_y field. They were constructed similarly to the small controllable fields in the interaction region but with 25 loops. The setup was placed closer to the detection region than the pumping region due to space limitations in the chamber, which was about 20 cm away from the center of the interaction region.

We also want all of the magnetic field coils to be stable over the length of the measurement time. If the fields in the z-direction drift too much, it will change the Zeeman shift, causing the transition frequency to change. Once the transition frequency shifts off of the driving frequency, the transition amplitude of the PNC interaction will lessen. This will increase the

necessary integration time. More importantly, the drifts could be in the x- or y-direction. This would effect the amount of the M1 interaction present in comparison to the PNC interaction, which we require to stay fairly constant. We acquired low noise power supplies (Keysight E36313A) for all of the magnetic field coils, besides the interaction region's B_z coils, to be able to ensure that drifts in the current were on the order or less than 0.1 mA. The typical current magnitude is around 100 mA to 1 A. The line/load regulation of the Keysight units is 0.01%+250 μA. For the interaction region B_z coils we found that the Keysight E36313A still varied too much, which we could see on the peak of the Δm=0 transition varying over time. Instead we used a current controller for a diode laser that has improved current regulation (ILX Lightwave LDC-3744B). The output current variation was less than 20 μA for the Lightwave and we could no longer observed the peak of the Δm=0 transition varying over time.

3.5.3 Raman Lasers

For the Raman interaction, we needed two phase-locked lasers whose frequencies are ~9.2 GHz apart. We initially tried optical injection locking, similar to Ref. [81]–[83], but found that it did not stay locked for long enough and required too much maintenance time to keep working (both with two lasers locked 9.2 GHz apart and three lasers each locked 4.6 GHz apart). Instead, we ended up using two external cavity diode lasers (ECDL). One laser was locked to a saturated absorption setup about 80 MHz detuned from the $6p_{3/2}$ F=2 using an AOM (or 230 MHz from the $6p_{3/2}$ F=3 state, which is the lowest state the Raman lasers can excite in our current setup). The second laser was locked to the first using a Vescent D2-135 Offset Phase Lock Servo at 9.2 GHz away. A simple diagram of the setup may be seen in Fig. 3.11. We explored different powers of the two Raman lasers (both individually and together), along with varying the detuning from the $6p_{3/2}$ state, to achieve a 50-50 mixture of the ground and excited states. We found that we had to carefully control the ratio of the two Raman lasers to help control the ac Stark effect. The ac Stark shift is opposite coming out of the ground F=3 or F=4 state, therefore increasing the strength of one of the Raman lasers ended up increasing the resonant frequency of the Raman transition while increasing

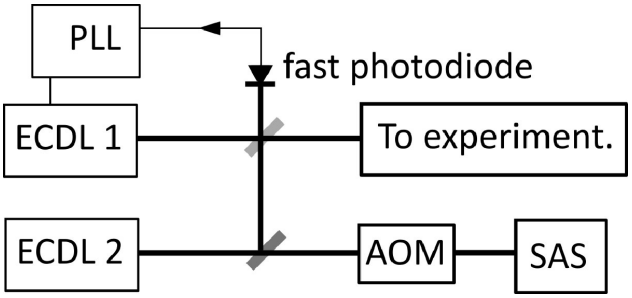

Figure 3.11. Raman laser setup using a phase lock loop (PLL) from Vescent to create two Raman beams that are phase locked and 9.2 GHz apart. Abbreviations used in this figure are: external cavity diode laser (ECDL), acousto-optic modulator (AOM), and saturated absorption setup (SAS). (For the AOM and SAS setup we are using them to lock the laser to a detuning away from the cesium transition.)

the strength of the other would decrease the resonant frequency. In the end, we optimised the power ratio by keeping the Raman transition peak as narrow as possible, which ended up with a power ratio of 2 (the laser tuned from the $6s$ $F = 3$ state needing half as much as the one out of $6s$ $F = 4$). We assumed the narrowest peak would occur when the net ac Stark effect was at a minimum, which was reinforced when we tested the interference with the rf cavity, as seen in the next chapter. We also found that having less total power in the lasers made it easier to keep a narrow Raman peak, along with less scattered light on the detection photodiode. We therefore decided to have the Raman interaction be 80 MHz detuned from the $6p_{3/2}$ F=2 level.

3.5.4 RF Cavity

To shape the rf field in the vacuum chamber, we originally used a parallel plate transmission line (PPTL) designed by Jungu Choi, seen in Fig. 3.12 and described in more detail in Appendix B. We later found that, particularly at high rf powers, rf leakage from the PPTL caused effects that we could not understand or control. Additionally, due to the structure of the magnetic field of the PPTL, we found that the sensitivity of a small detuning away from the resonance, less than 1 Hz, would cause M1 to completely swamp the PNC signature.

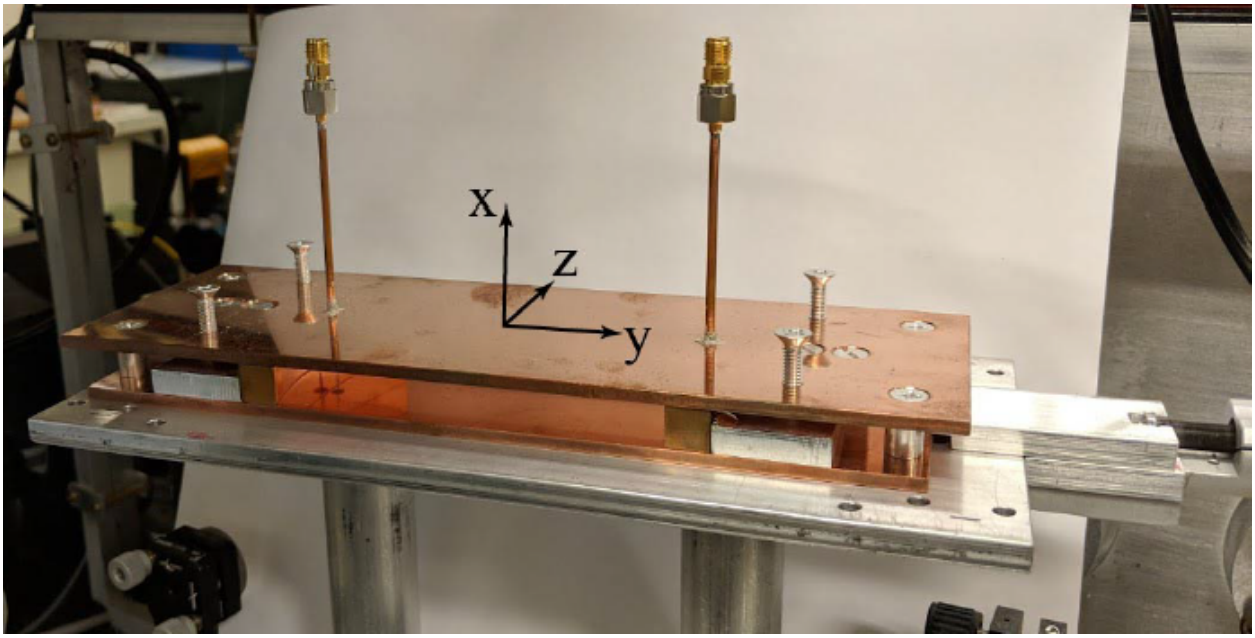

Figure 3.12. Picture of our old PPTL plate.

We decided to design a new rf cavity that would solve both of these problems. The first iteration of the design can be seen in Fig. 3.13, with the machine version later in Fig. B.6. After some testing we discovered that the cavity design allowed a strong-unwanted magnetic dipole interaction at the atom entry and exit holes that we could not get rid of, more detail is in Appendix B. The final design can be seen in Fig. 3.14 and with the machine version later in Fig. 3.15. We found the new design would reduce the unwanted magnetic field on the atom entry/exit holes due to symmetry. In the next chapter, we will find it further needs to be reduced.

The final design of the rf cavity assembly consists of a central 'science' chamber, flanked by two 'excitation' chambers. We chose to use two excitation chambers instead of directly exciting the science chamber to keep the science chamber's mode more pure. The rf power enters on a coaxial feedthrough into one or both excitation chambers, depending on the needs at the time. The excitation chamber is 1.65 cm by 0.5 cm by 4 cm. The coaxial feedthroughs are in the middle of the excitation chamber on the 1.65 cm by 4 cm face. The pin of the coax is inserted such that it is half of the 0.5 cm height of the cavity. The power will be

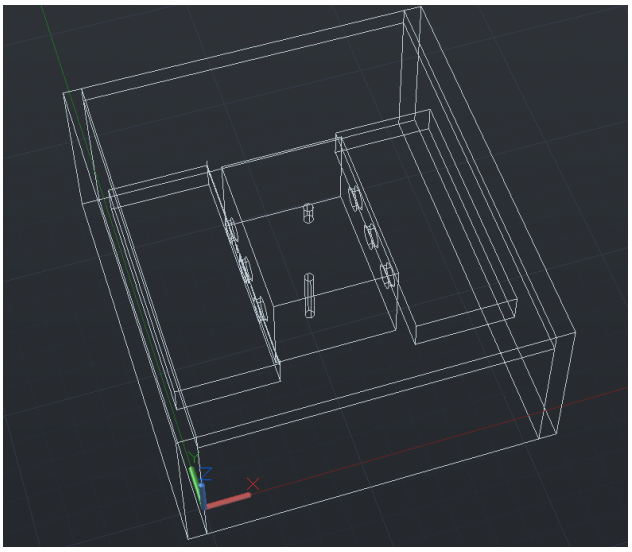

Figure 3.13. Simplified Autocad design of the first design of the rf cavity. There is no feedthrough coax pictured.

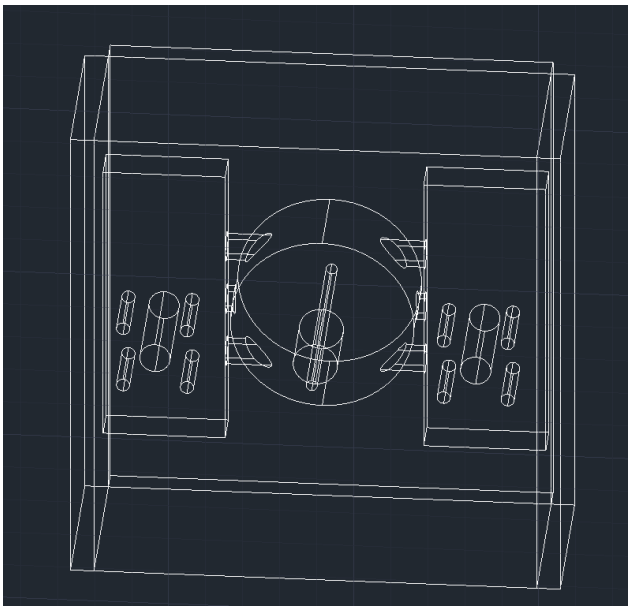

Figure 3.14. Simplified Autocad design of the final design of the rf cavity. The holes for the feedthrough coax are pictured.

transferred from the excitation chambers to the science chamber through coupling channels between the two chambers. The coupling channels are three evenly spaced holes (diameter 4mm, the center of each spaced apart 8 mm) in the middle of the side of the science chamber. In the science chamber there is an additional hole (1.5 mm diameter) through the central axis to allow the atom beam ($\approx$ 1mm diameter) to pass and be excited by the rf power. The first and second rf cavity assembly designs differs only in the science chamber. The science chamber is different in the effect that instead of being 1.8 cm long in the atom beam's path, it is 1.25 cm long. This was to help reduce the need to keep the magnetic fields uniform over a longer region as well as keeping the next nearest excitation mode over 4 GHz away for the second design. Additionally, the first design was a rectangular cavity while the second design is a cylindrical cavity with a radius of 1.241 cm. We found that due to the symmetry of the atom entry/exit holes being circular to the cavity being circular, the h_z^{rf} created due to having a hole in the cavity was reduced. Also, we found that when both excitation chambers were excited with the same phase, it further reduced the unwanted magnetic field, discussed and seen in COMSOL simulations in the next chapter.

After comparing properties of aluminium and OFHC copper, we chose to machine this out of aluminum. Both materials have relatively high electrical conductivity, can be obtained and machined with ease, and have similar thermal expansion coefficients. Aluminum has about half the electrical conductivity of OFHC copper and about a quarter bigger thermal expansion coefficient. We have currently decided to go with aluminum mainly due to being able to machine it a smaller tolerance. The smaller tolerance is of great help as it allows us to more reliably achieve an appropriate rf resonant frequency. A 1 mm size variations in any of the dimensions could easily push the resonant frequency far enough away from 9.2 GHz that we can not produce a strong enough magnetic field to use the cavity or be too close to the zero magnetic field resonance. One possible negative side-effect to using aluminium for the rf cavity is the likelihood of forming an oxide layer (copper would also oxidize). The oxide layer would effect the properties of the aluminum, though we did not see any clear evidence of this in the experiment. The finished cavity can be seen in Fig. 3.15.

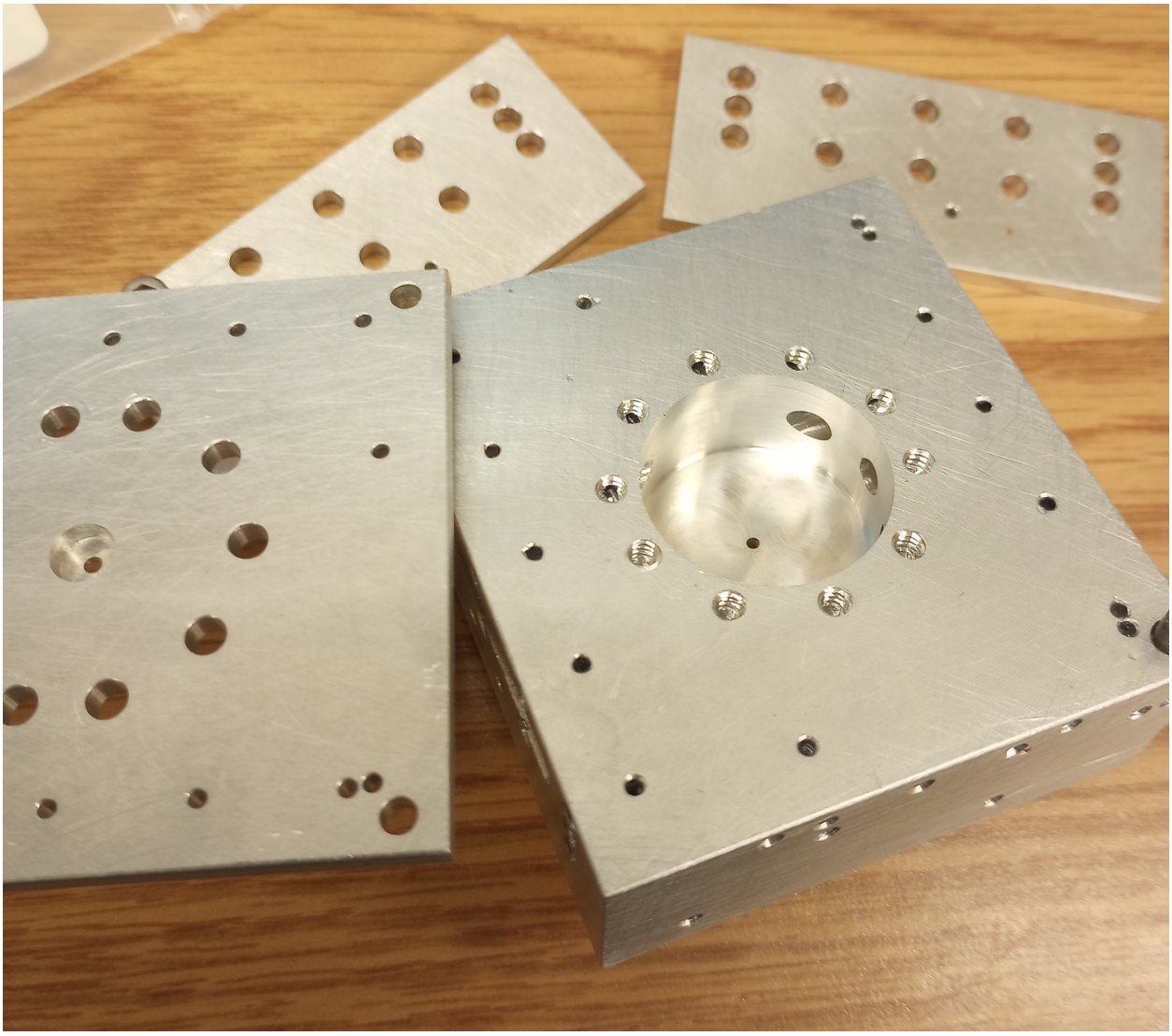

Figure 3.15. Machined version of the final cylindrical rf cavity.

RF Fields

We investigated the magnetic and electric fields that are created in the rf cavity. I have completed COMSOL simulations to investigate how the magnetic and electric rf fields would look in the rf cavity, the final cavity's design results can be seen in Figures 3.16- 3.19. During the course of the COMSOL simulations, I varied all possible lengths in the rf cavity to find the optimal sizes to maintain a strong and pure field inside of the rf cavity. In the final design's COMSOL simulations, both excitation chambers were excited with 1 W of power, in phase with each other, at a frequency of 9.2 GHz. The 9.2 GHz is near the peak of the resonance for the dimensions of the simulated cavity. The TM_{010} mode is excited, the lowest order mode. The fields of interest are the electric rf field, ϵ_z^{rf}, and the magnetic rf fields, h_x^{rf}, h_y^{rf}, and h_z^{rf}. The main difference between a perfect TM_{010} mode and the COMSOL simulations with necessary holes, is that h_z^{rf} is introduced into the rf cavity at the atom entry/exit holes, along with the 'turn on and off' of the rf fields at the edges of the cavity being less steep.

RF Source

The sources of the rf power for the experiment comes from a Berkeley Nucleonics 845 RF Microwave Signal Generator (BNC) for the 9.2 GHz rf signal and a Agilent E4420B for the 143 MHz rf signal. These sources allow us to output a wide range of frequencies, along with being able to sweep the output power, phase, and frequency, for the rf signal. The setup of the components to get the two sources phase coherent and to transfer the rf power from the sources to the rf cavity and Raman lasers are seen in Fig. 3.20. The phase shifter inserted in the path to the excitation chamber of the rf cavity gives us control over the phase difference between the two inputs of the rf cavity. This allows us to optimize the phase difference between the two inputs to have the two incoming rf fields add constructively or destructively in the rf cavity. Additionally in each path are circulators that act as isolators that allow rf power to the rf cavity inputs and stop rf power from going back along the rf path to the rf source. This will help protect the rf equipment, like the rf power amplifier and the rf source. Additionally, it will allow us to monitor the power transmitted through the cavity from one

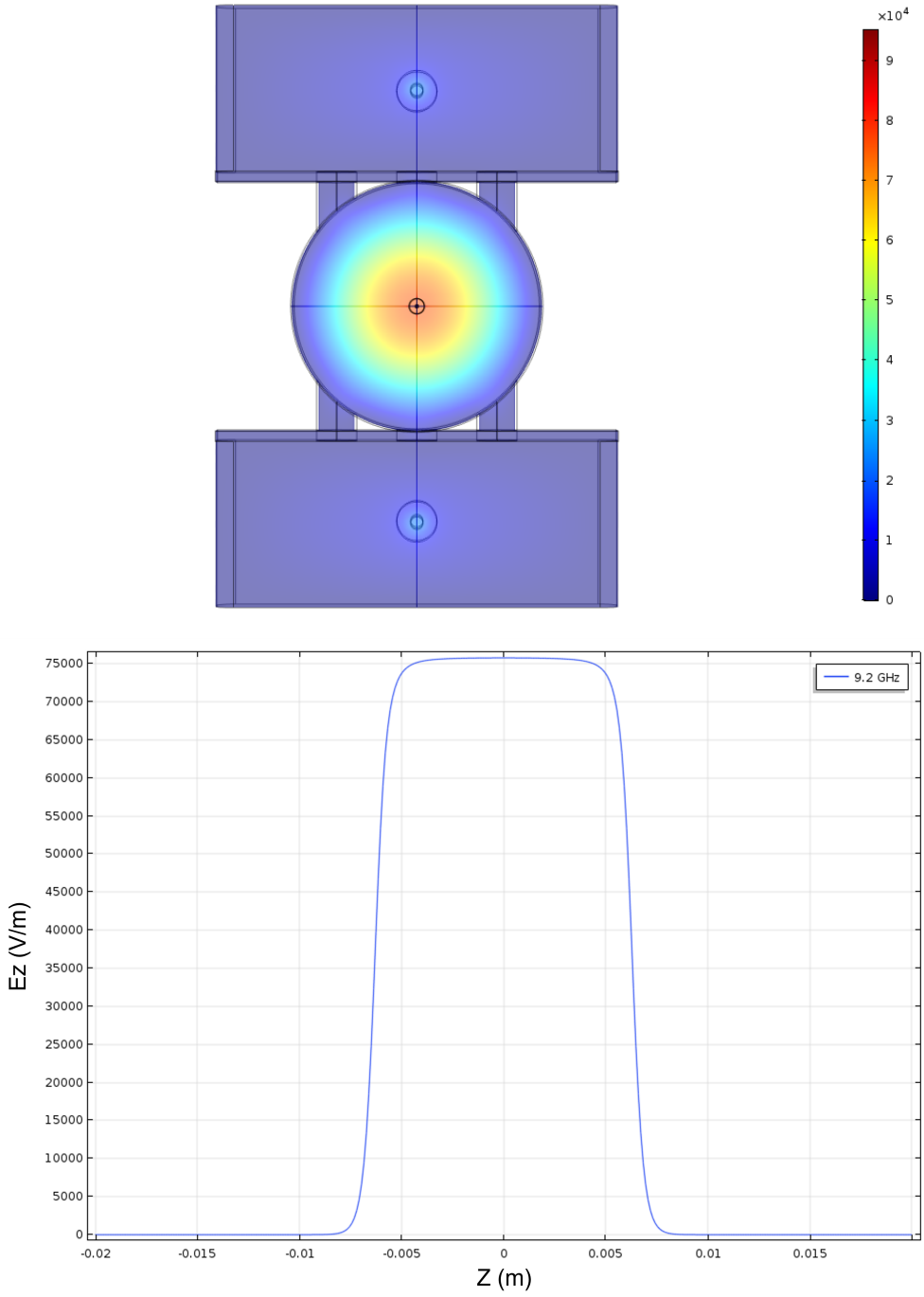

Figure 3.16. (a) Gradient map of the magnitude of the rf electric field ϵ_z^{rf} (units of color-bar are V/m) and (b) electric field cut out along atom beam path (out of the page in this picture at the center, marked by two concentric circles).

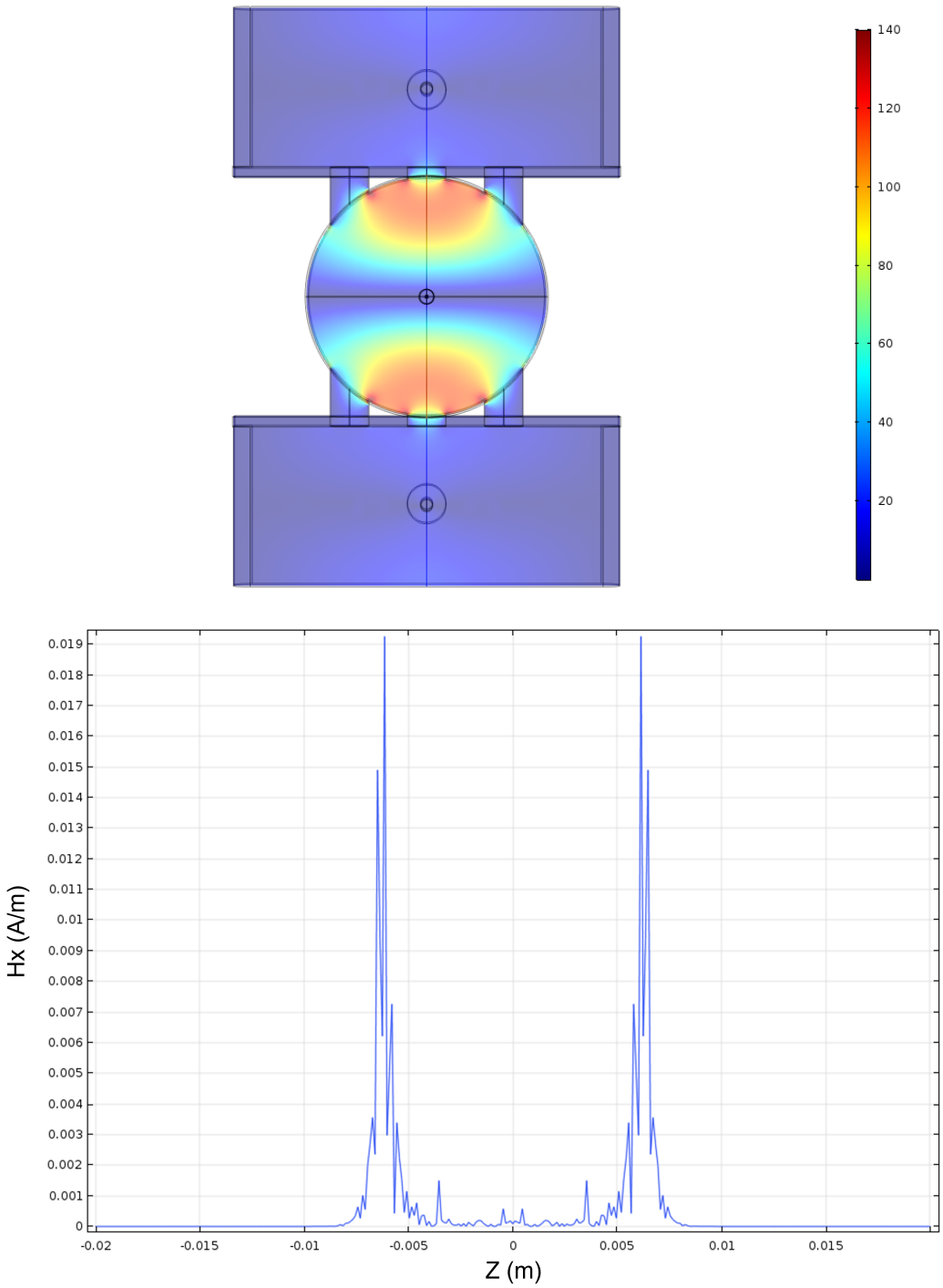

Figure 3.17. (a) Gradient map of the magnitude of the rf magnetic field strength of h_x^{rf} for the lowest order mode supported by the rf cavity. The field is small, but not quite zero, along atom beam direction (out of the page in this picture at the center, marked by two concentric circles) (units of color-bar are A/m) and in (b) the field cut along the atom beam path.

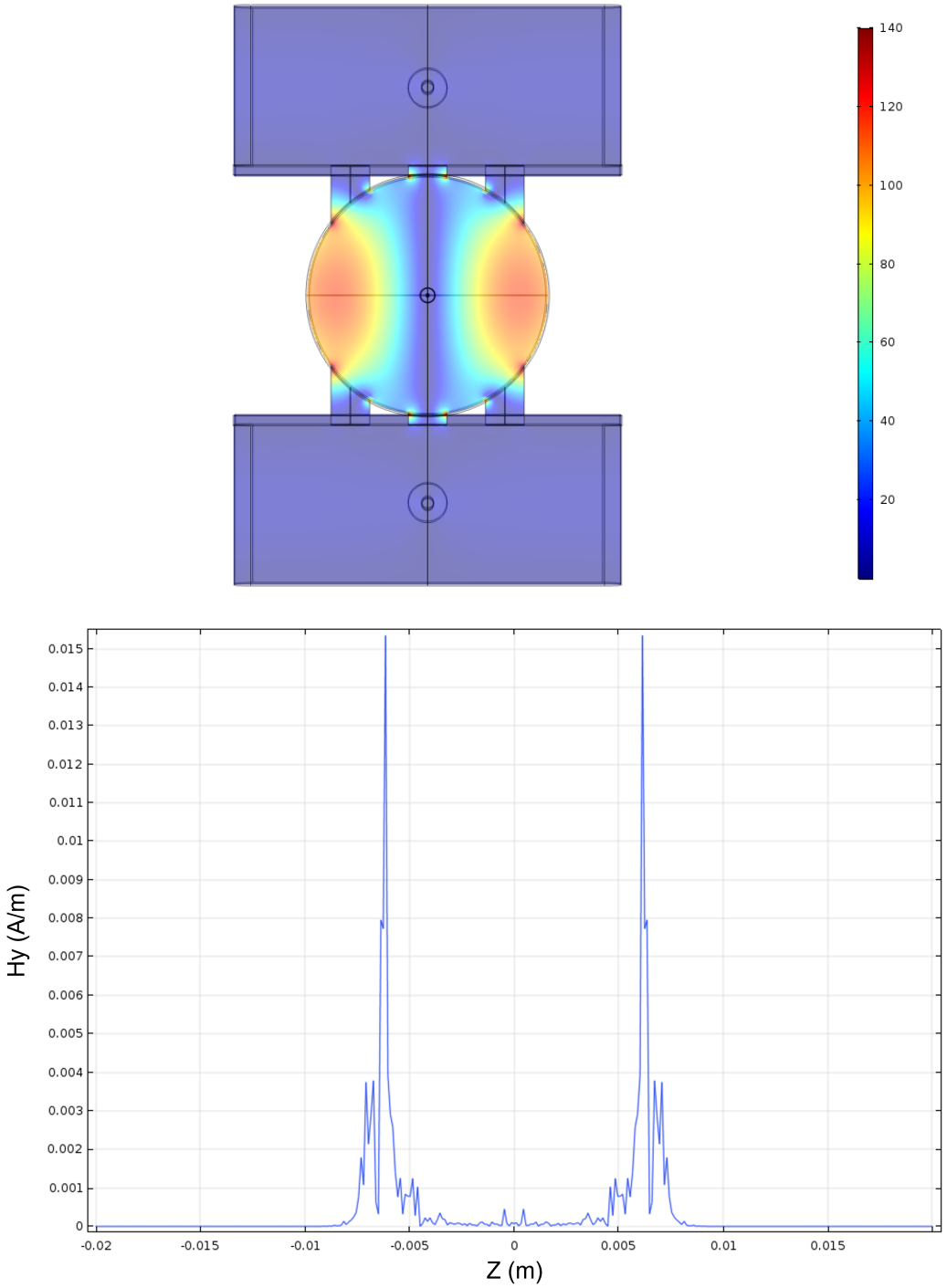

Figure 3.18. (a) Gradient map of the magnitude of the rf magnetic field strength of h_y^{rf} for the lowest order mode supported by the rf cavity. The field is very small along atom beam direction (out of the page in this picture at the center, marked by two concentric circles) (units of color-bar are A/m) and in (b) the field cut along the atom beam path.

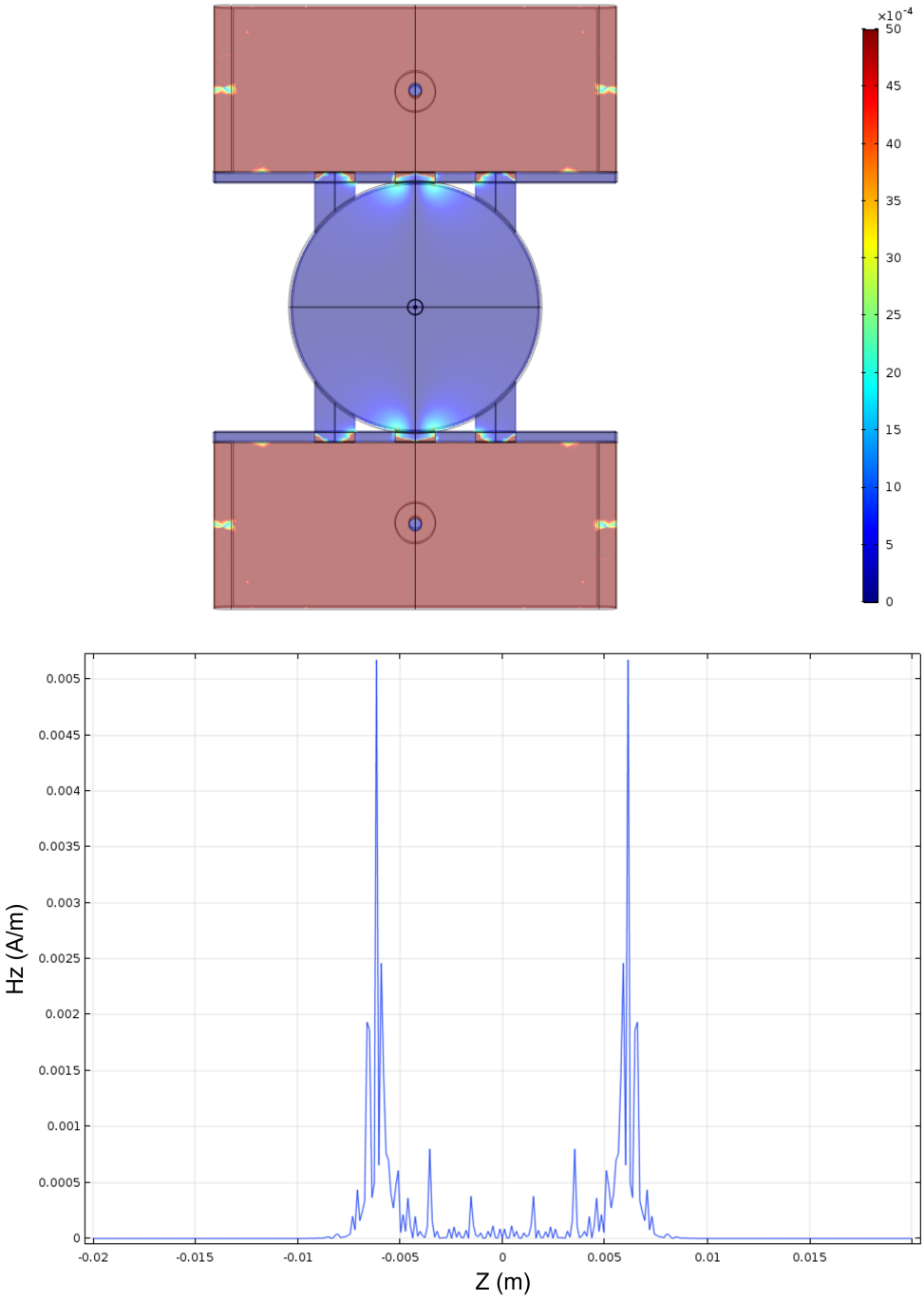

Figure 3.19. (a) Gradient map of the magnitude of the rf magnetic field strength of h_z^{rf} for the lowest order mode supported by the rf cavity. The field is zero along atom beam direction (out of the page in this picture at the center, marked by two concentric circles) (units of color-bar are A/m) and in (b) the field cut along the atom beam path.

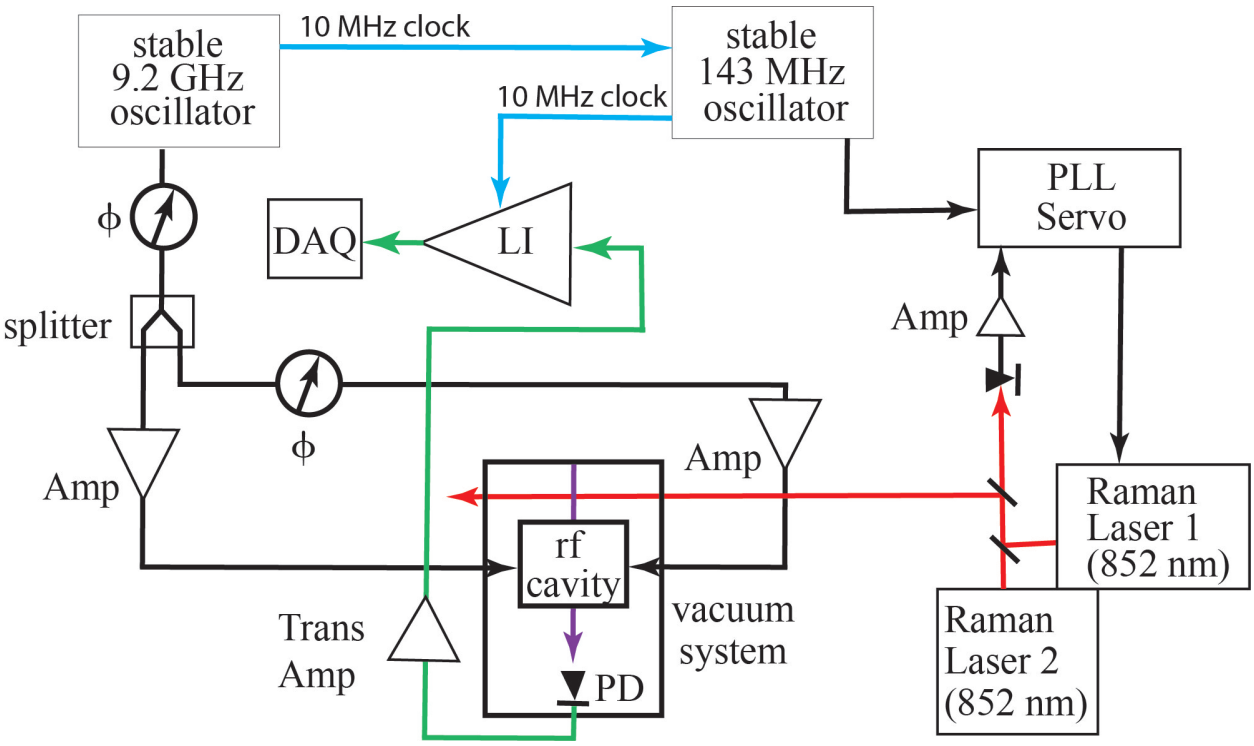

Figure 3.20. Diagram of rf power to the rf cavity and method of phase locking the Raman interaction to the rf interaction. Notation in the figure: red lines show the path of the output of the Raman lasers, PD is a photodiode, ϕ is a phase shifter, PLL is a phase-lock loop, LI is a lock-in amplifier, DAQ is the data acquisition system, AMP is an amplifier, and the blue lines are the reference clock (10 MHz clock).

excitation chamber to the other. The setup of the rf equipment is essentially the same as when we were using the first rf cavity design. In Chapter 4, I will discuss the experimental steps to verify that we had the necessary coherence between the sources to allow our setup to work to measure E_{PNC}.

3.5.5 Noise in the Setup

To choose the optimal interference frequency of the signal, we investigated various sources of noise that were affecting our system. For this experiment, the most significant noises are the ones that occur at the same rate as the interference frequency between the rf and Raman interactions. We therefore carefully analyzed the noise level at different frequencies in our

Table 3.2. V_{rms} noise with 1s integration time at 150 Hz.

Source	V_{rms} ($\mu V/\sqrt{\text{Hz}}$)
detection laser	0.8
optical pumping lasers	1.2
Raman lasers	3.5
shot noise	20
Johnson noise	6
op amp voltage noise	0.04
op amp input current noise	0.5
total	21

system to select the quietest frequency by sending the signal output into a Fast Fourier Transform (FFT) analyzer. We found that electrical interference at 60 Hz and its harmonics were the worst offenders, along with low frequencies in general. Additionally we have an upper limit on the rate due to the wide speed range of the atoms from the oven and an averaging affect of different atomic velocities from collecting too fast. With those facts in mind we chose 150 Hz as the interference frequency. We discuss the noise level from different sources at 150 Hz with a bandwidth of 1 Hz in the following paragraphs.

We looked at the effect from different sources noise at 150 Hz with a bandwidth of 1 Hz, seen in Table 3.2. We used theoretical calculations, data sheets for electronics, and the lock-in amplifier to obtain the values. The first source of noise to consider is the noise from the detection system circuit, which was designed by George Toh [37]. There are three main outputs from the circuit. We used the output that first went through a transimpedance amplifier, which uses a 20 MΩ resistor to convert the current to a voltage signal, and then an additional 10 times gain stage to the amplify the signal further. There is Johnson noise from the transimpedance amplifier of the circuit. At our current temperature for the circuit, we estimate a V_{rms} of 6 $\mu V/\sqrt{\text{Hz}}$ from the calculations on our signal. There is also noise coming from the op amp (OPA827) itself in the transimpedance amplifier: the input voltage

noise is 0.04 $\mu V/\sqrt{\text{Hz}}$ and the input current noise is 0.5 $\mu V/\sqrt{\text{Hz}}$ from the op amp specs and after the 10 times gain stage.

The signal size of the Raman interaction and scattered light contributes to the shot noise. With the current level of the 50:50 Raman interaction being about 1 V, and our atomic beam characteristics, the shot noise V_{rms} is 20 μV for a 1 s integration time. We followed the steps and calculations from Dionysios Antypas's thesis [71] for the shot noise value. Background atoms and scattered light add to the statistical noise of the system by raising the voltage level in our system. Over the past years we have reduced this voltage level to a DC voltage of around 20 mV on the 10x gain stage of our detection circuit. One key way to decrease this background signal was by keeping the detection windows on the vacuum chamber clean of cesium build up.

We next looked at the noise coming from the different lasers we are using for the experiment. We used the lock-in amplifier to observe the voltage variations in the amplitude of each laser using a photo-diode. The 852 nm detection laser had V_{rms} noise of 0.8 $\mu V/\sqrt{\text{Hz}}$ on it, along with similar amounts on the two optical pumping lasers with 0.8 $\mu V/\sqrt{\text{Hz}}$ on one and 0.9 $\mu V/\sqrt{\text{Hz}}$ on the other. The two Raman lasers locked together at 852 nm did end up having more noise on them, with their effective noise together at 3.5 $\mu V/\sqrt{\text{Hz}}$. In addition, if the power varies for either/both of the Raman lasers in the atom beam at any rate, that would effect the ac Stark effect from the Raman lasers. This would change the resonant frequency of the Raman interaction and therefore the overlap of the rf and Raman interactions. We used an AOM power stabilizing circuit to reduce this effect. With the current stabilization we did not observe an error due to this effect. Without the power stabilizing circuit, a shift in the Raman interaction's resonant frequency was noticeable in the amplitude of the interference signal of the Raman and rf interactions on the time scale of a couple of minutes. We used a saturated absorption lock setup on the second Raman laser not stabilized by the phase lock loop (PLL) circuit from Vescent. When the frequency of the Raman interaction detuning varied, the amplitude of the Raman interaction would vary. Without the laser offset frequency locked, we found that the interference signal amplitude of the two interactions drifted noticeably on the minute time scale.

The last big source of noise comes from 'non-ideal' and changing magnetic fields. We have previously discussed the effects of 'non-ideal' magnetic fields on the rf cavity, and due to the h_z^{rf} in the cavity, we were only able to confirm that we could get the B_x and B_y fields down to less than 30 mG. When compared to the $B_z \sim 7G$ field, these transverse fields are less than 0.3% of the total magnetic field. We also needed to change the current source for the B_z field as we found the old unit's regulation of the current caused the B_z field to slightly oscillate, which we noticed while watching the interference signal of the two interactions. With a new unit that has better current regulation, the oscillating signal went away. The new unit's specifications keep the Zeeman shift to less than a 200 Hz shift in a 150 kHz bandwidth. In a 1 Hz bandwidth at 150 Hz, assuming a flat power density across frequency for the unit, there should be less than a 0.6 Hz shift. With the new unit the magnitude of the interference signal of the two interactions did not change over the course of 30+ minutes (during which, no intentional changes where made to vary the signal). Another note of concern with the **B** fields is 60 Hz magnetic fields from the room's power strips and other powered electronics. We did not observe effects from this in our system, but for the final experiment we will have a signal 3 to 4 orders smaller than our current one. For future experiments they could become an issue. Finally, one will have to watch to ensure that the Earth's magnetic field shifting over time is not effecting the experiment.

In the next chapter, I will discuss the experimental results from the setup described in this chapter.

4. EXPERIMENTAL DATA

In this section, I will discuss the experimental steps I took to explore and understand the rf cavity and Raman interactions. I will then discuss the frequency dependence of the interference signal of the two interactions and what we believed caused the signal shape. I will also discuss the details on zeroing the B_x and B_y magnetic fields in the interaction region. Finally, I will discuss the next step/design of a new rf cavity that we are exploring to be able to successfully finish the experiment.

4.1 Raman Interference

Our first step to verify the experiment was viable was to test if the atoms stayed coherent over the distance between the Raman lasers location and the rf cavity location in the atom beam. In order to accomplish this we split the Raman lasers into two approximately equal power beams. We used two Raman beams, instead of the rf cavity and a Raman beam, as we wanted fewer variables to worry about (and we were still waiting on the rf cavity to be machined). The two split Raman beams would be coherent to each other and we were worried about the untested coherence of the Raman lasers to the rf cavity. We positioned one of the beams into the location where the Raman lasers would ultimately be, while the second beam's position was at the center of the rf cavity, seen in Fig. 4.1. The phase difference between the two beams was changed by a motorized stage with two mirrors that would act as a delay line for the second beam. This would change the length of one beam's path compared to the other, thus changing the phase difference, and allow us to test the coherence of the atoms over the interaction region.

We were able to successfully observe interference between the two Raman beams using the setup in Fig. 4.1. Fig. 4.2 is the experimental interference between the two Raman beams over several oscillations, with all of the preparation lasers on. The whole scan took about 8 minutes to collect and the signal is the fraction of atoms excited into the ground F=4 level by the two Raman beams (we converted the voltage signal measured by the detection system into a fraction following the calibration steps in the previous chapter). For the interference between the Raman beam and rf cavity, the signal will be modulated at a faster rate and

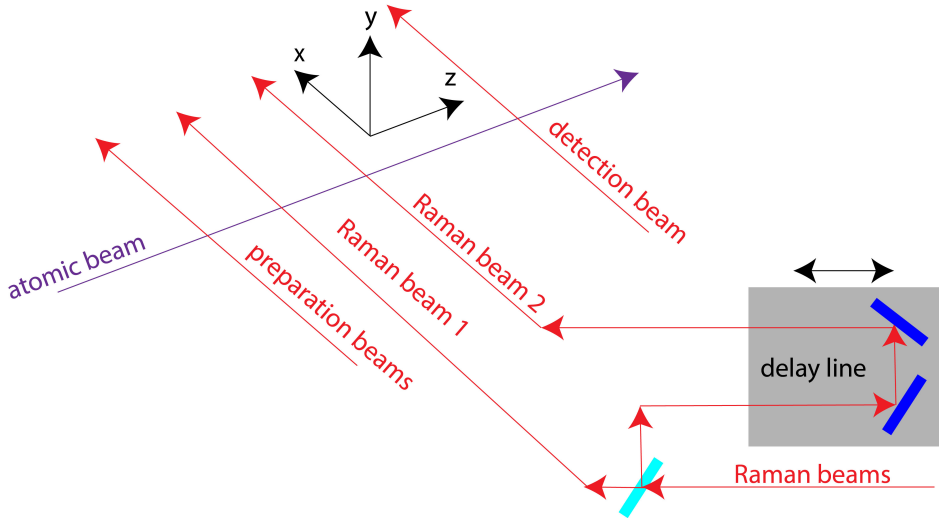

Figure 4.1. Setup for the interference between two Raman lasers. Raman beam 1 and 2 are approximately 1.25 cm apart. This figure is identical to Fig. 2.8 with the exception of Raman beam 2 instead of a rf cavity and the added delay line for Raman beam 2.

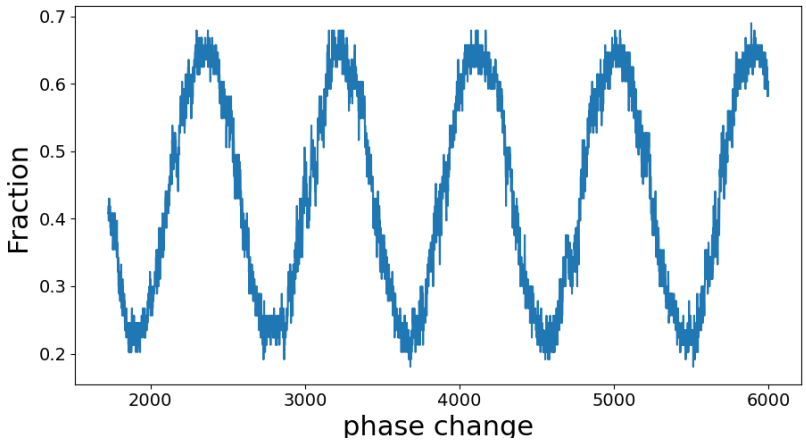

Figure 4.2. Interference between two Raman beams.

use a lock-in amplifier to reduce noise on the signal from the detection system. In the next paragraph I will discuss the amplitude of the two Raman beam interference.

We explored methods to increase the depth of modulation of the interference signal of the two Raman beams. The largest amplitude sine wave we achieved is seen in Fig. 4.2. We worked towards increasing the depth of the modulation as it would mean the atoms stayed coherent over the region and would have the necessary phase coherence to see the interference later with the rf cavity (as long as the rf cavity was coherent with the Raman lasers). We were unable to get the maximum peak difference between peaks, 0 to 100% excited, due to the difficulties in perfectly matching the power of the two Raman beams, along with the difficulty of fine tuning the first beam's power to perfectly excite half of the atoms to create a 50-50 mixture. Additionally, the Raman lasers were slightly diverging such that a longer beam path would cause the beam to be slightly bigger and less intense than a shorter one at the atom beam. In theory, if the two Raman beams were exactly the same power and shape, while exciting exactly 50% of the atoms in the system, we could achieve the maximum peak difference. We also found the delay line slightly changed the location of the second beam over the whole scan. We observed the reflection of the two mirrors would ever so slightly move in the traverse direction at the atom beam location over the 10 cm change in path length of the stage. This could cause the resonant frequency of the moving beam to slightly shift over the distance movement due to slight spatial variations in the magnetic field. (We have since improved the homogeneity of B_z through the interaction region.) When there is a B_z gradient over the region, the two Raman interactions at different positions would be resonant at slightly different frequencies. When one of the interactions moves across the gradient, it would cause the resonance to change, thus changing the ability of the second Raman interaction to be completely coherent or decoherent with the first Raman interaction. It was partly from this experiment that we decided we needed to have and use tweaking magnetic field coils to even out the magnetic field gradient, as seen in Fig. 3.9, for the final experiment. We decided the height of the interference, with our understanding of why we couldn't achieve a maximum peak difference, was sufficient to prove the atoms stayed coherent across the interaction region in the experimental setup.

Another reason for first exploring the interference between two Raman interactions was to determine and understand the experimental constraints of the two Raman lasers. It was from this exploration that we experimentally determined the optimal value of the detuning from resonance (80 MHz from the $6p_{3/2}$ F=2). We also decided on the approximate ratio necessary of the two Raman laser powers to reduce the ac Stark shift (a narrow peak) for our setup that was mentioned in the previous chapter. This was achieved by tweaking all of the available parameters (power of the individual lasers, combined power level, size of the lasers at the atom beam, detuning from resonance, etc), until we were confident in our understanding of the behavior they exhibited.

4.2 RF Cavity

After the machine shop had completed the rf cavity, seen in Fig. 3.15, we tested the resonant frequency and did our best to verify it was performing as anticipated. To test the resonant frequency we inserted rf power to one excitation chamber of the rf cavity and observed the output rf power from the second excitation chamber on a rf power meter. We then scanned the input rf frequency to observe $|S_{21}|$ vs. rf frequency. ($|S_{21}|$ is the transfer function, the transmitted power through the rf cavity divided by the power incident on the rf cavity.) We also use COMSOL to theoretically calculate $|S_{21}|$ vs. rf frequency to compare the responses. The final results can be seen in Fig. 4.3, which shows that the machined cavity had reasonably close rf resonant frequencies to the designed rf resonant frequencies from COMSOL (keeping in mind machining tolerances). As a note we could have used a vector network analysis (VNA) to make the experiment easier and more precise, but had more ready access to a rf power meter that could observe frequency in the 15 GHz range. Additionally, for the results we wanted the rf power meter's accuracy was sufficient, as we were able to verify the resonant frequencies of the machined rf cavity match well to the COMSOL simulation.

We then mounted the rf cavity on a five-axis tilt aligner stage (Newport 8081-UHV), which we installed in the vacuum chamber. The positioner is controllable from outside of the vacuum chamber and allows us to have control over the position of the rf cavity to step

sizes of less than 30 nm or an angular step of less than 0.7 μrad. With this control we were able to center the rf cavity on the atom beam and were able to explore the effect of the cavity's position on the atomic signal, as discussed further on in this section. As a note, the interference of the rf and Raman interactions would be the most sensitive to the change in the cavity's position due to the spatial cancellation of the h_x^{rf} and h_y^{rf} signal over the atomic beam. For the interference of the two interactions the spatial cancellation will lead to a

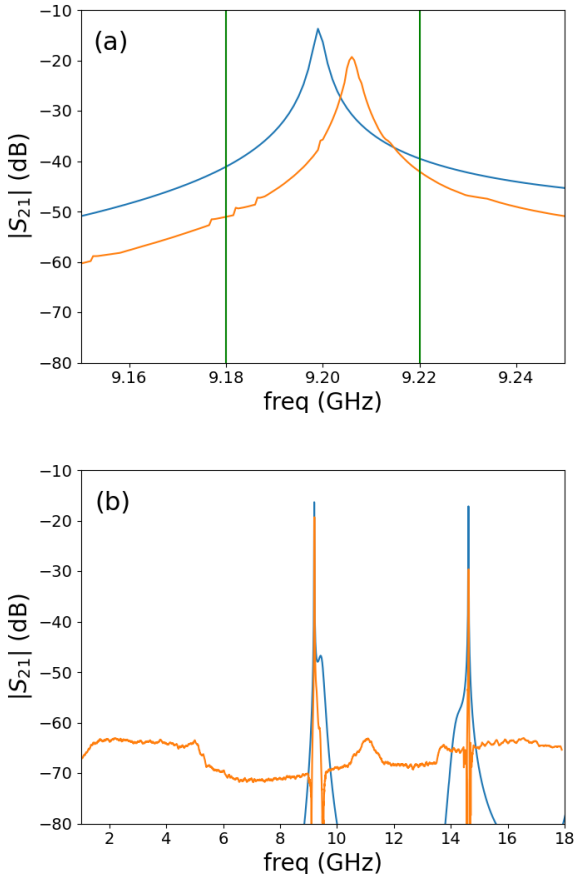

Figure 4.3. The S-parameter $|S_{21}|$ vs. frequency for the rf cavity. The orange curve is the measurement with the machined cylindrical rf cavity and the blue curve is the COMSOL simulation. (a) zoomed in on the TM_{010} peak centered at 9.2 GHz. The vertical green lines are from COMSOL simulations of the resonant frequency for variations in the cavity radius differing by 0.001" (the machining tolerance of the main cylindrical cavity). (b) Spectrum of the TM_{010} peak at 9.2 GHz and the next closest mode, the TM_{110} peak at 14.7 GHz.

signal cancellation. For just the rf only interaction, the signal cancellation does not occur. Unsurprisingly, the aligner stage moving perturbed the system and one has to wait a few seconds after the movement is stopped to observe the new atom beam signal size.

Our first step, once we got the atom beam path roughly passing through the rf cavity, was to center the rf cavity on the atom beam. To accomplish this we optimized the detection only signal (just the detection laser is on; the Zeeman, hyperfine, Raman lasers, and rf cavity are all off). The detection only signal is the simplest way to identify the strength of the atom beam making it to the detection region. As a note for the five-axis stage, the step-size going one way versus the other was not the same distance (aka 500 steps forward did not move the rf cavity the same amount as 500 steps back). We found when moving the rf cavity that we needed a $\sim$1 mm pinhole about 5cm from the rf cavity for the atom beam to travel unobstructed through the rf cavity. We came to this conclusion with the observation of the size of the detection only signal increasing/decreasing when the rf cavity started clipping the beam, with a region of constant signal over an appropriate number of steps between clipping events. When the atom beam is larger than the rf cavity atom hole, there are more steps needed between the clipping events. We were able to optimize the detection only signal using the five-axis stage to get the rf cavity centered on the atom beam, such that all of the atom beam made it through the rf cavity with no noticeable clipping.

After we got the atomic beam going through the rf cavity, we worked on zeroing the Earth's magnetic field inside of the rf cavity with the earth canceling field coils. We scanned the input frequency of the rf cavity using a 9.192 GHz rf frequency signal ramping over $\sim$1 MHz to zero the external magnetic fields, as discussed in the previous chapter. With the hyperfine laser on and the Zeeman laser off, all of the atoms will be in the ground F=3 state but evenly distributed across the magnetic sub-levels, instead of all in one extreme m level. We then looked for a peak from the rf signal (or peaks when the magnetic field is really far off from being zero). When the magnetic field is zero, all of the different m levels' $\Delta m = 1$ and 0 transition frequencies are equal and the signal becomes one narrow peak. As a note, it is important to do this at lower rf powers, such that the rf signal interacts with less than 50% of atoms. If the rf interaction is stronger there is a wider frequency spread due to the saturation of the signal and one cannot zero the magnetic field as precisely. An example of

the Earth's magnetic field canceled for the rf cavity frequency scan can be seen in Fig. 4.4, which shows the change in width of the frequency response on the signal due to a strong rf field. With the Earth's field canceled, we can use our magnetic field coils to impose the B_z magnetic field with minimal transverse magnetic fields.

When a strong B_z field is added in the interaction region, it splits all of the different m levels' transitions rf peaks, such that we can isolate the $\Delta m = 0$ transition we will be using. As long as the B_z field coils do not add a significant B_x or B_y, there will be 7 clear peaks for the $\Delta m = 1$ transitions driven by h_x^{rf} and h_y^{rf}. The $\Delta m = 0$ transition peaks will be small, but when closely investigated at the correct frequency, there are 6 peaks in total driven by h_x^{rf} and h_y^{rf} due to a small transverse magnetic field. If there is a significant B_x or B_y, then the $\Delta m = 0$ transition peaks are larger and observed more easily while scanning the rf frequency of the rf cavity. To initially find the correct $\Delta m = 0$ transition peak for

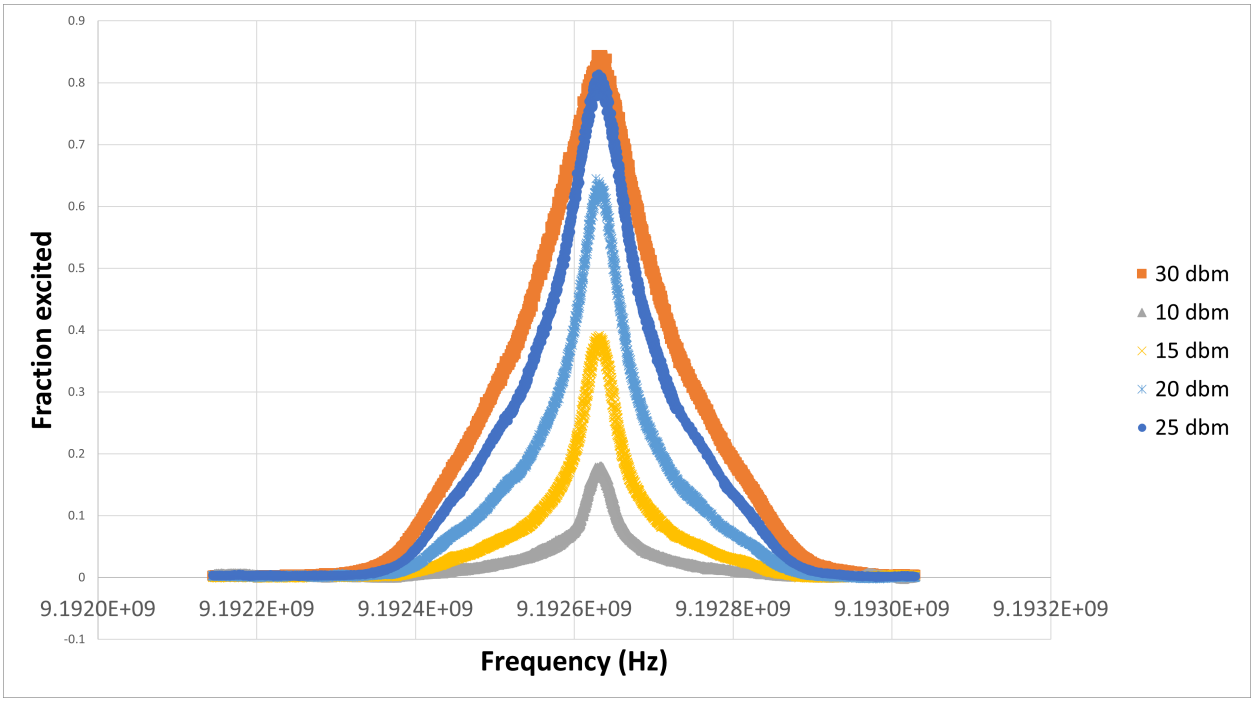

Figure 4.4. Signal due to the rf cavity with near zero magnetic field in the rf cavity. (The hyperfine and detection lasers are on and the Zeeman laser is off). The input frequency to the rf cavity is scanned over the ground state transition at different input rf power levels.

the F=3, m=±3 to F=4, m=±3 transition, I did purposefully add significant B_x and B_y. Once found, I then slowly reduced B_x and B_y while I observed the shrinking peak's resonant frequency. For the $\Delta m = 1$ transition peaks, and the $\Delta m = 0$ transition peaks with a significant transverse magnetic field, the peak shape was a single peak with no additional structure. When B_x and B_y were small in the interaction region, the $\Delta m = 0$ transition peaks were no longer a single peak as seen in Fig. 4.5. We believe that the multiple peaks of the isolated $\Delta m = 0$ transition peak comes mainly from there being magnetic field gradients along the atomic beam path in the rf cavity, which will be discussed later in this chapter.

4.2.1 Calibrating the RF Cavity

After verifying that the $\Delta m = 0$ and $\Delta m = 1$ transition peaks were mostly behaving as expected, we looked into calibrating the experimental input rf power to the theoretical COMSOL rf field size inside the cavity, as discussed in the previous chapter. We used the $\Delta m = 1$ transition peak for this; the $\Delta m = 0$ transition peak is more sensitive in height to

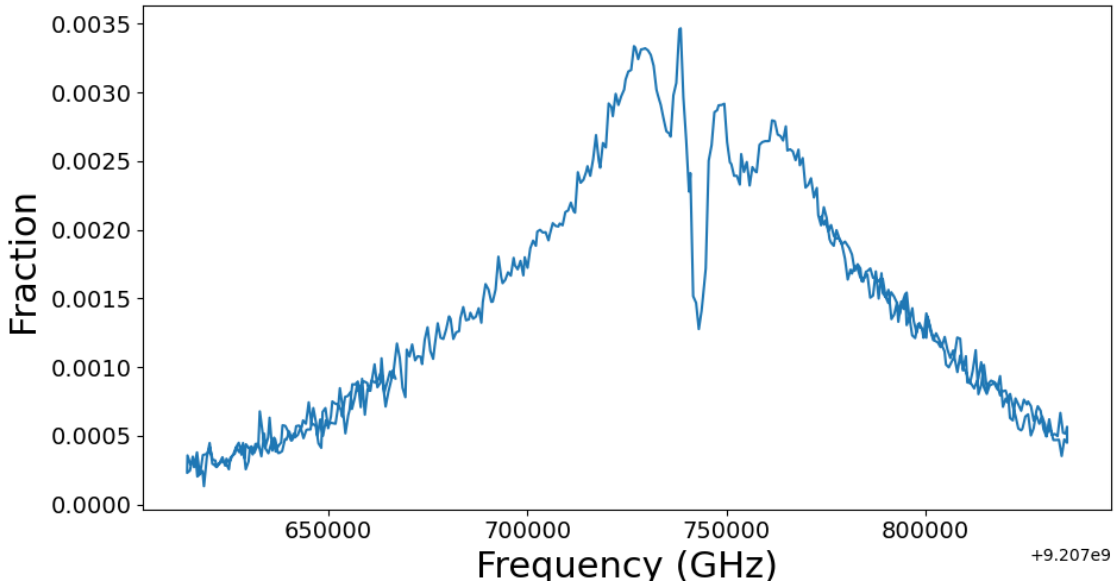

Figure 4.5. Experimental spectrum of the rf only signal for the $\Delta m = 0$ transition peak with small gradients in the B_x, B_y, and B_z across the rf cavity.

the size of the B_x or B_y than the $\Delta m = 1$ looking at Eq. 3.3 and Eq. 3.18. In Fig. 4.6, we show the experimental and theoretical rf peak's value against the outputted rf power from the signal generator unit. In the following paragraphs, I will discuss how we calibrated and obtained each of the curves.

To calibrate the y-axis of the experimental scan of Fig. 4.6 as fraction of atoms excited, we have to use several experimental measurements. First, we turned all the lasers and rf cavity off, leaving just the detection laser on; the signal size on the detection system is 9/16 of the atoms coming out of the atomic beam and any background signal from stray light hitting the photodiode. (The 9/16 is only true when detecting the ground F=4 state; when detecting the ground F=3 state the signal is 7/16 of the atoms.) We also took the detection+hyperfine+Zeeman laser voltage signal level (the Raman lasers and rf cavity are off), as only the background signal is left. Taking those two voltage values, we can then turn a voltage signal into a fraction of atoms excited out of all of the atoms in the system. For comparison with theory, we need the number of atoms that were in just the extreme F=3 m=3 level. Only atoms in that level would have been affected by the rf signal for the $\Delta m = 1$ transition peak (F=3 m=3 to F=4 m=4) we were using. To determine the fraction of total atoms that were in the m level of interest, the Raman lasers and all the preparation lasers were on, with just the rf cavity off. The Raman lasers frequency difference was scanned over the whole frequency range to obtain the fraction of atoms pumped into the extreme F=3 m=3 level as compared to the F=3 m=-3,-2,-1,0,1,2 levels. We can then take that fraction and the total atom voltage signal to transform the detection system's voltage signal into the fraction of atoms excited from the F=3 m=3 level for the $\Delta m = 1$ transition peak's height at different input rf powers for the experimental scan.

To obtain the theoretical signal in Fig. 4.6, we take COMSOL values for the h_x^{rf} and h_y^{rf} at different radii from the center of the cavity. We then calculate the fraction of atoms excited at the different radii in the atom beam. We average over the different radii across the cross section of the atom beam to obtain the calculated fraction of atoms excited over the whole atom beam. We iterate the process at different h_x^{rf} and h_y^{rf} values to trace out a changing rf power signal as we numerically calculate the fraction of atoms excited at the different values. These calculations follow the simulation steps that we used in the previous

chapter to predict the rf cavity's fields interaction. To be able to correlate the rf power for the theoretical and experimental data, we use specific values of h_x^{rf} and h_y^{rf} from COMSOL that were for the rf cavity excited with 1 W of input power into each of the excitation chambers. We obtained the experimental signal generator's rf power level for 1 W of input power at the rf cavity by calculating/measuring the losses and gains in the rf power from the signal generator's output through all of the necessary elements to the input of the rf cavity, seen in Fig. 3.20. We can then take that point of comparison and scale the various h_x^{rf} and h_y^{rf} values into the scale of the signal generator's rf power output for the theoretical curve.

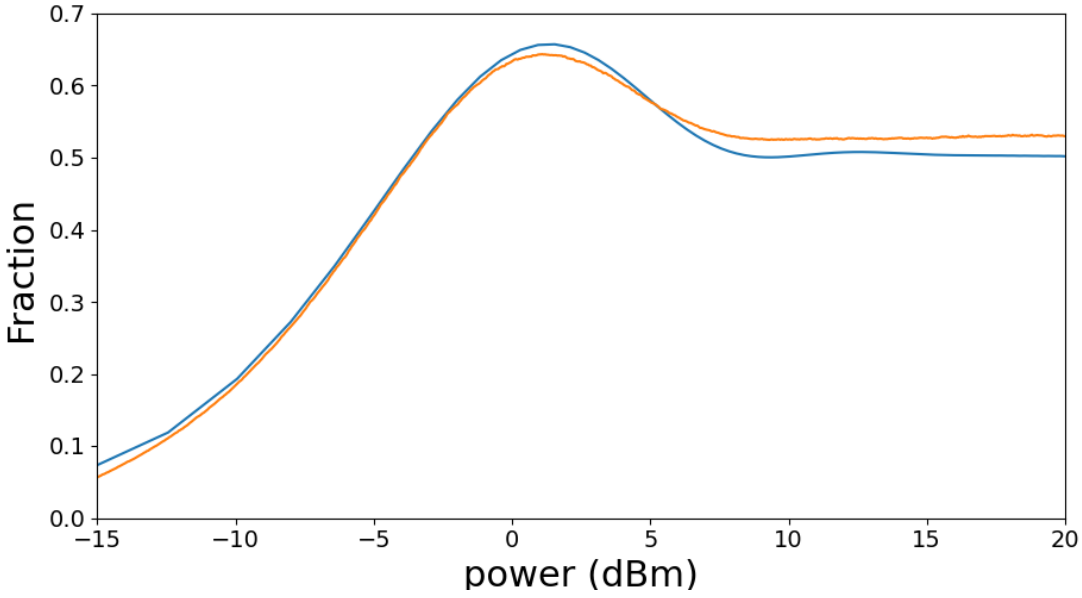

Figure 4.6. The fraction of atoms transferred from $6s\ ^2S_{1/2}\ F = 3, m = 3$ to $6s\ ^2S_{1/2}\ F = 4, m = 4$ by the rf field vs. the rf power from the signal generator unit. The orange trace is the experimental data, while the blue trace is the result of numerically integrating Eq. 3.15 and Eq. 3.16. The only adjustment needed was to the power. We adjusted the power by 3 dBm of the numerical integration to match the experimental data. The fraction excited for the experimental data fraction took into account the pumping efficiency into the $6s\ ^2S_{1/2}\ F = 3, m = 3$ to obtain just the fraction excited out of the ground $F = 3, m = 3$ state.

The final results of relating both signals can be seen in Fig. 4.6, which show good agreement between the two. The only other extra tweak we had to make to have the two scans match was to subtract an additionally 3 dBm off of the theoretical scan's rf power. We believe this difference can be explained by the machining tolerance differences between the actual cavity and the perfect COMSOL version. We found the change in the coupling channel's radius between the science chamber and excitation chamber could cause that much of a change in the value of h_x^{rf} and h_y^{rf} inside the cavity. This idea is backed up by the S-parameter $|S_{21}|$ vs. frequency scan of the machined rf cavity in Fig. 4.3. The experimental 9.2 GHz peak does not reach the same height as the theoretical peak by about $5-7$ dBm. If both of the excitation chamber's coupling channels were ~ 3 dBm less efficient in the actual cavity than COMSOL, then the transmission through the whole cavity would be ~ 6 dBm less efficient. From this measurement, we believe we understood the size of the rf power inside the cavity versus input power well enough to be able pull out the anapole moment, if this rf cavity worked (discussed further on in this chapter).

4.3 RF Cavity and Raman Interference

After verifying that we understood and could control both the Raman and rf interactions, we worked on finding and understanding their interference. We first started with a strong transverse magnetic field value, to amplify the $\Delta m = 0$ rf only transition peak. See Eq. 3.3 for the magnetic interaction. The Raman lasers' polarization allows only $\Delta m = 0$ transition peaks for the Raman interaction. We did look into the Raman laser pair polarization configuration to allow the $\Delta m = 1$ transition peaks but found that, due to cancellation between different components contributions from intermediate states, the peaks were too small. We therefore could only observe the interference between the two interactions on the $\Delta m = 0$ transition in our setup. Thankfully our setup required no adjustment to display the interference. We found interference between the two interactions as seen in Fig. 4.7. We found when investigating their interference that when the Raman peak was spectrally broad, the rf signal wouldn't interfere with the sides of the peak. The rf signal would only interfere with part of the peak near the center. We believe this is an indicator of the Stark effect broadening the

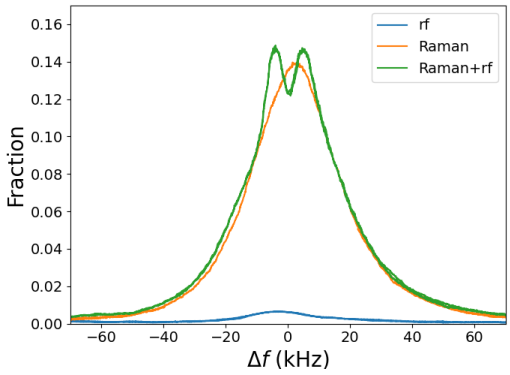

Figure 4.7. Experimental data of the $\Delta m = 0$ transition peak with a large transverse magnetic field is applied. The field size was selected such that the magnetic interaction was visible on the same scale as the Raman signal, which was reduced. The spectra are showing the fraction of the population excited to the $6s$ $F = 4, m = 3$ state from the $6s$ $F = 3, m = 3$ state vs. the frequency detuning from the transition resonance, $\Delta f = f - f_c$. Raman only is the orange trace, the rf only is the blue trace, and when both the rf and Raman interactions are turned on is the green trace. The frequency shift between the Raman and rf resonances is due to a gradient in B_z that occurred due to adding the large transverse magnetic field.

rf signal's peak. It was during this stage that we finalized the necessary power for each of the Raman lasers to reduce the ac Stark effect along with the final combined beam power, as we ensured the whole Raman peak could interfere with the rf signal.

We then explored the effect of reversing the transverse magnetic field value on the interference. We tested the prediction from theoretical calculations that the sign of the interference phase should be opposite upon reversing the transverse magnetic field, see Eq. 3.3. This is seen in Fig. 4.8. As a note for the figure, over the course of minutes the relative phase between the rf cavity and Raman lasers would drift, i.e. the position of the peak and valley in Fig. 4.8 would shift along the x-axis. We believe this is due to room temperature/pressure changing the phase of the pair of Raman lasers. Therefore we needed to collect data quickly enough in order to compare the positions of the peaks and valleys at two opposite transverse magnetic field values. For this measurement we used a saw tooth voltage signal that modulated the phase of the Raman interaction while leaving the rf phase constant,

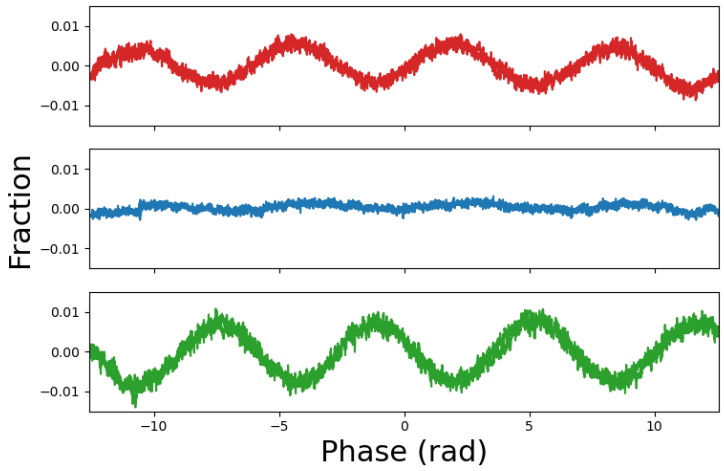

Figure 4.8. Population change in the $6s$ $F = 4, m = 3$ state vs. phase difference between the Raman and rf interactions near the resonant frequency of the $\Delta m = 0$ transition peak. The rf interaction is primarily V_m. $B_x = 75$ mG for each trace. B_y differs for the three traces. The blue trace is $B_y = 0$ mG, the red trace is $B_y = 125$ mG, and the green trace is B_y = -125 mG. Note the 180° phase shift between the red and green traces, consistent with sign change of V_m. This signal modulation (fraction) sits on top of a large dc signal, of magnitude ∼0.5 population fraction.

as discussed in the previous chapter. For the rest of the interference measurements in this chapter, we used the 150 Hz frequency difference between the rf and Raman signals to have a continuous phase difference. From the two tests in this section, we were satisfied with our understanding and control of the interference between the two interactions.

4.4 Zeroing the Transverse Magnetic Fields in the Interaction Region

Once we found the interference between the Raman lasers and the rf cavity, we started the arduous journey of figuring out the necessary current values for each of the magnetic field coils. One of the troubling parts was how many degrees of freedom we had due to the large number of magnetic field coils throughout the vacuum chamber. We first started with the rf only signal (no Raman interaction with all of the preparation lasers and rf cavity on) on the $\Delta m = 0$ transition peak, to keep the zeroing process as simple as possible. By Eq. 3.3,

the magnetic dipole contribution to the signal resulting from h_x^{rf} and h_y^{rf} can be reduced by adjusting B_x and B_y to zero throughout the interaction region, leaving just a small, narrow peak due to the PNC interaction. This peak will be too small to see over the noise in our system when the Raman lasers are absent, so we should effectively see just a straight line for the $\Delta m = 0$ transition peak. With a strong transverse magnetic field, the signal should be a relatively big, single peak. One example of an intermediate stage that took a while to understand can be seen in Fig. 4.5. We figured out at least part of the reason there were multiple peaks was due to a gradient in B_z. When B_z is not uniform over the rf cavity, it causes the atoms to be resonant at different rf frequencies across the rf cavity, widening the peak or causing separate peaks to form. We minimized the B_z field gradient by tuning the rf frequency output of the signal generator to be resonant with the nearby $\Delta m = 1$ transition peak. We tweaked the available B_z field gradient coils to make that peak as narrow as possible. We chose to do this on the $\Delta m = 1$ transition peak due to the confusion on the $\Delta m = 0$ transition peak spectral shape. Additionally, the $\Delta m = 1$ transition is stronger as it is driven by the h_x^{rf} and h_y^{rf} cavity fields, which are the primary components of the cavity mode. Even after reducing the B_z gradient, we still ended up with two peaks for the $\Delta m = 0$ transition peak we could not get rid of, as seen in the red trace in Fig. 4.9. We propose that the duel peak structure is mainly due to a gradient in B_x and/or B_y. It could be potentially due to h_z^{rf} on the entry or exit atom hole, but we found the frequency difference between the peaks better matched a gradient in the B_x or B_y magnetic field, seen later in Fig. 4.14. While we were unable to completely zero the transverse magnetic fields, we were able to reduce/increase the signal due to them by tuning the currents in the magnetic field coils. There is discussion later on in this section on the effect of unwanted magnetic fields for all of the different regions in the vacuum chamber.

Additionally, we investigated the interference signal (the Raman interaction, the rf interaction, and all of the preparation laser beams are on) when zeroing the transverse magnetic fields, seen as the blue curve in Fig. 4.9. We found the spectral shape of the rf only signal and the interference signal do not match over the same frequency range. We believe this is due to the cancellation of the signal due to the symmetry of h_x^{rf} and h_y^{rf} over the atom beam, which only occurs for the interference signal as discussed previously. Therefore in Fig. 4.9,

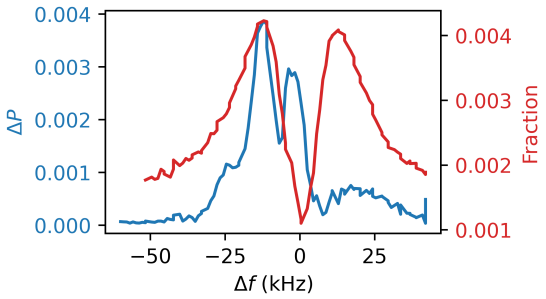

Figure 4.9. Experimental data of the $\Delta m = 0$ transition peak: the red curve is the rf only signal and the blue curve is the interference signal. Fraction for the red trace is the change in population due to the rf field where fraction=0 corresponds to zero atoms in the excited, F=4 state. ΔP for the blue trace is the amplitude of the interference modulation where ΔP=0 is the amplitude of the interference is zero.

the rf only signal we observed was the effect due to h_x^{rf} and h_y^{rf}. For the interference signal, the effect due to h_x^{rf} and h_y^{rf} is spatially canceled and we observed a different, smaller effect on the signal, details of which are discussed later in this section.

We completed more experiments to verify our inferences by changing different available variables and observing the interference signal and rf only signal when the transverse magnetic field is close to zero. When we changed the rf power, the size of both of the signals changed in height as expected. When we moved the rf cavity (without clipping the atom beam), the signals' spectrum did not change. (Clipping the atom beam reduced the signal size but did not otherwise change the spectral pattern.) When we changed either the gradient or magnitude of the transverse magnetic field, the rf only signal had a single peak change in size whose frequency was at the middle of the deep trench seen in the red curve in Fig. 4.9. The single peak rose up/down in the interference signal at the same frequency as well, but none of the other peaks changed. Additionally, the cables carrying the 9.2 GHz rf power can leak rf fields outside of the cables, which can potentially cause ground state transitions outside of the rf cavity [84]. The fields produced around the 9.2 GHz rf cables were experimentally found to be strongest near the rf cables and connectors. We added shielding to the rf cables in the vacuum chamber that reduced the leaked rf field by about two orders

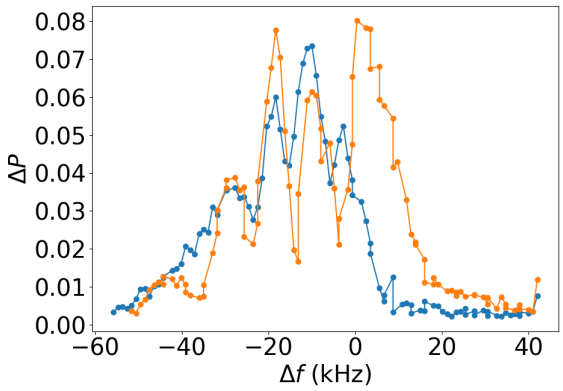

Figure 4.10. The population modulation (ΔP) of the interference signal vs a sweep across frequency. The orange curve is when the two excitation chambers are in-phase and the blue curve is when the two excitation chambers out-of-phase. Each point is the average of 2s from the lock in amplifier, whose time constant is 100 ms. The in-phase and out-of-phase phase shifter values were found using the rf only signal for the $\Delta m = 1$ transition peak, to either maximize or minimize the peak respectively.

of magnitude. We did not find a difference between no rf shielding or with rf shielding in the interference or rf only signal. The peaks in the interference signal did change somewhat by changing the phase of one input excitation chamber on the rf cavity in comparison with the other, but the overall height didn't change. One example can be seen in Fig. 4.10. The rf only signal changed in height depending how in-phase (bigger) or out-of-phase (smaller) the two excitation chambers were. We decided to investigate the phase difference of the two excitation chambers more closely as we were able to observe changes to the spectral interference signal.

We further tested what occurred when the relative phase difference of the two rf inputs changed by investigating what happened to our signals when the excitation chambers are completely in- or out-of-phase (or as close as we could realistically achieve). From COMSOL calculations, when the two excitation chambers are out-of-phase the TM mode in the science chamber is minimized, seen in Fig. 4.11 and Fig. 4.12. When the two excitation chambers are in-phase the TM mode is maximized, seen in Fig. 3.16 and Fig. 3.17. We determined how in-phase or out-of-phase the two excitation chambers were by looking at the rf only signal of

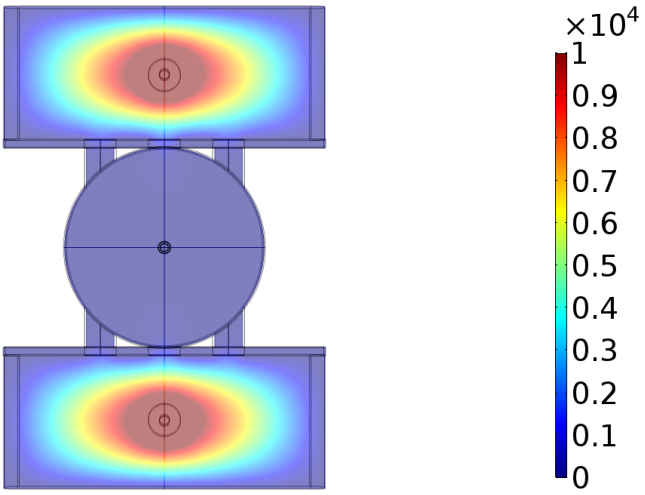

Figure 4.11. Color plot of e^{rf}_{norm} over the rf cavity when the two excitation chambers are out-of-phase. Units are (V/m).

the $\Delta m = 1$ transition peak height. To optimize the two excitation cavity's being in-phase, we tweaked the phase difference to have the $\Delta m = 1$ transition peak be as big as possible (usually done at small rf powers to avoid saturation effects). To optimize the two excitation cavity's being out-of-phase, we tweaked the phase to have the $\Delta m = 1$ transition peak be as small as could be made (usually done at normal rf powers to keep the signal above the noise). We weren't able to completely get them in or out-of-phase, so the $\Delta m = 1$ transition peak never completely went away while optimizing the out-of-phase phase difference. As a note, for the out-of-phase signal the $\Delta m = 0$ transition peak was reduced below the noise, while the in-phase signal was at its biggest. Interestingly, even at these extremes, the interference signal's height did not vary that much, seen in Fig. 4.10. From Comsol simulations, the h_z^{rf} on the atom hole of the rf cavity maintains a similar magnitude for the two excitation chambers being in- or out-of-phase, seen in Fig. 4.13. After all of our tests, we believe the interference signal we saw is most likely due to the h_z^{rf} near the input and exit atom holes, while the rf only signal is due to a small gradient of the transverse magnetic field.

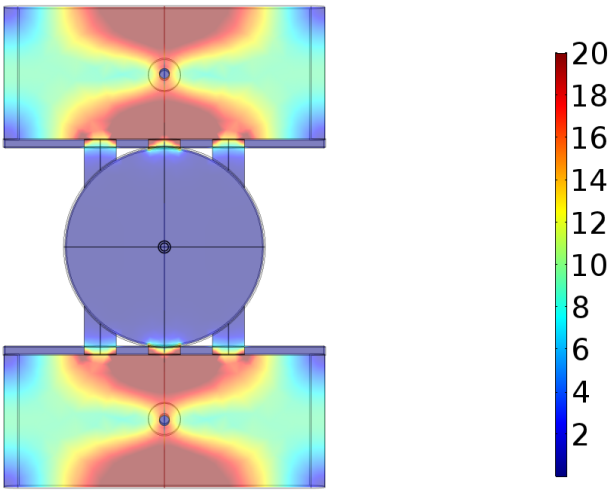

Figure 4.12. Color plot of h^{rf}_{norm} over the rf cavity when the two excitation chambers are out-of-phase. Units of the color bar are (A/m).

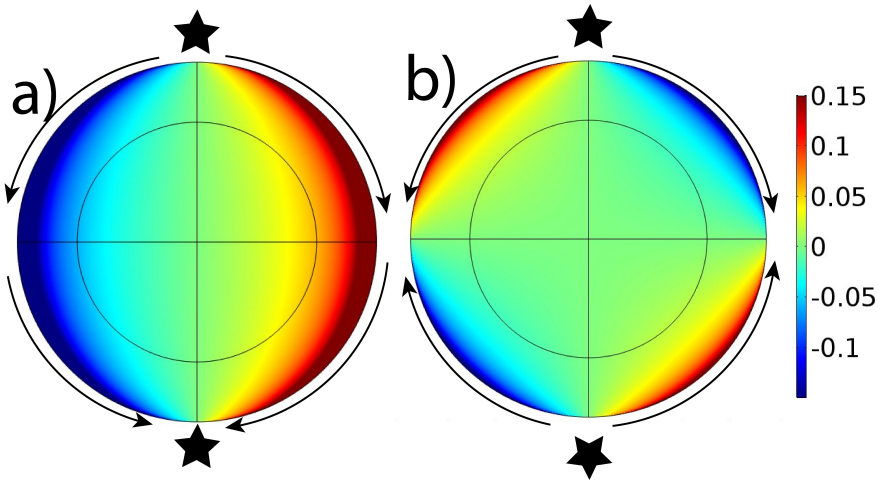

Figure 4.13. Color plot of h^{rf}_{z} over the cross section of the atom entry hole for the rf cavity. The inner black circle is the intended size and location of the atom beam. a) is when the two excitation chambers are out-of-phase and b) is when the two excitation chambers are in-phase. Units of the color bar are (A/m).

4.4.1 Details on Effects of the Magnetic Fields in Each Region

In this section I will discuss the details of getting the needed magnetic field for each region. Each region has different sensitivities to a non-ideal magnetic field. The detection region is the least affected by non-ideal magnetic fields. The large B_z field leaking into the region from the interaction region does not impact the experimental detection efficiency to a noticeable degree. The optical pumping region is mildly affected by magnetic fields that are not B_x. The large B_z field leaking into the region from the interaction region impacts the pumping efficiency to the correct ground Zeeman level. For example, with no large B_z field in the interaction region, we can achieve pumping efficiencies of greater than 95% into the wanted ground m level. With the large $B_z \sim 7G$ field in the interaction region turned on, the pumping efficiency dropped to 60%. With the two B_z correcting coils in the optical pumping region on and tuned to reduce B_z in the pumping region, seen in Fig. 3.9, we were able to increase the efficiency to 80%. We also had to keep the imposed B_x field small for the region. Increasing this field would improve the pumping efficiency, but it would also increase the B_x field that leaked into the interaction region. Thankfully, poor pumping efficiency mainly just lowers the overall signal, with minimal effects to the signal from atoms being in the wrong state. We decided to sacrifice the pumping efficiency for less transverse magnetic fields in the interaction region. The interaction region is the region most sensitive to the magnitude, orientation, and uniformity of $\mathbf{B}$. The most sensitive part of the interaction region is along the 1.25 cm long rf cavity. Misalignment of $\mathbf{B}$ with the axis of the rf cavity leads to magnetic dipole contributions to the signal, that we need to reduce in order to see the E_{PNC} signal. We also had to ensure that B_z stayed constant over the Raman beam and rf cavity to keep their resonant frequencies overlapped. When tuning all of the magnetic field coils, we have to keep the desired magnetic field for each region in mind.

For setting the correct current for the magnetic field coils in the various regions, all of the coils were tweaked iteratively to get the final desired fields in each region while observing the rf only signal. We tried observing the interference signal as well for this step, but found the signal's shape was too confusing and we were unable to lower the B_x and B_y field as far. The shape we ended up looking for on the detection system for the $\Delta m = 0$ transition

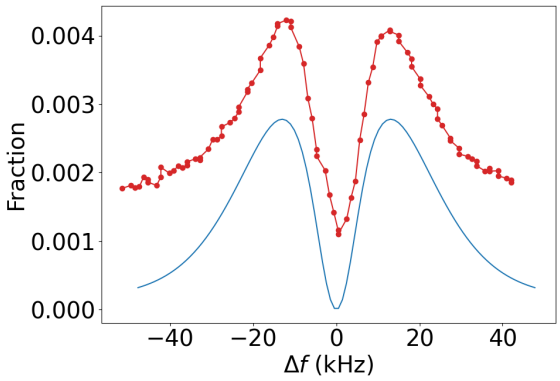

Figure 4.14. The red curve is the experimental data of the $\Delta m = 0$ transition peak and the blue curve is the theoretical simulation with averaging over velocity and atom beam width with a linear gradient of B_x. B_x varied linearly from -30 mG to +30 mG. Fraction is the change in population due to the rf field where fraction = 0 corresponds to zero atoms in the excited, $F = 4$ state.

rf only peak was a small and narrow duel peak structure, with the minimum between the two peaks near zero, seen in Fig. 4.9. The duel peak structure most likely came from the gradient B_x and B_y fields we were unable to reduce. For a gradient of B_x or B_y that passed through zero at the center of the cavity, and the integration of the transverse magnetic field was exactly equal on each half of the rf cavity, the atom beam signal would sum to zero at the resonant frequency. At non-resonant frequencies, the summing to zero from equal halves is no longer as clean on the Bloch sphere and will result in a non-zero signal after the rf cavity. A comparison of theoretical calculations for a linear gradient of B_x or B_y in our system to our experimental results is seen in Fig. 4.14. This leads us to believe for the future progress, improving the B_x and B_y gradient in the interaction region will be important.

4.5 Next Steps to Measure the Anapole Moment

After analyzing the current signal we can achieve and verifying our noise in the system, we believe the most straightforward way to achieve our measurement is to design and create a new rf cavity that reduces the h_z^{rf} on the atom entry/exit holes of the rf cavity. We decided the best way to reduce the h_z^{rf} on the atom entry/exit holes was to introduce more

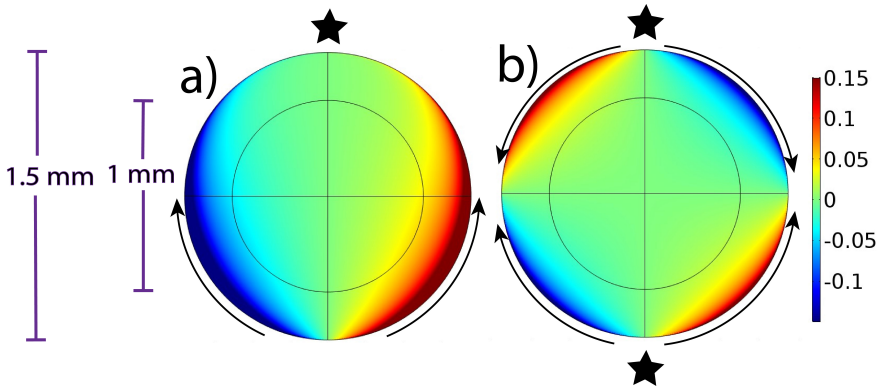

Figure 4.15. Color plot of h_z^{rf} over the cross section of the atom entry hole for the rf cavity. The inner black circle is the intended size and location of the atom beam. a) is when one excitation chamber is excited and b) is when the two excitation chambers are both excited in-phase. A star denotes the location of the excited chamber. Units of the color bar are (A/m).

symmetry into the system after testing different configurations in COMSOL. We found that for the cylindrical rf cavity we used, when both excitation chambers were powered at the same phase the h_z^{rf} became slightly canceled near the center compared to only one chamber powered, seen in Fig. 4.15. We decided to add additional excitation chambers to see if we could reduce it even further. Due to spatial considerations, we made the excitation chambers one big cylinder with four SMA cable inputs to evenly input the rf power, seen in Fig. 4.16. When each SMA cable input is excited with 1 W, the h_z^{rf} on the atom entry/exit hole is reduced by over 2 orders of magnitude (where e_z^{rf} is four times larger) than the rf cavity design used for the current experiment (with two SMA cable inputs each excited with 1W of rf power). The h_z^{rf} on the atom entry hole can be seen in Fig. 4.17 for the new cavity design. Additionally, what appears on the atom beam entry/exit hole seems to occur near the limitations in COMSOL's capabilities, so it could be potentially even smaller. We therefore believe the new design will reduce h_z^{rf} on the atom entry/exit holes.

If this 4 input rf cavity design does not sufficiently reduce the h_z^{rf} on the atom beam entry/exit holes, another option would be to use a pulsed experiment to be able to just 'ignore' the time the atom spends in the atom hole. We have not implemented this idea or done much with it due to the current spread of atomic velocities in the system. We would

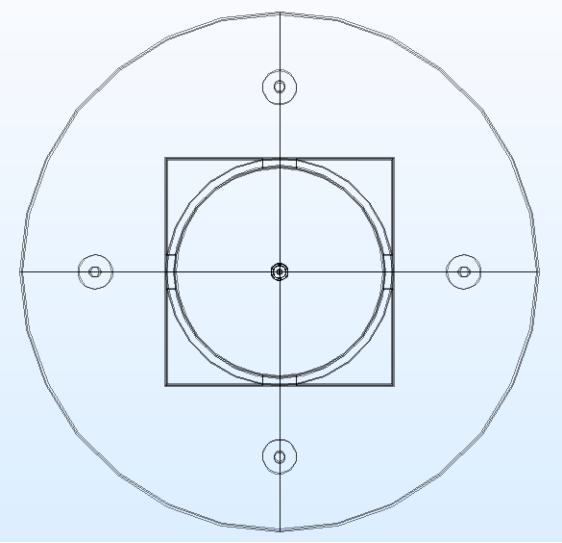

Figure 4.16. Proposed 4 input cavity design. The central circular outline is the science chamber which is the same as the cylindrical cavity that has been used in this thesis. Surrounding it are four equally-spaced rf inputs in a second bigger cylindrical cavity that will act like the excitation chambers of the cylindrical cavity being used. The height of this excitation chamber is about 1/3 the height of the central cylinder. Power is coupled from the outer excitation chamber into the central cavity via four coupling channels that are rectangular in shape.

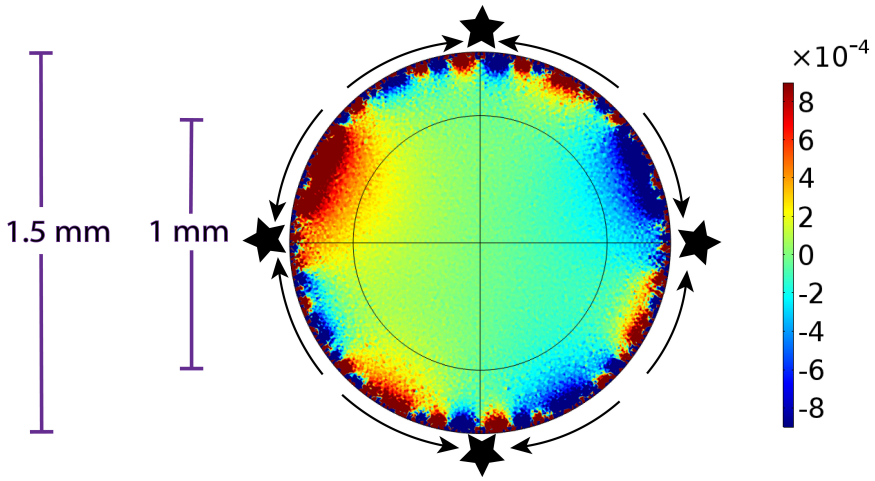

Figure 4.17. Color plot of h_z^{rf} over the cross section of the atom beam entry/exit hole for the newly designed 4 input rf cavity. The inner black circle is the intended size and location of the atom beam. The stars denote the location of the SMA inputs. The maximum h_z^{rf} is over 2 orders of magnitude smaller while $\mathrm{e}_z^{\mathrm{rf}}$ is over 4 times bigger than the current rf cavity. There is doubt in the shape of the h_z^{rf} as this is close to the limits of COMSOL calculations.

need to find a way to be able to select just a portion of the atoms at a certain velocity. We could then use pulses of rf power to only have rf power on when the atoms interact with the main body of the rf cavity and not the atom entry/exit holes on the rf cavity. This would allow us to observe E_{PNC} as V_m due to h_z^{rf} would be reduced.

5. CONCLUSION

This thesis includes my contributions to achieve more precise results of the PNC effect in cesium atoms. In this chapter I discuss what I have accomplished towards this goal and what still needs to be done.

5.1 My Contributions

The first contributions I made in the lab were towards measuring various reduced electric dipole matrix elements in cesium. These measurements, which are described in Appendix A, help improve the experimental value of the scalar and vector polarizabilty for the $6s - 7s$ transition in cesium. Improved values help give theorists bench marks to compare their theories against. The second part is vital, as we rely on theorists to calculate the necessary factors that relate our measured experimental amplitudes to the anapole moment or the weak charge of cesium, which cannot be directly experimentally measured. More information on this may be seen in the Appendix A.

I also significantly advanced the system and technique for the measurement of the anapole moment in cesium. I revamped the Raman laser setup from using injection locking to a PLL circuit to maintain the 9.2 GHz frequency splitting between two lasers. We changed the design of the rf field from using a PPTL to using a rf cavity to confine the rf fields to a known region. Finally, I determined that the current limitation in our system to measuring the anapole moment is the h_z^{rf} on the atom entry and exit holes in the rf cavity.

5.2 Future

The ultimate goal of the anapole moment experiment is to measure the moment to a precision of 3%. There is a need for further tests of the new proposed 4 port rf cavity, particularly controlling and characterizing the rf mode in the rf cavity. There is still more work to be done on characterizing the shape of the static magnetic field in the vacuum chamber, since new coils will be used to give slight tweaks to B_x and B_y. The new coils should introduce smaller gradients in the transverse magnetic field than the pairs I used

in this document. Lastly more tests will need to be done experimentally to identify and verify areas of concern for the measurement that we could not fully explore due to the signal obtained being 3 to 4 orders of magnitude bigger than the expected PNC signal's amplitude.

REFERENCES

[1] S. Weinberg, "The making of the standard model," *The European Physical Journal C - Particles and Fields*, vol. 34, no. 1, pp. 5–13, May 2004, ISSN: 1434-6052. DOI: 10.1140/epjc/s2004-01761-1. [Online]. Available: https://doi.org/10.1140/epjc/s2004-01761-1.

[2] J. Ginges and V. Flambaum, "Violations of fundamental symmetries in atoms and tests of unification theories of elementary particles," *Physics Reports*, vol. 397, no. 2, pp. 63–154, 2004, ISSN: 0370-1573. DOI: https://doi.org/10.1016/j.physrep.2004.03.005. [Online]. Available: http://www.sciencedirect.com/science/article/pii/S0370157304001322.

[3] M. S. Safronova, D. Budker, D. DeMille, D. F. J. Kimball, A. Derevianko, and C. W. Clark, "Search for new physics with atoms and molecules," *Rev. Mod. Phys.*, vol. 90, p. 025 008, 2 Jun. 2018. DOI: 10.1103/RevModPhys.90.025008. [Online]. Available: https://link.aps.org/doi/10.1103/RevModPhys.90.025008.

[4] H. Davoudiasl and I. M. Lewis, "Dark matter from hidden forces," *Phys. Rev. D*, vol. 89, p. 055 026, 5 Mar. 2014. DOI: 10.1103/PhysRevD.89.055026. [Online]. Available: https://link.aps.org/doi/10.1103/PhysRevD.89.055026.

[5] J. Erler and P. Langacker, "Indications for an extra neutral gauge boson in electroweak precision data," *Physical Review Letters*, vol. 84, no. 2, p. 212, 2000. [Online]. Available: https://link.aps.org/doi/10.1103/PhysRevLett.84.212.

[6] R. Diener, S. Godfrey, and I. Turan, "Constraining extra neutral gauge bosons with atomic parity violation measurements," *Phys. Rev. D*, vol. 86, p. 115 017, 11 Dec. 2012. DOI: 10.1103/PhysRevD.86.115017. [Online]. Available: https://link.aps.org/doi/10.1103/PhysRevD.86.115017.

[7] C. Bhm and P. Fayet, "Scalar dark matter candidates," *Nuclear Physics B*, vol. 683, no. 1, pp. 219–263, 2004, ISSN: 0550-3213. DOI: https://doi.org/10.1016/j.nuclphysb.2004.01.015. [Online]. Available: http://www.sciencedirect.com/science/article/pii/S0550321304000306.

[8] M. Cadeddu, N. Cargioli, F. Dordei, C. Giunti, and E. Picciau, "Muon and electron $g-2$ and proton and cesium weak charges implications on dark Z_d models," *Physical Review D*, vol. 104, Jul. 2021. DOI: 10.1103/PhysRevD.104.L011701.

[9] B. Aubert and C. Rubbia, "Twenty years neutral currents - ten years W and Z: Cern colloquium, April 29, 1993," *Physics Reports*, vol. 239, no. 4, pp. 215–284, 1994, ISSN: 0370-1573. DOI: https://doi.org/10.1016/0370-1573(94)90077-9. [Online]. Available: http://www.sciencedirect.com/science/article/pii/0370157394900779.

[10] B. Roberts, V. Dzuba, and V. Flambaum, "Parity and time-reversal violation in atomic systems," *Annual Review of Nuclear and Particle Science*, vol. 65, no. 1, pp. 63–86, 2015. DOI: 10.1146/annurev-nucl-102014-022331. eprint: https://doi.org/10.1146/annurev-nucl-102014-022331. [Online]. Available: https://doi.org/10.1146/annurev-nucl-102014-022331.

[11] A. Rousset, "The discovery of weak neutral currents," *Nuclear Physics B - Proceedings Supplements*, vol. 36, pp. 339–362, 1994, ISSN: 0920-5632. DOI: https://doi.org/10.1016/0920-5632(94)90785-4. [Online]. Available: http://www.sciencedirect.com/science/article/pii/0920563294907854.

[12] D. J. Griffiths, *Introduction to elementary particles*. Weinheim, Germany: Wiley-VCH Verlag GmbH & Co. KGaA, 2004, ISBN: 9783527618460.

[13] F. Hasert, H. Faissner, W. Krenz, *et al.*, "Search for elastic muon-neutrino electron scattering," *Physics Letters B*, vol. 46, no. 1, pp. 121–124, 1973, ISSN: 0370-2693. DOI: https://doi.org/10.1016/0370-2693(73)90494-2. [Online]. Available: http://www.sciencedirect.com/science/article/pii/0370269373904942.

[14] W. C. Haxton and C. E. Wieman, "Atomic parity nonconservation and nuclear anapole moments," *Annual Review of Nuclear and Particle Science*, vol. 51, no. 1, pp. 261–293, 2001. DOI: 10.1146/annurev.nucl.51.101701.132458. eprint: https://doi.org/10.1146/annurev.nucl.51.101701.132458. [Online]. Available: https://doi.org/10.1146/annurev.nucl.51.101701.132458.

[15] E. M. Henley, "Parity and time-reversal invariance in nuclear physics," *Annual Review of Nuclear Science*, vol. 19, no. 1, pp. 367–432, 1969. DOI: 10.1146/annurev.ns.19.120169.002055. eprint: https://doi.org/10.1146/annurev.ns.19.120169.002055. [Online]. Available: https://doi.org/10.1146/annurev.ns.19.120169.002055.

[16] T. D. Lee and C. N. Yang, "Question of parity conservation in weak interactions," *Phys. Rev.*, vol. 104, pp. 254–258, 1 Oct. 1956. DOI: 10.1103/PhysRev.104.254. [Online]. Available: https://link.aps.org/doi/10.1103/PhysRev.104.254.

[17] C. S. Wu, E. Ambler, R. W. Hayward, D. D. Hoppes, and R. P. Hudson, "Experimental test of parity conservation in beta decay," *Phys. Rev.*, vol. 105, pp. 1413–1415, 4 Feb. 1957. DOI: 10.1103/PhysRev.105.1413. [Online]. Available: https://link.aps.org/doi/10.1103/PhysRev.105.1413.

[18] T. P. Emmons and E. N. Fortson, "Parity nonconservation in atoms," in *Progress in Atomic Spectroscopy: Part D*, H. J. Beyer and H. Kleinpoppen, Eds. Boston, MA: Springer US, 1987, pp. 237–269.

[19] M.-A. Bouchiat and C. Bouchiat, "Parity violation in atoms," *Reports on Progress in Physics*, vol. 60, no. 11, pp. 1351–1396, Nov. 1997. DOI: 10.1088/0034-4885/60/11/004.

[20] C. Bouchiat and C. Piketty, "Parity violation in atomic cesium and alternatives to the standard model of electroweak interactions," *Physics Letters B*, vol. 128, no. 1, pp. 73–78, 1983, ISSN: 0370-2693. DOI: https://doi.org/10.1016/0370-2693(83)90076-X. [Online]. Available: http://www.sciencedirect.com/science/article/pii/037026938390076X.

[21] T. T. Hoang Bao and A. Derevianko, "Implications of W-boson mass anomaly for atomic parity violation," *Atoms*, vol. 10, no. 4, p. 149, 2022. [Online]. Available: https://www.proquest.com/scholarly-journals/implications-w-boson-mass-anomaly-atomic-parity/docview/2756660225/se-2.

[22] Y. B. Zeldovich, "Parity nonconservation in the 1st order in the weak-interaction constant in electron scattering and other effects," *J. Exptl. Theoret. Phys. (U.S.S.R.)*., vol. 36, 1959.

[23] Bouchiat, M. A. and Bouchiat, C., "I. parity violation induced by weak neutral currents in atomic physics," *J. Phys. France*, vol. 35, no. 12, pp. 899–927, 1974. DOI: 10.1051/jphys:019740035012089900. [Online]. Available: https://doi.org/10.1051/jphys:019740035012089900.

[24] C. S. Wood, S. C. Bennett, D. Cho, *et al.*, "Measurement of parity nonconservation and an anapole moment in cesium," *Science*, vol. 275, no. 5307, pp. 1759–1763, 1997, ISSN: 0036-8075. DOI: 10.1126/science.275.5307.1759. eprint: https://science.sciencemag.org/content/275/5307/1759.full.pdf. [Online]. Available: https://science.sciencemag.org/content/275/5307/1759.

[25] D. Antypas, A. Fabricant, J. Stalnaker, K. Tsigutkin, and D. Budker, "Isotopic variation of parity violation in atomic ytterbium," *Nature Physics*, vol. 15, Feb. 2019. DOI: 10.1038/s41567-018-0312-8.

[26] N. H. Edwards, S. J. Phipp, P. E. G. Baird, and S. Nakayama, "Precise measurement of parity nonconserving optical rotation in atomic thallium," *Phys. Rev. Lett.*, vol. 74, pp. 2654–2657, 14 Apr. 1995. DOI: 10.1103/PhysRevLett.74.2654. [Online]. Available: https://link.aps.org/doi/10.1103/PhysRevLett.74.2654.

[27] D. M. Meekhof, P. A. Vetter, P. K. Majumder, S. K. Lamoreaux, and E. N. Fortson, "Optical-rotation technique used for a high-precision measurement of parity nonconservation in atomic lead," *Phys. Rev. A*, vol. 52, pp. 1895–1908, 3 Sep. 1995. DOI: 10.1103/PhysRevA.52.1895. [Online]. Available: https://link.aps.org/doi/10.1103/PhysRevA.52.1895.

[28] M. J. D. Macpherson, K. P. Zetie, R. B. Warrington, D. N. Stacey, and J. P. Hoare, "Precise measurement of parity nonconserving optical rotation at 876 nm in atomic bismuth," *Phys. Rev. Lett.*, vol. 67, pp. 2784–2787, 20 Nov. 1991. DOI: 10.1103/PhysRevLett.67.2784. [Online]. Available: https://link.aps.org/doi/10.1103/PhysRevLett.67.2784.

[29] A. Kramida, Y. Ralchenko, J. Reader, and NIST ASD Team, "Nist atomic spectra database (version 5.0); National Institute of Standards and Technology, Gaithersburg, MD, 2012," *NIST Atomic Spectra Database (version 5.6.1)*, 2019. [Online]. Available: https://physics.nist.gov/asd.

[30] W. Williams, M. Herd, and W. Hawkins, "Spectroscopic study of the $7P_{1/2}$ and $7P_{3/2}$ states in cesium-133," *Laser Physics Letters*, vol. 15, no. 9, p. 095 702, 2018. DOI: 10.1088/1612-202X/aac97e. [Online]. Available: https://dx.doi.org/10.1088/1612-202X/aac97e.

[31] T. Udem, J. Reichert, R. Holzwarth, and T. W. Hänsch, "Absolute optical frequency measurement of the cesium D_1 line with a mode-locked laser," *Phys. Rev. Lett.*, vol. 82, pp. 3568–3571, 18 May 1999. DOI: 10.1103/PhysRevLett.82.3568. [Online]. Available: https://link.aps.org/doi/10.1103/PhysRevLett.82.3568.

[32] D. Das and V. Natarajan, "Precise measurement of hyperfine structure in the $6P_{1/2}$ state of ^{133}Cs," *Journal of Physics B: Atomic, Molecular and Optical Physics*, vol. 39, no. 8, p. 2013, 2006. DOI: 10.1088/0953-4075/39/8/018. [Online]. Available: https://dx.doi.org/10.1088/0953-4075/39/8/018.

[33] R. J. Rafac and C. E. Tanner, "Measurement of the ^{133}Cs $6p^2P_{1/2}$ state hyperfine structure," *Phys. Rev. A*, vol. 56, pp. 1027–1030, 1 Jul. 1997. DOI: 10.1103/PhysRevA.56.1027. [Online]. Available: https://link.aps.org/doi/10.1103/PhysRevA.56.1027.

[34] V. Gerginov, K. Calkins, C. E. Tanner, *et al.*, "Optical frequency measurements of $6s\,^2S_{12} - 6p\,^2P_{12}$ (D_1) transitions in ^{133}Cs and their impact on the fine-structure constant," *Phys. Rev. A*, vol. 73, p. 032 504, 3 Mar. 2006. DOI: 10.1103/PhysRevA.73.032504. [Online]. Available: https://link.aps.org/doi/10.1103/PhysRevA.73.032504.

[35] S. L. Gilbert, R. N. Watts, and C. E. Wieman, "Hyperfine-structure measurement of the $7S$ state of cesium," *Phys. Rev. A*, vol. 27, pp. 581–582, 1 Jan. 1983. DOI: 10.1103/PhysRevA.27.581. [Online]. Available: https://link.aps.org/doi/10.1103/PhysRevA.27.581.

[36] G. Yang, J. Wang, B. Yang, and J. Wang, "Determination of the hyperfine coupling constant of the cesium $7S_{1/2}$ state," *Laser Physics Letters*, vol. 13, no. 8, p. 085 702, 2016. [Online]. Available: http://stacks.iop.org/1612-202X/13/i=8/a=085702.

[37] Y. D. G. Toh, "Progress towards a new parity non-conservation measurement in cesium-133," Ph.D. dissertation, Purdue University, Aug. 2019. DOI: 10.25394/PGS.8297531.v1.

[38] C. S. Wood, S. C. Bennett, J. L. Roberts, D. Cho, and C. E. Wieman, "Precision measurement of parity nonconservation in cesium," *Canadian Journal of Physics*, vol. 77, no. 1, pp. 7–75, 1999. DOI: 10.1139/p99-002. eprint: https://doi.org/10.1139/p99-002. [Online]. Available: https://doi.org/10.1139/p99-002.

[39] V. Flambaum, I. Khriplovich, and O. Sushkov, "Nuclear anapole moments," *Physics Letters B*, vol. 146, no. 6, pp. 367–369, 1984, ISSN: 0370-2693. DOI: https://doi.org/10.1016/0370-2693(84)90140-0. [Online]. Available: http://www.sciencedirect.com/science/article/pii/0370269384901400.

[40] C. Bouchiat and C. A. Piketty, "Nuclear spin dependent atomic parity violation, nuclear anapole moments and the hadronic axial neutral current," *Zeitschrift für Physik C Particles and Fields*, vol. 49, pp. 91–107, 1991. DOI: 10.1007/BF01570800. [Online]. Available: https://doi.org/10.1007/BF01570800.

[41] V. Dmitriev, I. Khriplovich, and V. Telitsin, "Nuclear anapole moments in single-particle approximation," *Nuclear Physics A*, vol. 577, no. 3, pp. 691–708, 1994, ISSN: 0375-9474. DOI: https://doi.org/10.1016/0375-9474(94)90940-7. [Online]. Available: http://www.sciencedirect.com/science/article/pii/0375947494909407.

[42] V. V. Flambaum and D. W. Murray, "Anapole moment and nucleon weak interactions," *Phys. Rev. C*, vol. 56, pp. 1641–1644, 3 Sep. 1997. DOI: 10.1103/PhysRevC.56.1641. [Online]. Available: https://link.aps.org/doi/10.1103/PhysRevC.56.1641.

[43] M. Gunawardena and D. S. Elliott, "Weak signal detection using coherent control," *Phys. Rev. A*, vol. 76, p. 033 412, 3 Sep. 2007. DOI: 10.1103/PhysRevA.76.033412. [Online]. Available: https://link.aps.org/doi/10.1103/PhysRevA.76.033412.

[44] Y.-Y. Yin, C. Chen, D. S. Elliott, and A. V. Smith, "Asymmetric photoelectron angular distributions from interfering photoionization processes," *Phys. Rev. Lett.*, vol. 69, pp. 2353–2356, 16 Oct. 1992. DOI: 10.1103/PhysRevLett.69.2353. [Online]. Available: https://link.aps.org/doi/10.1103/PhysRevLett.69.2353.

[45] C. Chen, Y.-Y. Yin, and D. S. Elliott, "Interference between optical transitions," *Phys. Rev. Lett.*, vol. 64, pp. 507–510, 5 Jan. 1990. DOI: 10.1103/PhysRevLett.64.507. [Online]. Available: https://link.aps.org/doi/10.1103/PhysRevLett.64.507.

[46] C. Chen and D. S. Elliott, "Measurements of optical phase variations using interfering multiphoton ionization processes," *Phys. Rev. Lett.*, vol. 65, pp. 1737–1740, 14 Oct. 1990. DOI: 10.1103/PhysRevLett.65.1737. [Online]. Available: https://link.aps.org/doi/10.1103/PhysRevLett.65.1737.

[47] D. Antypas and D. Elliott, "Measurement of weak optical transition moments through two-pathway coherent control," *Canadian Journal of Chemistry*, vol. 92, no. 2, pp. 144–156, 2014. DOI: 10.1139/cjc-2013-0318. eprint: https://doi.org/10.1139/cjc-2013-0318. [Online]. Available: https://doi.org/10.1139/cjc-2013-0318.

[48] E. Gomez, S. Aubin, G. D. Sprouse, L. A. Orozco, and D. P. DeMille, "Measurement method for the nuclear anapole moment of laser-trapped alkali-metal atoms," *Phys. Rev. A*, vol. 75, p. 033 418, 3 Mar. 2007. DOI: 10.1103/PhysRevA.75.033418. [Online]. Available: https://link.aps.org/doi/10.1103/PhysRevA.75.033418.

[49] L. A. Orozco, "The francium trapping facility at triumf," *Nuclear Physics News*, vol. 23, no. 4, pp. 17–20, 2013. DOI: 10.1080/10619127.2013.821918. eprint: https://doi.org/10.1080/10619127.2013.821918. [Online]. Available: https://doi.org/10.1080/10619127.2013.821918.

[50] E. Gomez, S. Aubin, R. Collister, *et al.*, "The FrPNC experiment, weak interaction studies in francium at TRIUMF," *Journal of Physics: Conference Series*, vol. 387, p. 012 004, Sep. 2012. DOI: 10.1088/1742-6596/387/1/012004. [Online]. Available: https://doi.org/10.1088/1742-6596/387/1/012004.

[51] D. Sheng, L. A. Orozco, and E. Gomez, "Preliminary studies for anapole moment measurements in rubidium and francium," *Journal of Physics B: Atomic, Molecular and Optical Physics*, vol. 43, no. 7, p. 074 004, Mar. 2010. DOI: 10.1088/0953-4075/43/7/074004. [Online]. Available: https://doi.org/10.1088/0953-4075/43/7/074004.

[52] G. Gwinner and L. Orozco, "Studies of the weak interaction in atomic systems: Towards measurements of atomic parity non-conservation in francium," *Quantum Science and Technology*, vol. 7, no. 2, p. 024 001, 2022.

[53] D. Antypas, A. Fabricant, J. Stalnaker, K. Tsigutkin, V. Flambaum, and D. Budker, "Isotopic variation of parity violation in atomic ytterbium," *Nature Physics*, vol. 15, no. 2, p. 120, 2019.

[54] E. Altunta , J. Ammon, S. B. Cahn, and D. DeMille, "Demonstration of a sensitive method to measure nuclear-spin-dependent parity violation," *Phys. Rev. Lett.*, vol. 120, p. 142 501, 14 Apr. 2018. DOI: 10.1103/PhysRevLett.120.142501. [Online]. Available: https://link.aps.org/doi/10.1103/PhysRevLett.120.142501.

[55] E. Altuntas, J. Ammon, S. B. Cahn, and D. DeMille, "Measuring nuclear-spin-dependent parity violation with molecules: Experimental methods and analysis of systematic errors," *Phys. Rev. A*, vol. 97, p. 042 101, 4 Apr. 2018. DOI: 10.1103/PhysRevA.97.042101. [Online]. Available: https://link.aps.org/doi/10.1103/PhysRevA.97.042101.

[56] D. DeMille, S. B. Cahn, D. Murphree, D. A. Rahmlow, and M. G. Kozlov, "Using molecules to measure nuclear spin-dependent parity violation," *Phys. Rev. Lett.*, vol. 100, p. 023 003, 2 Jan. 2008. DOI: 10.1103/PhysRevLett.100.023003. [Online]. Available: https://link.aps.org/doi/10.1103/PhysRevLett.100.023003.

[57] V. A. Dzuba, J. C. Berengut, V. V. Flambaum, and B. Roberts, "Revisiting parity nonconservation in cesium," *Phys. Rev. Lett.*, vol. 109, p. 203 003, 20 Nov. 2012. DOI: 10.1103/PhysRevLett.109.203003. [Online]. Available: https://link.aps.org/doi/10.1103/PhysRevLett.109.203003.

[58] S. G. Porsev, K. Beloy, and A. Derevianko, "Precision determination of weak charge of ^{133}Cs from atomic parity violation," *Phys. Rev. D*, vol. 82, p. 036 008, 3 Aug. 2010. DOI: 10.1103/PhysRevD.82.036008. [Online]. Available: https://link.aps.org/doi/10.1103/PhysRevD.82.036008.

[59] S. G. Porsev, K. Beloy, and A. Derevianko, "Precision determination of electroweak coupling from atomic parity violation and implications for particle physics," *Phys. Rev. Lett.*, vol. 102, p. 181 601, 18 May 2009. DOI: 10.1103/PhysRevLett.102.181601. [Online]. Available: https://link.aps.org/doi/10.1103/PhysRevLett.102.181601.

[60] B. M. Roberts and J. S. M. Ginges, "Comment on "new physics constraints from atomic parity violation in ^{133}Cs"," *Phys. Rev. D*, vol. 105, p. 018 301, 1 Jan. 2022. DOI: 10.1103/PhysRevD.105.018301. [Online]. Available: https://link.aps.org/doi/10.1103/PhysRevD.105.018301.

[61] B. K. Sahoo, B. P. Das, and H. Spiesberger, "New physics constraints from atomic parity violation in ^{133}Cs," *Phys. Rev. D*, vol. 103, p. L111303, 11 Jun. 2021. DOI: 10.1103/PhysRevD.103.L111303. [Online]. Available: https://link.aps.org/doi/10.1103/PhysRevD.103.L111303.

[62] H. B. Tran Tan, D. Xiao, and A. Derevianko, "Parity-mixed coupled-cluster formalism for computing parity-violating amplitudes," *Phys. Rev. A*, vol. 105, p. 022 803, 2 Feb. 2022. DOI: 10.1103/PhysRevA.105.022803. [Online]. Available: https://link.aps.org/doi/10.1103/PhysRevA.105.022803.

[63] B. K. Sahoo and B. P. Das, *Constraints on new physics from an improved calculation of parity violation in* ^{133}Cs, 2020. arXiv: 2008.08941 [hep-ph].

[64] B. K. Sahoo, B. P. Das, and H. Spiesberger, "Reply to "comment on 'new physics constraints from atomic parity violation in ^{133}Cs"'," *Phys. Rev. D*, vol. 105, p. 018 302, 1 Jan. 2022. DOI: 10.1103/PhysRevD.105.018302. [Online]. Available: https://link.aps.org/doi/10.1103/PhysRevD.105.018302.

[65] B. M. Roberts, P. G. Ranclaud, and J. S. M. Ginges, "Bohr-weisskopf effect: From hydrogenlike-ion experiments to heavy-atom calculations of the hyperfine structure," *Phys. Rev. A*, vol. 105, p. 052 802, 5 May 2022. DOI: 10.1103/PhysRevA.105.052802. [Online]. Available: https://link.aps.org/doi/10.1103/PhysRevA.105.052802.

[66] B. M. Roberts, C. J. Fairhall, and J. S. M. Ginges, "Electric-dipole transition amplitudes for atoms and ions with one valence electron," *Phys. Rev. A*, vol. 107, p. 052 812, 5 May 2023. DOI: 10.1103/PhysRevA.107.052812. [Online]. Available: https://link.aps.org/doi/10.1103/PhysRevA.107.052812.

[67] C. J. Fairhall, B. M. Roberts, and J. S. M. Ginges, "QED Radiative corrections to electric dipole amplitudes in heavy atoms," *Phys. Rev. A*, vol. 107, p. 022 813, 2 Feb. 2023. DOI: 10.1103/PhysRevA.107.022813. [Online]. Available: https://link.aps.org/doi/10.1103/PhysRevA.107.022813.

[68] B. M. Roberts and J. S. M. Ginges, "Hyperfine anomaly in heavy atoms and its role in precision atomic searches for new physics," *Phys. Rev. A*, vol. 104, p. 022 823, 2 Aug. 2021. DOI: 10.1103/PhysRevA.104.022823. [Online]. Available: https://link.aps.org/doi/10.1103/PhysRevA.104.022823.

[69] H. B. Tran Tan and A. Derevianko, *Precision theoretical determination of electric-dipole matrix elements in atomic cesium*, Apr. 2023. DOI: 10.1103/PhysRevA.107.042809. [Online]. Available: https://link.aps.org/doi/10.1103/PhysRevA.107.042809.

[70] D. Antypas and D. S. Elliott, "Measurement of a weak transition moment using two-pathway coherent control," *Phys. Rev. A*, vol. 87, p. 042 505, 4 Apr. 2013. DOI: 10.1103/PhysRevA.87.042505. [Online]. Available: https://link.aps.org/doi/10.1103/PhysRevA.87.042505.

[71] D. Antypas, "Measurement of a weak transition moment using coherent control," Ph.D. dissertation, Purdue University, 2013.

[72] S. L. Gilbert and C. E. Wieman, "Atomic-beam measurement of parity nonconservation in cesium," *Phys. Rev. A*, vol. 34, pp. 792–803, 2 Aug. 1986. DOI: 10.1103/PhysRevA.34.792. [Online]. Available: https://link.aps.org/doi/10.1103/PhysRevA.34.792.

[73] D. A. Steck, *Cesium D line data*, 2019. [Online]. Available: http://steck.us/alkalidata.

[74] J. D. Jackson, *Classical Electrodynamics.* eng. New York: Wiley, 1962.

[75] A. Derevianko, "Hyperfine-induced quadrupole moments of alkali-metal-atom ground states and their implications for atomic clocks," *Physical Review A*, vol. 93, no. 1, p. 012 503, 2016.

[76] R. Zare, *Angular Momentum, Understanding Spatial Aspects in Chemistry and Physics.* Wiley, 1988.

[77] M. Bouchiat and C. Bouchiat, "Parity violation induced by weak neutral currents in atomic physics. part ii," *Journal de Physique*, vol. 36, no. 6, pp. 493–509, 1975.

[78] S. L. Gilbert, R. N. Watts, and C. E. Wieman, "Measurement of the $6S \rightarrow 7S$ M1 transition in cesium with the use of crossed electric and magnetic fields," *Physical Review A*, vol. 29, no. 1, p. 137, 1984.

[79] N. Ramsey, *Molecular Beams* (International series of monographs on physics). OUP Oxford, 1956, ISBN: 9780198520214. [Online]. Available: https://books.google.com/books?id=T_7Hg08X7CMC.

[80] J. Choi, "Toward measurement of Nuclear Spin-Dependent(NSD) Parity Non-Conserving (PNC) interaction in ^{133}Cs hyperfine ground states via two-pathway coherent control," Ph.D. dissertation, Purdue University, Aug. 2019. DOI: 10.25394/PGS.8319686.v1.

[81] M. J. Snadden, R. B. M. Clarke, and E. Riis, "Injection-locking technique for heterodyne optical phase locking of a diode laser," *Opt. Lett.*, vol. 22, no. 12, pp. 892–894, Jun. 1997. DOI: 10.1364/OL.22.000892. [Online]. Available: http://ol.osa.org/abstract.cfm?URI=ol-22-12-892.

[82] J. Ringot, Y. Lecoq, J. Garreau, and P. Szriftgiser, "Generation of phase-coherent laser beams for raman spectroscopy and cooling by direct current modulation of a diode laser," *The European Physical Journal D - Atomic, Molecular, Optical and Plasma Physics*, vol. 7, no. 3, pp. 285–288, Oct. 1999, ISSN: 1434-6079. DOI: 10.1007/s100530050571. [Online]. Available: https://doi.org/10.1007/s100530050571.

[83] R. Kowalski, S. Root, S. D. Gensemer, and P. L. Gould, "A frequency-modulated injection-locked diode laser for two-frequency generation," *Review of Scientific Instruments*, vol. 72, no. 6, pp. 2532–2534, 2001. DOI: 10.1063/1.1373670. eprint: https://doi.org/10.1063/1.1373670. [Online]. Available: https://doi.org/10.1063/1.1373670.

[84] T. Wang, S.-J. Park, J. Shin, P. Jayne, L. G. Ramo, and T. Michalka, "2018 *IEEE* symposium on electromagnetic compatibility, signal integrity and power integrity (*EMC*, *SI* & *PI*)," in *Radiation Mechanisms and Mitigation Methods in Multi-GHz RF Cable and Connector for Next Generation Mobile Applications*, 2018, pp. 245–249. DOI: 10.1109/EMCSI.2018.8495293.

[85] D. Cho, C. S. Wood, S. C. Bennett, J. L. Roberts, and C. E. Wieman, "Precision measurement of the ratio of scalar to tensor transition polarizabilities for the cesium 6s-7s transition," *Phys. Rev. A*, vol. 55, pp. 1007–1011, 2 Feb. 1997. DOI: 10.1103/PhysRevA.55.1007. [Online]. Available: https://link.aps.org/doi/10.1103/PhysRevA.55.1007.

[86] S. A. Blundell, J. Sapirstein, and W. R. Johnson, "High-accuracy calculation of parity nonconservation in cesium and implications for particle physics," *Phys. Rev. D*, vol. 45, pp. 1602–1623, 5 Mar. 1992. DOI: 10.1103/PhysRevD.45.1602. [Online]. Available: https://link.aps.org/doi/10.1103/PhysRevD.45.1602.

[87] A. A. Vasilyev, I. M. Savukov, M. S. Safronova, and H. G. Berry, "Measurement of the $6s-7p$ transition probabilities in atomic cesium and a revised value for the weak charge Q_W," *Phys. Rev. A*, vol. 66, 020101(R), 2 Aug. 2002. DOI: 10.1103/PhysRevA.66.020101. [Online]. Available: https://link.aps.org/doi/10.1103/PhysRevA.66.020101.

[88] L. Young, W. T. Hill, S. J. Sibener, *et al.*, "Precision lifetime measurements of Cs 6p $^2P_{1/2}$ and 6p $^2P_{3/2}$ levels by single-photon counting," *Phys. Rev. A*, vol. 50, pp. 2174–2181, 3 Sep. 1994. DOI: 10.1103/PhysRevA.50.2174. [Online]. Available: https://link.aps.org/doi/10.1103/PhysRevA.50.2174.

[89] R. J. Rafac and C. E. Tanner, "Measurement of the ratio of the cesium D-line transition strengths," *Phys. Rev. A*, vol. 58, pp. 1087–1097, 2 Aug. 1998. DOI: 10.1103/PhysRevA.58.1087. [Online]. Available: https://link.aps.org/doi/10.1103/PhysRevA.58.1087.

[90] R. J. Rafac, C. E. Tanner, A. E. Livingston, and H. G. Berry, "Fast-beam laser lifetime measurements of the cesium $6p^2P_{1/2,3/2}$ states," *Phys. Rev. A*, vol. 60, pp. 3648–3662, 5 Nov. 1999. DOI: 10.1103/PhysRevA.60.3648. [Online]. Available: https://link.aps.org/doi/10.1103/PhysRevA.60.3648.

[91] A. Derevianko and S. G. Porsev, "Determination of lifetimes of $6P_J$ levels and ground-state polarizability of Cs from the van der waals coefficient C_6," *Phys. Rev. A*, vol. 65, p. 053 403, 5 Apr. 2002. DOI: 10.1103/PhysRevA.65.053403. [Online]. Available: https://link.aps.org/doi/10.1103/PhysRevA.65.053403.

[92] J. M. Amini and H. Gould, "High precision measurement of the static dipole polarizability of cesium," *Phys. Rev. Lett.*, vol. 91, p. 153 001, 15 Oct. 2003. DOI: 10.1103/PhysRevLett.91.153001. [Online]. Available: https://link.aps.org/doi/10.1103/PhysRevLett.91.153001.

[93] N. Bouloufa, A. Crubellier, and O. Dulieu, "Reexamination of the 0_g^- pure long-range state of Cs_2: Prediction of missing levels in the photoassociation spectrum," *Phys. Rev. A*, vol. 75, p. 052 501, 5 May 2007. DOI: 10.1103/PhysRevA.75.052501. [Online]. Available: https://link.aps.org/doi/10.1103/PhysRevA.75.052501.

[94] Y. Zhang, J. Ma, J. Wu, L. Wang, L. Xiao, and S. Jia, "Experimental observation of the lowest levels in the photoassociation spectroscopy of the 0_g^- purely-long-range state of Cs_2," *Phys. Rev. A*, vol. 87, 030503(R), 3 Mar. 2013. DOI: 10.1103/PhysRevA.87.030503. [Online]. Available: https://link.aps.org/doi/10.1103/PhysRevA.87.030503.

[95] B. M. Patterson, J. F. Sell, T. Ehrenreich, *et al.*, "Lifetime measurement of the cesium $6P_{3/2}$ level using ultrafast pump-probe laser pulses," *Phys. Rev. A*, vol. 91, p. 012 506, 1 Jan. 2015. DOI: 10.1103/PhysRevA.91.012506. [Online]. Available: https://link.aps.org/doi/10.1103/PhysRevA.91.012506.

[96] M. D. Gregoire, I. Hromada, W. F. Holmgren, R. Trubko, and A. D. Cronin, "Measurements of the ground-state polarizabilities of Cs, Rb, and K using atom interferometry," *Phys. Rev. A*, vol. 92, p. 052 513, 5 Nov. 2015. DOI: 10.1103/PhysRevA.92.052513. [Online]. Available: https://link.aps.org/doi/10.1103/PhysRevA.92.052513.

[97] C. E. Tanner, A. E. Livingston, R. J. Rafac, *et al.*, "Measurement of the $6p^2P_{3/2}$ state lifetime in atomic cesium," *Phys. Rev. Lett.*, vol. 69, pp. 2765–2767, 19 Nov. 1992. DOI: 10.1103/PhysRevLett.69.2765. [Online]. Available: https://link.aps.org/doi/10.1103/PhysRevLett.69.2765.

[98] J. F. Sell, B. M. Patterson, T. Ehrenreich, G. Brooke, J. Scoville, and R. J. Knize, "Lifetime measurement of the cesium $6P_{3/2}$ state using ultrafast laser-pulse excitation and ionization," *Phys. Rev. A*, vol. 84, 010501(R), 1 Jul. 2011. DOI: 10.1103/PhysRevA.84.010501. [Online]. Available: https://link.aps.org/doi/10.1103/PhysRevA.84.010501.

[99] G. Toh, J. A. Jaramillo-Villegas, N. Glotzbach, *et al.*, "Measurement of the lifetime of the $7s^2S_{1/2}$ state in atomic cesium using asynchronous gated detection," *Phys. Rev. A*, vol. 97, p. 052 507, 5 May 2018. DOI: 10.1103/PhysRevA.97.052507. [Online]. Available: https://link.aps.org/doi/10.1103/PhysRevA.97.052507.

[100] G. Toh, A. Damitz, N. Glotzbach, *et al.*, "Electric dipole matrix elements for the $6p\,^2P_J \rightarrow 7s\,^2S_{1/2}$ transition in atomic cesium," *Phys. Rev. A*, vol. 99, p. 032 504, 3 Mar. 2019. DOI: 10.1103/PhysRevA.99.032504. [Online]. Available: https://link.aps.org/doi/10.1103/PhysRevA.99.032504.

[101] M. S. Safronova, W. R. Johnson, and A. Derevianko, "Relativistic many-body calculations of energy levels, hyperfine constants, electric-dipole matrix elements, and static polarizabilities for alkali-metal atoms," *Phys. Rev. A*, vol. 60, pp. 4476–4487, 6 Dec. 1999. DOI: 10.1103/PhysRevA.60.4476. [Online]. Available: https://link.aps.org/doi/10.1103/PhysRevA.60.4476.

[102] S. C. Bennett, J. L. Roberts, and C. E. Wieman, "Measurement of the dc stark shift of the $6S \rightarrow 7S$ transition in atomic cesium," *Phys. Rev. A*, vol. 59, R16–R18, 1 Jan. 1999. DOI: 10.1103/PhysRevA.59.R16. [Online]. Available: https://link.aps.org/doi/10.1103/PhysRevA.59.R16.

[103] J. A. Quirk, A. Jacobsen, A. Damitz, C. E. Tanner, and D. S. Elliott, *Measurement of the static stark shift of the* $7s\ ^2S_{1/2}$ *level in atomic cesium*, 2023. arXiv: 2311.09169 [physics.atom-ph].

[104] D. Antypas and D. S. Elliott, "Measurement of the radial matrix elements of the $6s\,^2S_{1/2} \rightarrow 7p\,^2P_J$ transitions in atomic cesium," *Phys. Rev. A*, vol. 88, p. 052 516, 5 Nov. 2013. DOI: 10.1103/PhysRevA.88.052516. [Online]. Available: https://link.aps.org/doi/10.1103/PhysRevA.88.052516.

[105] A. Damitz, G. Toh, E. Putney, C. E. Tanner, and D. S. Elliott, "Measurement of the radial matrix elements for the $6s\,^2S_{1/2} \rightarrow 7p\,^2P_J$ transitions in cesium," *Phys. Rev. A*, vol. 99, p. 062 510, 6 Jun. 2019. DOI: 10.1103/PhysRevA.99.062510. [Online]. Available: https://link.aps.org/doi/10.1103/PhysRevA.99.062510.

[106] P. W. Pace and J. B. Atkinson, "The lifetimes of the $7^2P_{1/2}$ and $7^2P_{3/2}$ states of cesium," *Canadian Journal of Physics*, vol. 53, no. 10, pp. 937–941, 1975. DOI: 10.1139/p75-117. [Online]. Available: https://doi.org/10.1139/p75-117.

[107] J. Marek and K. Niemax, "The influence of collisions of Xe atoms on the lifetime of atomic states of Cs," *Journal of Physics B: Atomic and Molecular Physics*, vol. 9, no. 16, pp. L483–L488, Nov. 1976. DOI: 10.1088/0022-3700/9/16/005. [Online]. Available: https://doi.org/10.1088%5C%2F0022-3700%5C%2F9%5C%2F16%5C%2F005.

[108] M. Gustavsson, H. Lundberg, and S. Svanberg, "An efficient method for measuring atomic and molecular lifetimes using a modulated or deflected cw dye laser beam," *Physics Letters A*, vol. 64, no. 3, pp. 289–291, 1977, ISSN: 0375-9601. DOI: https://doi.org/10.1016/0375-9601(77)90365-6. [Online]. Available: http://www.sciencedirect.com/science/article/pii/0375960177903656.

[109] J. S. Deech, R. Luypaert, L. R. Pendrill, and G. W. Series, "Lifetimes, depopulation cross sections and hyperfine structures of some rydberg S and D states of ^{133}Cs," *Journal of Physics B: Atomic and Molecular Physics*, vol. 10, no. 5, pp. L137–L141, Apr. 1977. DOI: 10.1088/0022-3700/10/5/004. [Online]. Available: https://doi.org/10.1088%5C%2F0022-3700%5C%2F10%5C%2F5%5C%2F004.

[110] E. Campani, G. Degan, and G. Gobini, "Direct measurement of $7P_{1/2}$, $7P_{3/2}$ lifetimes in cesium," *Lettere al Nuovo Cimento (1971-1985)*, vol. 23, no. 5, p. 187, Apr. 1978, ISSN: 1827-613X. DOI: 10.1007/BF02856271. [Online]. Available: https://doi.org/10.1007/BF02856271.

[111] M. Ortiz and J. Campos, "Lifetime measurements of 7p levels of Cs(I) by means of laser excitation," *Journal of Quantitative Spectroscopy and Radiative Transfer*, vol. 26, no. 2, pp. 107–111, 1981, ISSN: 0022-4073. DOI: https://doi.org/10.1016/0022-4073(81)90070-4. [Online]. Available: http://www.sciencedirect.com/science/article/pii/0022407381900704.

[112] M. S. Safronova, U. I. Safronova, and C. W. Clark, "Magic wavelengths, matrix elements, polarizabilities, and lifetimes of Cs," *Phys. Rev. A*, vol. 94, p. 012 505, 1 Jul. 2016. DOI: 10.1103/PhysRevA.94.012505. [Online]. Available: %5C%5C%20https://link.aps.org/doi/10.1103/PhysRevA.94.012505.

[113] L. Shabanova, Y. N. Monakov, and A. Khlyustalov, "Oscillator strengths of lines in the principal series of cesium," *Optics and Spectroscopy*, vol. 47, pp. 1–3, 1979.

[114] L. Borvák, "Direct laser absorption spectroscopy measurements of transition strengths in cesium," Ph.D. dissertation, University of Notre Dame, 2014.

[115] V. A. Dzuba, V. V. Flambaum, A. Y. Kraftmakher, and O. P. Sushkov, "Summation of the high orders of perturbation theory in the correlation correction to the hyperfine structure and to the amplitudes of e1-transitions in the caesium atom," *Physics Letters A*, vol. 142, no. 6, pp. 373–377, 1989, ISSN: 0375-9601. DOI: https://doi.org/10.1016/0375-9601(89)90385-X. [Online]. Available: http://www.sciencedirect.com/science/article/pii/037596018990385X.

[116] A. Derevianko, "Reconciliation of the measurement of parity nonconservation in cs with the standard model," *Phys. Rev. Lett.*, vol. 85, pp. 1618–1621, 8 Aug. 2000. DOI: 10.1103/PhysRevLett.85.1618. [Online]. Available: https://link.aps.org/doi/10.1103/PhysRevLett.85.1618.

[117] V. A. Dzuba and V. V. Flambaum, "Off-diagonal hyperfine interaction and parity nonconservation in cesium," *Phys. Rev. A*, vol. 62, p. 052 101, 5 Oct. 2000. DOI: 10.1103/PhysRevA.62.052101. [Online]. Available: https://link.aps.org/doi/10.1103/PhysRevA.62.052101.

[118] S. C. Bennett and C. E. Wieman, "Measurement of the $6S \rightarrow 7S$ transition polarizability in atomic cesium and an improved test of the standard model," *Phys. Rev. Lett.*, vol. 82, pp. 2484–2487, 12 Mar. 1999. DOI: 10.1103/PhysRevLett.82.2484. [Online]. Available: https://link.aps.org/doi/10.1103/PhysRevLett.82.2484.

[119] J. Choi and D. S. Elliott, "Measurement scheme and analysis for weak ground-state-hyperfine-transition moments through two-pathway coherent control," *Phys. Rev. A*, vol. 93, p. 023 432, 2 Feb. 2016. DOI: 10.1103/PhysRevA.93.023432. [Online]. Available: https://link.aps.org/doi/10.1103/PhysRevA.93.023432.

A. ELECTRIC DIPOLE MATRIX ELEMENTS

A.1 Introduction

In this section, we discuss the measurements of electric dipole matrix elements made towards improving our understanding of the weak charge in cesium. For one of the experiments in the lab, led by Jonah Quirk, the goal is to measure E_{PNC}/β. Though the final variable of interest is Q_W, that depends on E_{PNC}. To be able to extract Q_W from our PNC measurement we must have a precise value of β, the vector polarizability, and $K_{PNC} = Q_W/E_{PNC}$, a theoretical calculation of the ratio of the weak charge to the amplitude of the PNC interaction [57]. To determine β, one can use a measurement of α/β [85] and a determination of α. To determine α, one can use a sum-over-states method like in Refs [86], [87], stated below.

$$\begin{aligned}\alpha &= \frac{1}{6}\sum_n \Bigg[\langle 7s_{1/2} \,||\, r \,||\, np_{1/2}\rangle\langle np_{1/2} \,||\, r \,||\, 6s_{1/2}\rangle \times \left(\frac{1}{E_{7s} - E_{np_{1/2}}} + \frac{1}{E_{6s} - E_{np_{1/2}}}\right) \\ &\quad - \langle 7s_{1/2} \,||\, r \,||\, np_{3/2}\rangle\langle np_{3/2} \,||\, r \,||\, 6s_{1/2}\rangle \times \left(\frac{1}{E_{7s} - E_{np_{3/2}}} + \frac{1}{E_{6s} - E_{np_{3/2}}}\right)\Bigg] \end{aligned} \quad \text{(A.1)}$$

$\langle np_J \,||\, r \,||\, ms_{1/2}\rangle$ are the electric dipole transition matrix elements and E_{ms} and E_{np_J} are state energies, where $J = 1/2$ or $3/2$ is the electronic angular momentum of the state, for the equation above. Therefore the precision of α depends heavily on the electric dipole transition matrix elements.

In addition, the matrix elements are important as benchmarks for theorists to produce more precise calculations of variables of interest that are experimentally inviable, like $K_{PNC} = Q_W/E_{PNC}$. K_{PNC} depends on the overlap of the nucleus with the electron waveform, which can not be experimentally measured directly. Therefore theorists use other values that experimentalists can measure, like dipole matrix elements and hyperfine constants, as benchmarks for their theory to be compared against. When the theory matches the measurements well, it serves as a guide to how well the theory can produce quantities that are not measurable. For our new measurement of the PNC amplitude, the most important matrix

elements are near the $6s\ ^2S_{1/2} \rightarrow 7s\ ^2S_{1/2}$ transition in cesium, the $\langle ms\ ^2S_{1/2} \mid\mid r \mid\mid np\ ^2P_J\rangle$, where $m, n = 6$ or 7 and $J = 1/2$ or $3/2$.

Our group has made significant progress in measuring many of the cesium matrix elements over the last couple years, mainly led by George Toh, Jonah Quirk, and me. The only matrix element not measured in our lab was the $\langle 6s\ ^2S_{1/2} \mid\mid r \mid\mid 6p\ ^2P_J\rangle$, as there had already been multiple, high precision experimental values that we didn't need to improve upon. For the rest of this chapter, I will go into detail how we reduced the uncertainty of these matrix elements to the 0.1% level.

A.2 6s 6p

For the $\langle 6s\ ^2S_{1/2} \mid\mid r \mid\mid 6p\ ^2P_J\rangle$ matrix elements, we found we did not need to remeasure them as they had been measured in a multitude of ways over the years. The different types of measurements include measuring the lifetime of the state, using the ground-state polarizability to calculate the matrix element, and other methods. These various methods of calculating the matrix value agree quite well as seen in Table A.1. From Refs. [88]–[98], we found the weighted average for the matrix elements to be $\langle 6s_{1/2} \mid\mid r \mid\mid 6p_{1/2}\rangle = 4.5057\,(16)\ a_0$ and $\langle 6s_{1/2} \mid\mid r \mid\mid 6p_{3/2}\rangle = 6.3398\,(22)\ a_0$. This obtains a precision of $\sim 0.035\%$ for these matrix elements.

A.3 6p 7s

A.3.1 Lifetime of the $7s$ State

For the $6p - 7s$ matrix elements we needed to complete two different experiments to obtain the value of the matrix element value, both led by George Toh. The first experiment was measuring the lifetime of the $7s$ state. The $7s$ state can decay two main ways as seen in Fig. A.1, either to the $6p_{3/2}$ or $6p_{1/2}$ state. The equation relating the matrix elements to the life time is:

$$\frac{1}{\tau_{7s}} = \sum_{\mathrm{j}=1/2,3/2} \frac{4}{3} \frac{{\omega_{\mathrm{j}}}^3}{c^2} \alpha \frac{|\ \langle 7s \mid\mid r \mid\mid 6p_{\mathrm{j}}\rangle\ |^2}{2\mathrm{j}' + 1}. \tag{A.2}$$

Table A.1. Values used to calculate the $\langle 6s\ ^2S_{1/2} \mid\mid r \mid\mid 6p\ ^2P_J \rangle$ values. Zhang et al. [94] reported slightly different lifetimes in the abstract vs. the text. The text value was used in this case. We calculated the weighted average of all the values in the table for the value labeled Weighted Average.

Author	Year	Measurement Type	$\langle 6S_{1/2} \mid\mid r \mid\mid 6P_{1/2} \rangle$	$\langle 6S_{1/2} \mid\mid r \mid\mid 6P_{3/2} \rangle$
Tanner et al. [97]	1992	fast-beam laser		6.3260(280)
Young et al., [88]	1994	time resolved fluorescence	4.5097(45)	6.3403(104)
Rafac et al. [90]	1999	fast-beam laser	4.4890(65)	6.3238(73)
Derevianko et al. [91]	2002	photoassociation	4.5064(45)	3.3424(63)
Amini et al. [92]	2003	ground-state polarizability	4.5116(41)	6.3498(56)
Bouloufa et al. [93]	2007	photoassociation	4.5051(233)	6.3404(313)
Zhang et al. [94]	2013	photoassociation	4.5058(45)	6.3404(63)
Gregoire et al. [96]	2015	atom interferometry	4.5080(40)	6.3450(50)
Patterson et al. [95]	2015	ultra-fast pump-probe laser		6.3349(48)
Weighted Average	2019		4.5057(16)	6.3398(22)

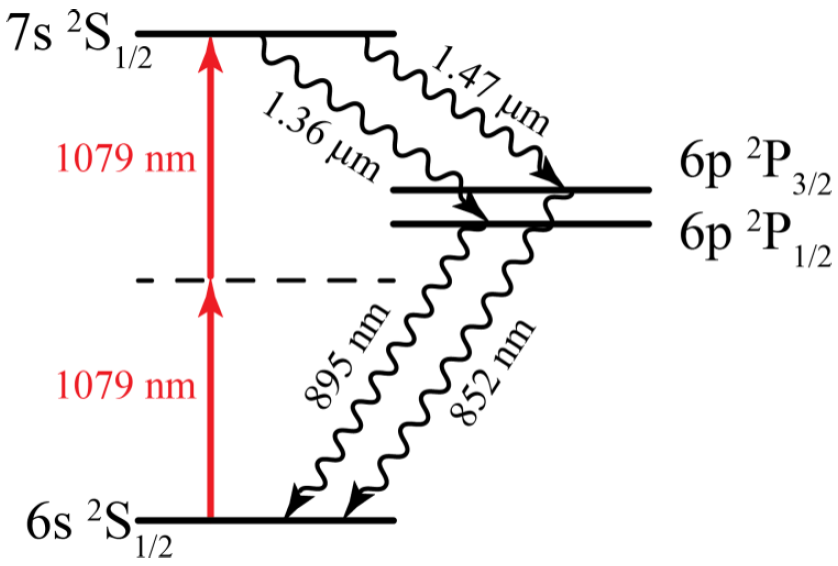

Figure A.1. Cesium energy levels showing the important energy levels of Cs-133 for the measurement of the lifetime of the $7s$ state.

where ω_{j} are the transition frequencies for the $7s\ ^2S_{1/2} \rightarrow 6p\ ^2P_{\mathrm{j}}$ transitions, $\mathrm{j}' = 1/2$ is the electronic angular momentum of the $7s\ ^2S_{1/2}$ state, c is the speed of light, and α is the fine structure constant.

In 2018 our group made a measurement of the $7s$ lifetime. We passed a 1079 nm laser beam through a cesium vapor cell to excite the ground state cesium atoms into the $7s$ state. An acousto-optical modulator (AOM) is used to quickly turn off the laser light to observe only the decay of atoms from the $7s$ state. The decay light is then detected in a single photon detector (SPD). We used the 1470 nm light as the decay light due to our access to a SPD that had good quantum efficiency there, reduction in possible radiation trapping effects due to not being a decay to the ground state, a higher branching ratio than the 1360 nm light (i.e. a higher chance of decaying at 1470 nm than 1360 nm), the time dependence of the decay signal being a single exponential form, and the ease of being able to filter out the unwanted light with a long-pass filter to only see the 1470 nm light. We then fit the decay curve to a single exponential curve and calculate the $7s$ lifetime as 48.28 ± 0.07 ns. More details on the experiment can be found in Ref. [99].

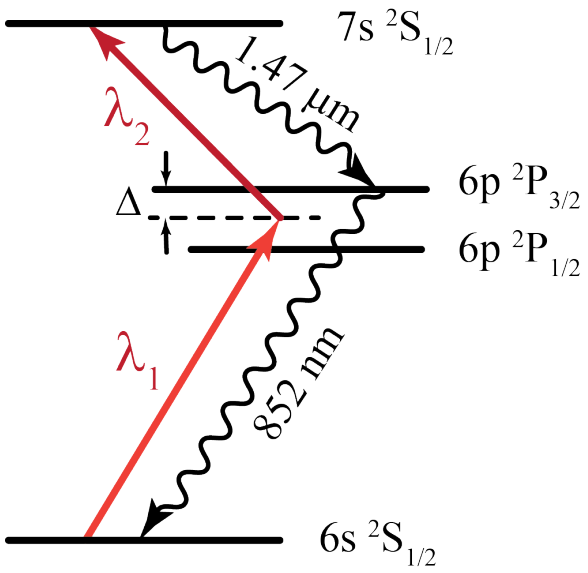

Figure A.2. Cesium energy levels of interest for the ratio of the $6p - 7s$ states. where λ_1 and λ_2 are the two different laser's wavelengths used in the experiment, $\sim$ 850 nm and $\sim$ 1470 nm

Measuring the lifetime is not enough to get the matrix element as the lifetime is related to both of the matrix elements. To get the matrix elements we needed another way to measure the relationship of the two matrix elements.

A.3.2 Ratio of the $\langle 7s_{1/2} \,||\, r \,||\, 6p_{3/2}\rangle / \langle 7s_{1/2} \,||\, r \,||\, 6p_{1/2}\rangle$

I worked with George Toh to measure the ratio of the two $6p - 7s$ states by comparisons of two-color, two-photon excitation rates of the $7s\,^2S_{1/2}$ state using laser beams with polarizations parallel to one another vs. perpendicular to one another. We used two different wavelength lasers at $\lambda_2 \sim 1470$ nm and $\lambda_1 \sim 850$ nm as seen in Fig. A.2. We changed the detuning, Δ in Fig. A.2, away from directly exciting the intermediate state $6p_{3/2}$, instead exciting the ground state cesium atoms through a intermediate virtual energy level to the $7s$ state. As Δ is changed, the transition rate of the perpendicular ($S_\perp$) to parallel ($S_\parallel$) polarization changes. We detected the changes in transition rate up to the $7s$ state by detecting

the fluorescence of the 852 nm decay light with a photo-multiplier tube (PMT). We chose this wavelength due to the PMT's we had access to being more efficient at this wavelength.

The strength of the transition from $6s\ ^2S_{1/2},\ F = 4 \rightarrow 7s\ ^2S_{1/2},\ F = 4$ component $(4 \rightarrow 4)$ for the parallel polarization can be written as:

$$S_{\parallel,4\rightarrow4} = \frac{2\pi}{\hbar^2}\frac{9}{16} \mid \tilde{\alpha} \mid^2 E_1^2 E_2^2, \tag{A.3}$$

with the amplitude of $\lambda_{\rm i}$ being $E_{\rm i}$ and

$$\begin{aligned} \tilde{\alpha} \;=\; & \frac{e^2}{6}\sum_n \Big[\langle 7s_{1/2} \mid\mid r \mid\mid np_{1/2}\rangle\langle np_{1/2} \mid\mid r \mid\mid 6s_{1/2}\rangle \\ & \times\left\{\frac{1}{\omega_2 - \omega_{np_{1/2}}} + \frac{1}{\omega_1 - \omega_{np_{1/2}}}\right\} \\ & -\langle 7s_{1/2} \mid\mid r \mid\mid np_{3/2}\rangle\langle np_{3/2} \mid\mid r \mid\mid 6s_{1/2}\rangle \\ & \times\left\{\frac{1}{\omega_2 - \omega_{np_{3/2}}} + \frac{1}{\omega_1 - \omega_{np_{3/2}}}\right\}\Big] \end{aligned} \tag{A.4}$$

where ω_1 is the frequency of the first laser, ~ 850 nm, and ω_2 is the frequency of the second laser, ~ 1470 nm. $\omega_{np_{1/2}}$ and $\omega_{np_{3/2}}$ are the frequency of the transition from $6s - np_{\rm j}$. The strength of the perpendicular polarization transition for $4 \rightarrow 4$ is different than the parallel with its strength being

$$S_{\perp,4\rightarrow4} = \frac{2\pi}{\hbar^2}\frac{15}{64} \mid \tilde{\beta} \mid^2 E_1^2 E_2^2, \tag{A.5}$$

where

$$\begin{aligned} \tilde{\beta} \;=\; & \frac{e^2}{6}\sum_n \Big[\langle 7s_{1/2} \mid\mid r \mid\mid np_{1/2}\rangle\langle np_{1/2} \mid\mid r \mid\mid 6s_{1/2}\rangle \\ & \times\left\{\frac{1}{\omega_2 - \omega_{np_{1/2}}} - \frac{1}{\omega_1 - \omega_{np_{1/2}}}\right\} \\ & +\frac{1}{2}\langle 7s_{1/2} \mid\mid r \mid\mid np_{3/2}\rangle\langle np_{3/2} \mid\mid r \mid\mid 6s_{1/2}\rangle \\ & \times\left\{\frac{1}{\omega_2 - \omega_{np_{3/2}}} - \frac{1}{\omega_1 - \omega_{np_{3/2}}}\right\}\Big]. \end{aligned} \tag{A.6}$$

When we take a ratio of the two different polarizations, seen below, we find that amplitudes of the laser's strengths no longer contribute and therefore the precision of the measurement is not dependent on our exact knowledge of that quantity as long as we keep the strength the same for the two polarizations.

$$\left(\frac{S_{\parallel}}{S_{\perp}}\right)_{4\to4} = \frac{12}{5}\,\frac{\mid\tilde{\alpha}\mid^2}{\mid\tilde{\beta}\mid^2}. \tag{A.7}$$

The transition from $6s\ ^2S_{1/2},\ F=3 \to 7s\ ^2S_{1/2},\ F=3$ component $(3\to3)$ is very similar to the $4\to4$, whose only difference is the constant in front with

$$S_{\parallel,3\to3} = \frac{2\pi}{\hbar^2}\frac{7}{16}\mid\tilde{\alpha}\mid^2 E_1^2E_2^2 \tag{A.8}$$

for parallel polarization, and

$$S_{\perp,3\to3} = \frac{2\pi}{\hbar^2}\frac{7}{64}\mid\tilde{\beta}\mid^2 E_1^2E_2^2 \tag{A.9}$$

for perpendicular polarization. The ratio of the two polarizations also follows a similar pattern to become:

$$\left(\frac{S_{\parallel}}{S_{\perp}}\right)_{3\to3} = 4\,\frac{\mid\tilde{\alpha}\mid^2}{\mid\tilde{\beta}\mid^2}. \tag{A.10}$$

Therefore the two different polarizations strengths will change as ω_1 and ω_2 change, or as Δ changes (the difference between $\omega_{6p3/2}$ and ω_1).

For this experiment we used a 1470 nm homemade ECDL in the Littmann configuration and a Ti:sapphire laser tuned near 850 nm. We chose a Littmann configuration for the 1470 nm laser due to it's unique feature of being able to be tuned over a wide-range of wavelengths without the output beam moving. The Ti:sapphire laser was coupled into a fiber for the light to be transferred over to the experiment table. We used a cesium vapor cell and counter-propagated the 850 nm and 1470 nm inside the cell. In each of the paths we have placed polarization optics in order to ensure the polarization purity of each laser. Through trial and error we learned that all of the optics needed to be mounted with soft plastic o-rings or flexible epoxy instead of metal o-rings or hard epoxy as they introduced birefringence strains

that effected the purity of the polarization. The strength of the transition was measured by ramping the Ti:sapphire laser over the transition and fitting the absorption spectrum to a Gaussian fit to obtain the height of the peak. We then measured the strength of the transition with the two lasers either having polarizations parallel to each other or perpendicular as a ratio of each other. We repeated this measurement over a range of 250 cm^{-1}, with the final results seen in Fig. A.3.

We then fit these results with the above equations to find that the ratio of the two matrix elements is $R = \langle 7s_{1/2} \mid\mid r \mid\mid 6p_{3/2}\rangle / \langle 7s_{1/2} \mid\mid r \mid\mid 6p_{1/2}\rangle = 1.5272\ (17)$. Then combined with the measurement of the lifetime of the $7s$ state, we were able to determine that $\langle 7s_{1/2} \mid\mid r \mid\mid 6p_{3/2}\rangle = -6.489\ (5)$ and $\langle 7s_{1/2} \mid\mid r \mid\mid 6p_{1/2}\rangle = -4.249\ (4)$. More details can be found in Ref. [100].

A.4 7s 7p

We found when we looked into how the $7s - 7p$ matrix elements were obtained, that Ref. [101] calculated them using a measurement of the dc Stark shift $\Delta\alpha_{6s7s}$ of the $6s \rightarrow 7s$ transition [102], the $7s - 6p$ matrix elements, and a measurement of the ground state polarizability α_{6s} [92], [96] in their calculation. They first calculated the polarizability of the $7s$ state, α_{7s}, from $\Delta\alpha_{6s7s}$ and α_{6s}. The polarizability of the $7s$ state then depends on the $7s - 7p$ and $7s - 6p$ matrix element values. Since we more precisely measured the $7s - 6p$ matrix elements from the last section, we can then use the same calculation as Ref. [101] but with our newly measured and more precise $7s - 6p$ matrix elements to more precisely obtain the $7s - 7p$ matrix elements. Our results from repeating this calculation are $\langle 7s_{1/2} \mid\mid r \mid\mid 7p_{1/2}\rangle = 10.325\ (5)\ a_0$ and $\langle 7s_{1/2} \mid\mid r \mid\mid 7p_{3/2}\rangle = 14.344\ (7)\ a_0$, which improves the uncertainty from 0.15% to 0.05%.

After Tan et al.[69], computed reduced electric-dipole matrix elements, they found the $7s - 7p$ had the largest disagreement between experiment and theory. This led our group to redo Bennett's [102] Stark shift measurement, led by Jonah Quirk [103]. This new experiment obtained a new value of the Stark shift and therefore new values for the $7s - 7p$ matrix

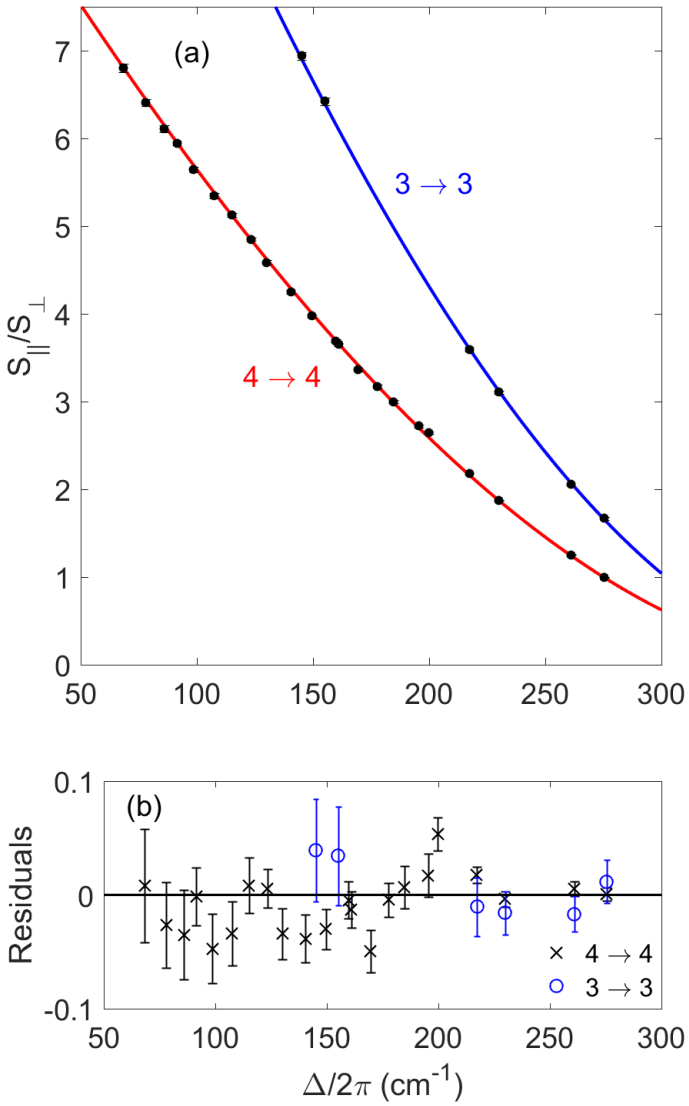

Figure A.3. From Ref. [100] of the change of $S_{\parallel}/S_{\perp}$ due to the change in detuning Δ. In (a) the red line is the curve from the $6s\ F = 4 - 7s\ F = 4$ while the blue line is the $6s\ F = 3 - 7s\ F = 3$. The data points are the experimental data, with those lying near the red line on the F=4-4 transition and those near the blue line the F=3-3 transition. In (b) we show the residual of the experimental data point to the theoretical curve, with the error bars showing the 1σ uncertainty (the error bars are also in (a) but are mostly smaller than the data point).

elements: $\langle 7s_{1/2} \,||\, r \,||\, 7p_{1/2} \rangle = 10.303\,(2)\ a_0$ and $\langle 7s_{1/2} \,||\, r \,||\, 7p_{3/2} \rangle = 14.312\,(3)\ a_0$ at lower uncertainty.

A.5 6s 7p

The last matrix elements are for the $6s - 7p$ transition. In the past, Antypas from our group measured them to less than 0.6% uncertainty [104]. The main contributor to the uncertainty was found to be the fact that the $6s - 7p_{1/2}$ absorption strength differed too much from the reference state, $6s - 6p_{1/2}$. Antypas was unable to obtain a large range of densities where both transitions were strong enough to be able to see both absorption curves, yet not too strong to the point of saturating one of the transitions. The level of precision of the two matrix elements could be improved by using two blue 450 nm lasers to directly compare the $6s - 7p_{3/2}$ and $6s - 7p_{1/2}$ matrix elements instead of only one blue 450 nm laser and a 894 nm laser to compare for both matrix elements.

Additionally as we worked on the experiment, we investigated how to fit the absorption curves. We discovered, both with newly collected data and the data Antypas collected, that there was a tiny difference of less than 1% between a purely Gaussian Doppler-broadened fit to the absorption curves and a proper Voigt profile fit to the curves. The Voigt profile is the convolution of the the Gaussian line-shape, due to Doppler-broadening, and a Lorenzian line-shape, due to the homogeneous natural linewidth of the transition and laser. We therefore used the more precise theoretical model with a Voigt profile to fit all of our curves to be confident with a 0.1% uncertainty. During our investigation of the absorption curves we also discovered the importance of the photodiode collecting the absorption curves having a fast enough fall/rise time to be able to record the absorption curve when the cesium goes from completely absorbing to fully transmitting the laser light. Therefore, we had to be careful with the scan speed of the laser over the transition and fall/rise time of the photodiode when collecting curves. To ensure the reliability of our results we decided to also re-do the measurement of the $6s - 7p_{3/2}$ matrix element, by repeating Antypas's measurement of the $6s - 7p_{3/2}$ matrix element with its reference to the $6s - 6p_{1/2}$ matrix element along with our

planned measurement of the $6s - 7p_{1/2}$ matrix element referenced to the $6s - 7p_{3/2}$ matrix element.

A.5.1 Theory

The experiment to measure the $6s - 7p_{\mathrm{j}}$ matrix elements used a narrow-band laser traveling through an atomic vapor cell to observe the amount of laser power that is transmitted through the cell. When the laser light's wavelength is the same as a transition of the atoms in the vapor cell, some of the laser's power is absorbed, causing a reduction in the transmitted laser power. The power transmitted in this situation can be written as

$$P(\omega) = P_0 \exp\{-2\alpha(\omega)\ell_{cell}\}, \tag{A.11}$$

where $\alpha(\omega)$ is the frequency-dependent electric field attenuation coefficient dependent on the atomic species, P_0 is the incident power on the vapor cell, and ℓ_{cell} is the length of the cell.

The key to figuring out the dependence of the transmitted power is how the frequency dependence works, $\alpha(\omega)$, which depends on the specifics of the experiment. For our experiment we are using linearly polarized laser light going through a vapor cell to a photodiode. We are not counter-propagating the laser, so the absorption curve will be Doppler-broadened. From Ref. [90], the form of $\alpha(\omega)$ can be written as

$$\alpha(\omega) = \frac{2\pi^2 n \alpha_{\mathrm{fs}} \omega}{(2I+1)(2J+1)} \mid \langle J' \mid\mid \vec{r} \mid\mid J \rangle \mid^2 \times \sum_{F'} \sum_{F} q_{J,F\to J',F'} V(\omega), \tag{A.12}$$

which involves the matrix elements. From the equation, n is the number density of the cesium atoms along the laser's path, α_{fs} is the fine-structure constant, and ω is the frequency. J is the quantum number for the total electric spin, I is the quantum number for the nuclear spin, and F is the quantum number for the total angular momentum (where m is the projection of F on the z-axis). To distinguish between the ground and excited states, we are using prime

Table A.2. Calculated values from Eq. (A.13) for the hyperfine components of interest for the $6s\ ^2S_{1/2} \rightarrow np\ ^2P_{\mathrm{j}}$ transition.

$F \rightarrow F'$	$6s\ ^2S_{1/2} \rightarrow np\ ^2P_{1/2}$	$6s\ ^2S_{1/2} \rightarrow np\ ^2P_{3/2}$
$4 \rightarrow 3'$	7/8	7/48
$4 \rightarrow 4'$	5/8	7/16
$4 \rightarrow 5'$	–	11/12
$3 \rightarrow 2'$	–	5/12
$3 \rightarrow 3'$	7/24	7/16
$3 \rightarrow 4'$	7/8	5/16

notation to denote the excited state (i.e. m') and unprimed to denote the ground state (i.e. m). $q_{J,F\rightarrow J',F'}$ are factors that depend on the hyperfine component and can be written as

$$\begin{aligned} q_{J,F\rightarrow J',F'} &= (-1)^{2(I+J)}\,(2F'+1)\,(2F+1) \\ &\quad \times \sum_{m,m'} \begin{pmatrix} F' & 1 & F \\ -m' & 0 & m \end{pmatrix}^2 \begin{Bmatrix} J' & F' & I \\ F & J & 1 \end{Bmatrix}^2, \end{aligned} \tag{A.13}$$

where the array in parentheses are the Wigner 3j symbol and the array in the curly brackets are the Wigner 6j symbol. They are also tabulated for the transitions used in this experiment in Table A.2. Finally $V(\omega)$ is the Voigt profile, the convolution of the Gaussian distribution and homogeneous Lorentzian. It can be written as

$$V(\omega) = \sqrt{\frac{\ln 2}{\pi^3}} \frac{1}{\Delta\omega_D} \int_{-\infty}^{\infty} \frac{\Gamma' \mathrm{e}^{-4\ln 2(\omega_D/\Delta\omega_D)^2} d\omega_D}{\left[\omega - \omega_D - \omega_{F\rightarrow F'}\right]^2 + \Gamma'^2/4}, \tag{A.14}$$

where $\Delta\omega_D$ is the width of the Gaussian distribution and Γ' is the width of the Lorentzian distribution. $\omega_{F\rightarrow F'}$ is the transition frequency between the hyperfine components $F \rightarrow F'$ and ω_D is the Doppler shift. The Voigt profile is properly normalized such that integrating over the resonance goes to one.

The above equations explicitly depend on atomic density in the vapor cell. Therefore to achieve high precision we would need to precisely know the density in the vapor cell. Additionally, our precision would also be limited by the uncertainty with which we know the

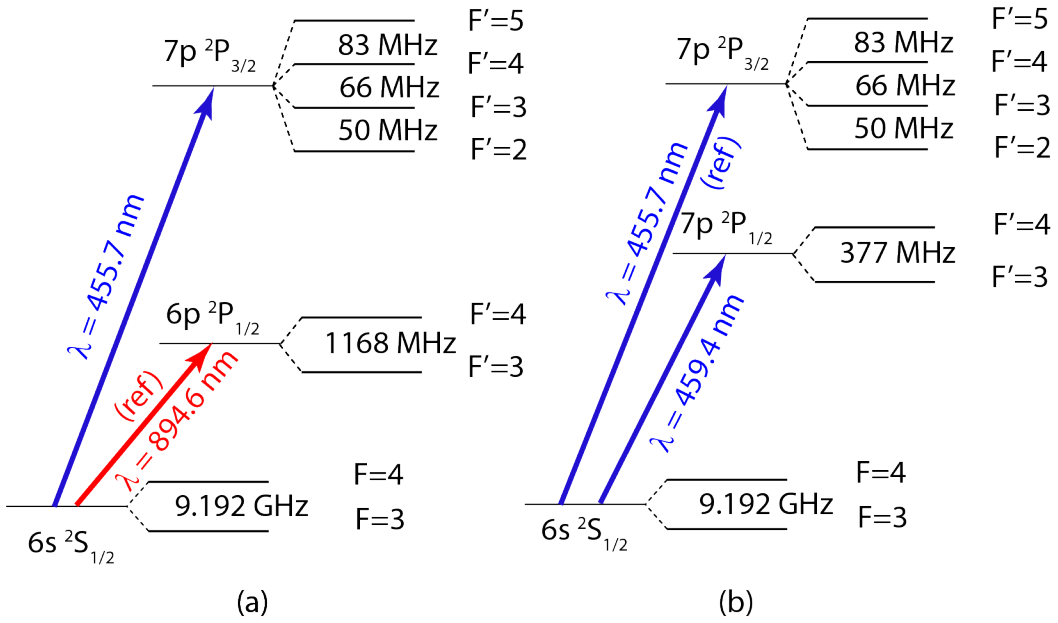

Figure A.4. From Ref. [105]. The energy levels of interest for the experiment. (a) is for measuring R_1 and (b) is for measuring R_2.

length of the cell. To simplify the experiment instead we will take a ratio of two different transitions absorption strengths, one being a reference transition that is known well, in which the length of the cell and the density of the atomic vapor will be the same for both and thus eliminate our measurements dependence on these quantities. One stipulation of taking the ratio is we must take our measurements of the two different transitions in a short enough time that the atomic vapor density does not change. To measure the two matrix elements of interest we will conduct two experiments. First we will measure the $6s-7p_{3/2}$ matrix element by using the $6s-6p_{1/2}$ matrix element as the reference element. Then we will measure the $6s-7p_{1/2}$ matrix element with the reference matrix element our newly measured matrix element from the $6s-7p_{3/2}$ state. The associated energy levels are illustrated in Fig. A.4.

The first ratio we measure is

$$R_1 \equiv \frac{\langle 6s_{1/2} \,||\, r \,||\, 6p_{1/2}\rangle}{\langle 6s_{1/2} \,||\, r \,||\, 7p_{3/2}\rangle} = \sqrt{\frac{\alpha^{894}_{3\to 3'}(\omega_0)/(7/24)}{\alpha^{456}_{F\to F'}(\omega_0)/q_{F\to F'}}}. \tag{A.15}$$

We find that the $\alpha^{456}_{F\to F'}(\omega_0)/q_{F\to F'}$ is the same for all of the hyperfine components of each of the transitions, so to simplify the expression we will use

$$\Upsilon^{\lambda} = \alpha^{\lambda}_{F\to F'}(\omega_0)/q_{F\to F'} \tag{A.16}$$

such that R_1 becomes

$$R_1 = \frac{\langle 6s_{1/2} \,||\, r \,||\, 6p_{1/2}\rangle}{\langle 6s_{1/2} \,||\, r \,||\, 7p_{3/2}\rangle} = \sqrt{\frac{\Upsilon^{894}}{\Upsilon^{456}}}. \tag{A.17}$$

The second ratio we will measure will be between the two $6s - 7p_J$ states, written as

$$R_2 \equiv \frac{\langle 6s_{1/2} \,||\, r \,||\, 7p_{3/2}\rangle}{\langle 6s_{1/2} \,||\, r \,||\, 7p_{1/2}\rangle} = \sqrt{\frac{\Upsilon^{456}}{\Upsilon^{459}}}. \tag{A.18}$$

A.5.2 Setup

The equipment setup we use for the experiment is shown in Figure A.5. The lasers we are using are all homemade external cavity diode lasers (ECDL) in the Littrow configuration. The 894 nm laser and one of the 450 nm lasers are the same diodes used by Antypas from our group's previous experiment. Additionally, the 450 nm laser is in the same cavity as before, but re-tuned back into alignment, with the 894 nm laser setup in a whole new cavity. We obtained another 450 nm laser, but found that it could not reach up to 459 nm for the $7p_{1/2}$ transition, so we used the old 450 nm laser for the $7p_{1/2}$ transition at 459 nm and the new 450 nm laser for the $7p_{3/2}$ transition at 456 nm. We were able to tune the frequency of the lasers by tuning the current, temperature, and PZT of each of the lasers. By further using a feed-forward circuit to tune the current of the laser and voltage going to the PZT simultaneously, we were able to achieve a 4-10 GHz mode-hop free tuning range for each of the lasers. This mode-hop free tuning range is far greater than the width of the Doppler-broadened spectra, allowing us to obtain the whole spectrum, including regions of no absorption for all of the spectrum.

Each of the lasers produces power in the 10 mW range, which we stabilized using an AOM and a photodiode. We oriented the AOM such that we saw the first-order diffraction beam coming out when rf power was supplied to the AOM. The diffracted beam is blocked and

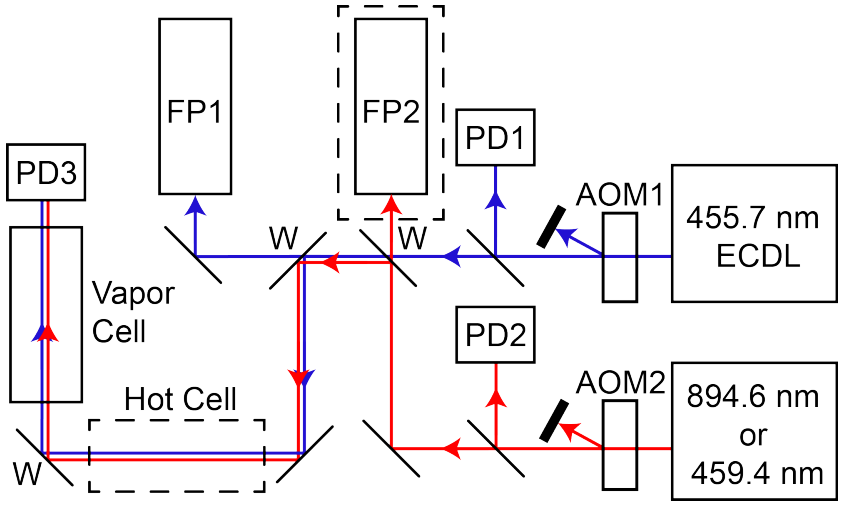

Figure A.5. From Ref. [105]. The setup for measuring the $6s - 7p_{3/2}$ and $6s - 7p_{1/2}$ matrix elements. The 455.7 nm laser is used for both measurements. The 894.6 nm or 459.4 nm laser changes depending on the measurement, R_1 or R_2 respectively, being done. (AOM1,2) acousto-optic modulators; (ECDL) external cavity diode laser; (PD1-3) photodiodes; (FP1,2) Fabry-Pérot cavities; and (W) wedged windows. FP2 (in the dashed box) is used only for the measurement of R_1.

then a portion of the undiffracted beam is diverted to a photodiode. We used the photodiode current to observe the relative power of the laser. With this readout we were able to create an error signal that we used to send to the controller of the rf power to adjust the rf power such that the undiffracted beam maintains relatively flat power over the whole scan, while dumping excess power into the diffracted beam that is blocked. We needed the constant laser power to help ensure any change to the signal is due solely to absorption in the vapor cell and not due to laser power changing. We managed to get the laser power variation to less than 3% variation over a 4-6 GHz scan of the 456 nm and 459 nm lasers and to less than a 0.5% variation over a 4-6 GHz scan for the 894 nm laser.

To reduce any impact due to saturation of the transition, we diminished the laser power using a combination of wedged windows and neutral density filters to around the 100 nW level for the 450 nm lasers and the 10 nW level for the 894 nm laser. The size of the 456 nm and 459 nm lasers at the vapor cell was $\sim$ 1.2 by 0.8 mm with the 894 nm laser bigger with a size of $\sim$ 2 by 2 mm. We had the 894 nm laser both bigger and with less power than the 450 nm lasers to attain similar levels of saturation of the transition. This is due to $6s - 6p_{1/2}$ transition being stronger at similar laser powers to the $6s - 7p_{\mathrm{j}}$ transitions.

We calibrated the frequency scans using Fabry-Pérot cavities at appropriate wavelengths for each laser frequency, with both of the 450 nm lasers using the same cavity and the 894 nm laser having it's own cavity. The cavities both had free spectral ranges of about 1500 MHz. We then had the laser going to both the cavity and through the vapor cell at the same time to be able to map the time scale to a frequency one for the absorption spectrum. To make use of the power we were dumping with the wedged windows we ended up using the unused power to send to the Fabry-Pérot cavity.

We also used the wedged windows to overlap the two lasers needed to drive the transitions of interest for the experiment, seen in Fig. A.4. We went to great lengths to ensure the two lasers overlapped, so that way we were assured that they traveled the same distance, over the same atomic density, in the vapor cell. We sent the laser beams over a distance of 14 m away to observe the quality of the overlap of the two beams. The beams were overlapped such that any possible divergence of the two beams to being parallel is 0.05 mrad, or less

than a 0.5 mm difference in the vapor cell. This ensures that any possible difference in the path length is under 0.02%.

Additionally, we left space in the beam path for another vapor cell that we could remove and insert easily from the path. This cell is labeled as the Hot Cell in the experimental setup in Figure A.5. We heated this cell to around 120°C, significantly higher than the vapor cell used for the main measurement. This ensured that all of the laser light that was on transition with the cesium in the vacuum chamber was absorbed in the Hot Cell. Any light that made it to the final photodiode was solely due to the power in the laser's wings that was not at the transition frequency. We used this measurement to deduct off this power in the laser wings from our final absorption spectra measurement.

The main vapor cell we used was borrowed from Carol Tanner at the University of Notre Dame. It was made in house at the university in order to have good control and knowledge over the dimensions of the cell. The main dimensions of interest for this experiment are that the total length of the cell is 29.9034(44) cm and both windows the laser beam passes through are flat. It also had a very long cold finger in the cell to help achieve stable and reliable control over the density of cesium in the cell. We maintained the body of the vapor cell at $\sim$ 25°C with the cold finger's temperature ranging over -8°C to 18°C to obtain different cesium densities in the cell. We were able to maintain the two different temperatures by encasing the main body of the cell with Kapton heaters and insulation to create a stable temperature and inserting the cold finger into a block of copper. The temperature of the copper block was controlled by using a thermoelectric cooler and a temperature sensor to create a feed back control. This allowed us separate control over the cold finger and main body temperatures.

We used two different vapor cells for the final vapor cell for the R_2 measurement to ensure that there was no significant effect due to miscellaneous atoms getting into the vapor cell or effects from the length of the interaction path/total density in the cell (we could use different temperature ranges due to the difference in path length). Along with cell mentioned above, we used a smaller, $\sim$ 6 cm, cell with wedged windows (0.5°). We achieved a similar setup of inserting the cold finger of the vapor cell into an aluminum block, using a thermoelectric cooler and temperature sensor to control the temperature of the cold finger. We encased the

main body of the cell with heat tape that was coiled around the cell in a random pattern to prevent fields from forming in the vapor cell due to the current flowing through the heat tape. The main body was then wrapped in aluminum foil to help maintain a uniform and stable temperature in the vapor cell. We maintained a uniform temperature of around 80°C in the main body of the cell and changed the temperature of the cold finger over a range of 40°C to 60°C.

Finally, the final photodiode needed to be carefully crafted in order to ensure we were not scanning through the absorption spectra faster than the photodiode could record the signal. Also, due to the necessary constraint at working at low laser powers to reduce saturation intensity effects, we needed the photodiode to be sensitive and low noise. We used a silicon photodiode that was sensitive to both 450 nm and 894 nm, the FDS010 diode from Thorlabs. It has a 1 ns rise time, responsive over 200 - 1100 nm, and a Ø1 mm^2 active area. We amplified the current of the photodiode in a transimpedance amplifier that had a gain of $5 \times 10^7 V/A$. We further had to increase the signal with a second gain stage of 10. Additionally in order to ensure the system was fast enough to map out the whole spectrum we slowed down the scan speed of the laser frequency down to about 4 GHz/s along with a wide amplifier bandwidth of 60 kHz. We initially were scanning much quicker to make data collection faster but found out that as we changed the scan rate of the laser, we changed the apparent depth of the absorption spectrum. We decreased the speed of the scan (and increased the bandwidth of the amplifier when needed) until changing scan speed either faster or slower did not change the depth of the absorption spectra, deciding that the fall and rise times of the photodiode were sufficient to observe the total change due to the cesium absorbing the laser light. For the R_2 measurement, due to the fact that the absorption strengths were more similar for the 459 nm and 456 nm lasers than the 456 nm and 894 nm, we were able to use less deep absorption spectrum for both transitions and as such was able to speed up the scan of the laser frequency to capture eight full absorption spectrum in 8s (using the same method as before to ensure the photodiode could sufficiently capture the spectrum). Additionally we were able to increase the signal-to-noise ratio by decreasing the detector bandwidth to 2 kHz.

In order to ensure all laser beam's light hits the photodiode sensor we have placed a 15 cm focal length lens after the vapor cell and before the photodiode. This allows us to reduce the size of the laser beam to less than the size of the photodiode. Due to the sensitivity of the photodiode, we had to perform the experiment without room lights on in addition to inserting a cylinder of aluminum foil in the distance between the vapor cell and the photodiode. This reduced the background signal, with no laser light, to that of just the photodiode and transimpedance amplifier circuit.

A.5.3 R_1 and R_2 Measurement

To measure R_1 or R_2, we need to obtain absorption curves where we can be confident in the depth of the curve. In order to do this we need to measure the total amount of signal that comes from noise on the photodiode circuit, what will be called the background offset level, along with any signal that comes from off-resonant laser light (power in the wings of the laser power spectrum) during the on-resonant laser frequency scan, which will be called laser wing power. To measure the background offset level is simply done by blocking both of the lasers from reaching the vapor cell, and recording the photodiode signal. For the R_1 measurement, the background offset was around 15-17 mV, varying over the day. Therefore before each run we recorded the background signal. For the measurement of R_2, due to having the better signal-to-noise ratio for the photodiode with a lower bandwidth, the background level was only about 1 mV. Any variations in the 1 mV were well within our uncertainty and as such we only recorded the background signal a couple of times during the day instead of before every run.

To measure the power in the laser wings, we inserted the hot cell in the path of the laser and recorded the amount of signal left after all of the on-resonant laser light was absorbed in the hot cell, seen in Figure A.6. We found that the 456 nm laser had about 0.1% laser power in the wings, about 1% for the 894 nm laser, and about 0.3% in the 459 nm laser. To find the signal solely due to the laser wing power, we subtracted off the background power. Unfortunately, adding the additional cell did effect the amount of total laser power hitting the photodiode, so we had to account for the fact that some of the power in the laser wings

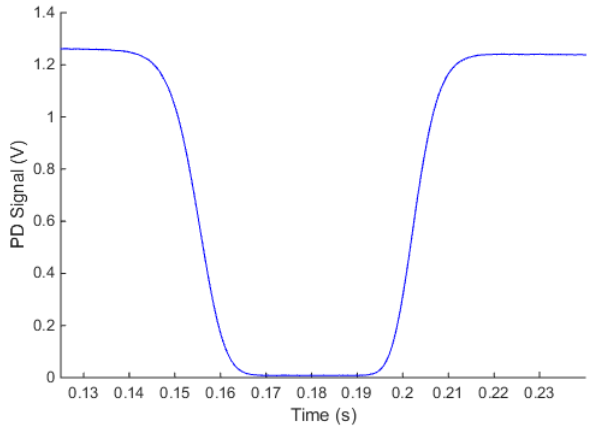

Figure A.6. An example of the complete absorption due to the hot cell being in the path of the 459 nm laser.

was being lost in additional windows of the hot cell. Therefore, we took a ratio of the total voltage level without the hot cell to that with the hot cell (i.e. the flat level amount of voltage with no absorption), and multiplied the corrected measured laser wing power by this ratio to find out how much laser wing power is there without the hot cell. The ratio of $\frac{nohotcell}{hotcell}$ was usually about 1.1 to 1.3, depending on how well we lined up the hot cell in the path again. We then added back in the background signal to find the total offset signal. We preformed the measurement of the laser wing power before each run for both the measurements of R_1 and R_2. Then we took off the total offset signal value for all of the absorption spectra in the run. For a couple of the runs we did repeat measuring the hot cell absorption spectra again at the end of the run but found that there was not a significant change over the course of the run. We decided that the measurement of the laser wing power at the beginning of the run was sufficient.

For a complete run of a measurement, after we collect the hot cell signal, we block one of the lasers while letting the other one through to the vapor cell. We then record about four full absorption curves over 10 seconds for the measurement of R_1 and about eight full absorption curves over 2 seconds for the measurement of R_2. We then switch which laser is blocked and repeat. We then repeat this process until we have 3 records of the second laser and 4 records of the first laser. This allows us to see if the density changed over the time

and average out the density change if it is linear and slow enough. Also, this allows us to get more records of the more uncertain absorption curves to help reduce the uncertainty. For that reason, during the R_1 measurement, the first laser was the 894 nm laser and the second laser was the 456 nm laser. This was mainly due to the fact that the 894 nm absorption on resonance was near enough complete that small variations in the depth of the signal that were recorded caused major changes in the fitting of the Υ^{894} as compared to the 456 nm laser were similar variations in absorption depth did not effect Υ^{456} as significantly. For the R_2 measurement the first laser was the 459 nm laser and the second was the 456 nm. In this case we kept the 456 nm laser's absorption well below complete in order to increase our speed scan and increase the signal to noise, so the smaller 459 nm absorption curve's fit was more uncertain due to the smaller depth of the curve. Examples of the absorption curves and fits are shown in Figures A.7 and A.8. Notice the difference in the size of the residual spread being greater for the 894 nm and 456 nm spectra in comparison to the 456 nm and 459 nm mainly due to the increase in photodiode bandwidth.

After we complete the measurement, we wait awhile and repeat a few more times at the same cold-finger temperatures, which helps us verify that the density of the atoms was indeed stable over the records. After we are satisfied that the records were run while the atomic density was stabilized, we changed the temperature. We waited until the temperature stabilized and then repeated the measurement process again. In this way were able to record multiple measurements at similar densities and repeat it over a wide range of densities to investigate a wide range of values for all of the Υ^{λ}. In addition we also did one measurement with the vapor cell completely removed from the system to verify the absence of the absorption spectrum features from the scan, adding a point at $\Upsilon^{\lambda} = 0$ on our range of values.

As we perform the experiment we have the choice of exciting from the $6s$ F=4 or F=3 ground hyperfine state. For the R_1 measurement we chose to excite solely from the F=3 for the 894 nm laser and F=4 for the 456 nm laser. This allowed a longer range of Υ^{λ} with both of the absorption curves of similar depth. Therefore since 894 nm absorption curve is deeper than the 456 nm curve and the F=3 ground state transition is weaker than the F=4 state transition, we chose the starting state for both that decreased the 894 nm transition

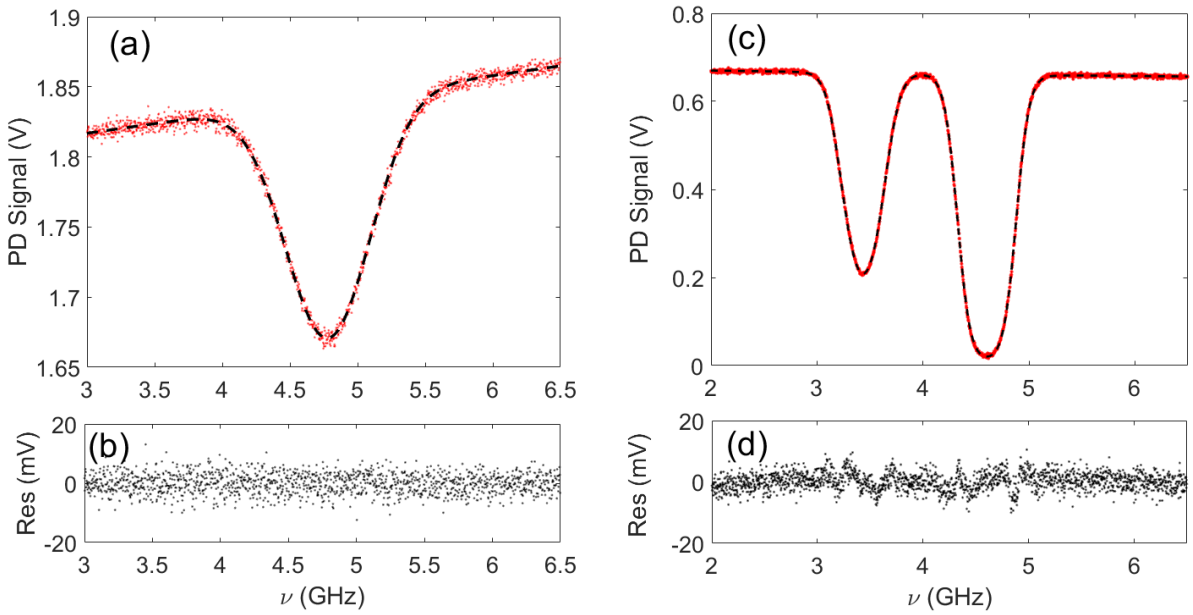

Figure A.7. Absorption spectra examples for the 456 nm and 894 nm lasers. The x-axis is the laser frequency as we scan the laser and the y-axis is the photodiode signal after correction for the total offset in the signal from the laser wings and background noise. The red data points are the experimental data while the dashed black line is the fit from Equation A.11. The cold finger was at $-2°$C. (a) The 456 nm spectrum is from the transition from F=4 to F′=3′,4′,5′, where the upper state hyperfine structure is not resolved. (c) The 894 nm spectrum is from F=3 to F′=3′,4′, where the upper state hyperfine structure is resolved. (b) The residual (data-fit) for the 456 nm curve from (a). (d) The residual (data-fit) for the 894 nm curve from (c).

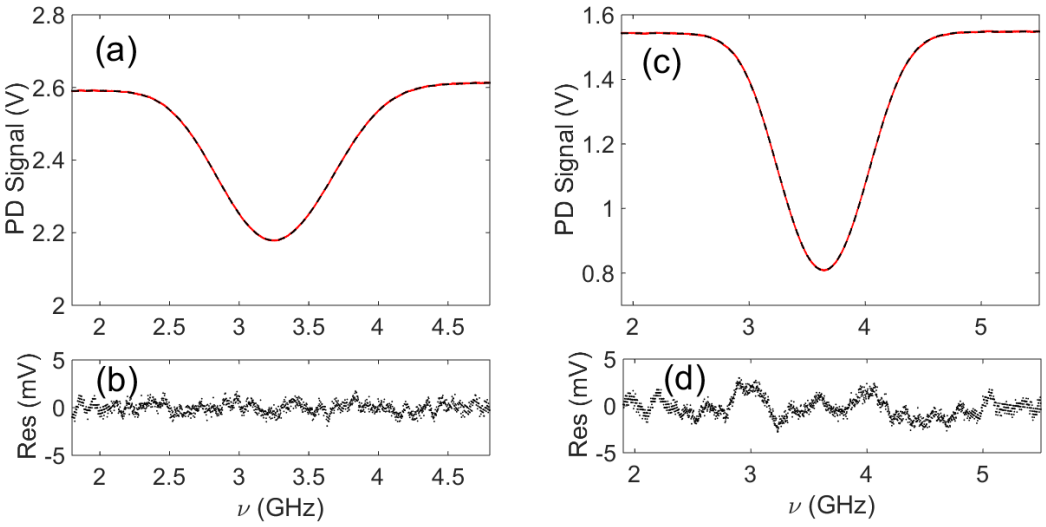

Figure A.8. Absorption spectra examples for the 456 nm and 459 nm lasers. The x-axis is the laser frequency as we scan the laser and the y-axis is the photodiode signal after correction for the total offset in the signal from the laser wings and background noise. The red data points are the experimental data while the dashed black line is the fit from Equation A.11. The cold finger was at 56°C and the 6 cm vapor cell was used. (a) The 459 nm spectrum is from the transition from F=4 to F′=3′,4′, where the upper state hyperfine structure is not resolved. (c) The 456 nm spectrum is from F=4 to F′=3′,4′,5′, where the upper state hyperfine structure is not resolved. (b) The residual (data-fit) for the 459 nm curve from (a). (d) The residual (data-fit) for the 456 nm curve from (c).

and increased the 456 nm. For the R_2 we ran two complete runs of just comparing the F=3 starting state for 456 nm and 459 nm and then just the F=4 (we also did one more run with the F=3 starting state but with the longer vapor cell instead of the shorter cell to test for background or density variation effects).

After we collect the absorption curves we need to fit them to Equation A.11 to obtain the Υ^{λ} value for the curve. Our first step in accomplishing this goal is to convert the time scale on the x-axis into a frequency scale. We use the Fabry-Pérot cavity to convert time into frequency. To do this we use the transmission peaks of the Fabry-Pérot cavity, ensuring we have at least four peaks over the scale (typically there are five transmission peaks from the cavity over the absorption curve scan). We then fit them to a third-order polynomial to relate the time scale of the photodiode scan to the laser frequency change over that time. We fit to the third-order polynomial instead of the second-order to catch any non-linearity in the scan. While working with the fits, we found that changes to the value of the free-spectral range (FSR) of the Fabry-Pérot cavity of a couple of MHz would change the fitted value of Υ^{λ}.

We found that just using the approximate FSR of the cavity of $\sim$ 1500 MHz was not precise enough. Therefore we had to experimentally find the FSR of the cavity. This was accomplished through fitting the absorption curves and changing the presumed FSR value of the cavity. Due to our precise understanding of the frequency splitting of the hyperfine components in the $7p$ and $6p$ states, when the FSR is off, and therefore the frequency calibration of the scan is off, there is extra structure in the residuals of the fits. The measured values for the frequency difference between the hyperfine components we used is found in Ref. [30]–[33]. We found that between the blue lasers that the 459 nm absorption curves in particular were sensitive to changes in the FSR value, with extra structure appearing when the FSR was off. The 894 nm absorption peaks were even more sensitive due to the fact that the two hyperfine peaks are clearly distinct, unlike the $7p$ states where all of the hyperfine structure overlaps to form just one peak. The FSR for each absorption curve was determined by calculating the residual for each FSR value and finding the minimum value. We repeated the process thirty times for the 894 nm Fabry-Pérot cavity and 90 times for the blue laser cavity (due to the higher spread in minimum FSR values compared to the

894 nm spectrum). We determined that the FSR for the 450 nm Fabry-Pérot cavity was 1501.6(10) MHz while the 894 nm FSR is 1481.9(4) MHz. We then take those FSR values for the third-order polynomial fit to the Fabry-Pérot cavity transmission peaks.

After we translate the time scale to a frequency scale we can fit the absorption curves to Eqs. (A.11)−(A.14). We have five adjustable values, the value of the total transmitted laser power through the cell, a term that accounts for a slope in the total transmitted laser power, the center frequency of one of the hyperfine components in the curve (can be any one), the linewidth of the Doppler broadened width, and Υ^{λ}, the value we want. We fixed the Lorenzian linewidth for the Voigt line shape as $\Gamma' = 2\pi(\Delta\nu_N + 0.2 \text{ MHz})$, where $\Delta\nu_N$ is the natural linewidth for the final state where $\Delta\nu_N = 4.6$ MHz [88]–[98] for the 894 nm laser absorption spectrum, 1.22 MHz [106]–[111] for the 456 nm absorption spectrum, and 1.06 MHz [106]–[111] for the 459 nm absorption. The 0.2 MHz is for the linewidth of the laser, which is approximately the same for all of the lasers as they are all Littrow style ECDL lasers, with more details later on how we experimentally found the value. We also fixed the relative heights of the hyperfine components using the $q_{F\to F'}$ factors in Table A.2. After the fit we verified that the Doppler broadened width was near our predicted values from the approximate temperature based off of the Doppler full-width-at-half-maximum (FWHM), $\Delta\omega_D$, of the transition, equal to $\omega\sqrt{8k_BT\ln 2/(Mc^2)}$. The 894 nm absorption curve was $\sim$ 360 MHz, the 456 nm and 459nm absorption curves were $\sim$ 700 MHz.

We experimentally measured the linewidth of the lasers by beating them against another laser near the same frequency. For the 894 nm laser, we have access to a frequency comb that covers 894 nm. We overlapped the 894 nm laser and the frequency comb on a fast photodiode, sending the photodiode's signal to a rf spectrum analyzer. We can then analyze the bandwidth of the 894 nm by observing the beat note on the rf spectrum analyzer. As the frequency comb's laser width is tiny in comparison to the 894 nm laser, any width in the beat note is mainly due to the 894 nm laser. For the 456 nm and 459 nm lasers, the frequency comb does not go down to this wavelength, so we beat the two 450 nm lasers against each other. Since both 450 nm lasers were ECDL lasers in Littrow configuration, we assumed that their linewidths would be similar. Therefore the beat note's width would have similar contributions from both lasers. Over the long term scale of a full measurement set,

all of the beat notes traversed 2-3 MHz. We attributed this spread due to the vibrations in the cavity. On single scan the width of all of the beat notes was on the few hundred of kHz scale, around 200 kHz. Due to the variety of widths of beat notes, we estimated a conservative uncertainty of 200 kHz. As stated earlier, we added the natural linewidth of the laser to the Lorenzian linewidth. Additionally, we added the longer term drifts in the beat notes to the Doppler width, as the longer term fluctuations would contribute to this length. We found that the natural linewidth of the laser did slightly affect the results while the longer term drifts were negligible as we were adding 2-3 MHz to 300 or 700 MHz.

After we fit each curve, we found that the uncertainty coming from the fit was too low to explain the spread in Υ^{λ} values over one measurement run. Our understanding of this is we collected enough data over the absorption curve that when the fit uncertainty was computed it was artificially reduced from the number of data points close to the fit. We therefore took the Υ^{λ} from each curve fit in the run (sixteen 894 nm curves and twelve 456 nm curves for R_1 or thirty-two 459 nm scans and twenty-four 456 nm scans for R_2) and computed the average and standard deviation for the run. We repeated this for every run.

One note of concern we discovered while collecting absorption curves was when the unabsorbed laser power surrounding the absorption curve was not a horizontal, flat line. We attributed the non-zero slope or curve mainly to etalon effects, the variation in transmitted power from reflections between to flat surfaces that cause interference. We could not get rid of all of the flat windows in our setup with the use of the $\sim$30 cm long vapor cell. We did estimate, with the knowledge of the window thickness of 1.2 mm, that any sinusoidal variation due to the etalon effects would be on the order of 80 GHz. Therefore as long as we were in the middle of the range the signal would be mostly a straight sloped line. We found that as long as the background transmitted power was not a curve, we could add a term to the fitting function, Equation A.11, that could account for a sloped line in the form of $y = mx + b$. We did explore options of accounting for a curve in the background of the fit but found that the fitting process failed. Therefore we did our best to ensure we were never near the minimum/maximum of the sinusoidal etalon effect were it was curved, and if we did not notice it until after the experiment was done we added the etalon uncertainty in quadrature to the Υ^{λ} value uncertainty. It was often hard to notice slight curves for any

particularly deep absorption curve that could mask a slight curve in the un-absorbed signal, which we only saw when we fit the absorption curve and saw a clear curve in the residual. For the few curves where it was significant, we ended up correcting the Υ^{λ} value for the run by the estimated amount of the height change due to the curve, and adding double the correction as the uncertainty of the etalon effect.

After we analyzed the data, we also observed that each run was affected by our uncertainty in the total offset and etalon effects. We estimated each effect as a change in the amount of offset we subtract as both effects would be able to change the apparent depth of the absorption curve by subtracting or adding too much signal between the minimum of the curve and zero signal. We found that a 1 mV change in the offset level would effect Υ^{λ} by 0.1% for the 456 nm laser, 0.3% for the 894 nm laser, and 0.05% for the 459 nm laser. For each run we estimate any possible height change in the absorption curve by observing the residual and estimating the change in height of the curve. For the R_1 measurement, we estimated the uncertainty in our total offset was about 0.5 mV for an added uncertainty of 0.15% for the 894 nm curves and 0.05% for the 456 nm curves. For the R_2 measurement, we estimated the uncertainty in the total offset at about 1 mV, for an added uncertainty of 0.05% uncertainty in the 459 nm curves and a 0.1% uncertainty in the 456 nm curves. The uncertainty for R_1 is less for the total offset due to the fact that the increased uncertainty in the 894 nm laser curves caused us to measure the individual offset for each measurement run while the effect for the 450 nm curves was small enough we only measured the background a couple of times per day.

We then take the average of Υ^{λ} and its uncertainty for each measurement run and then plot it. We show plots of the different Υ^{λ} plotted against each other for R_1 in Figure A.9 and for R_2 in Figure A.10. An individual data point in either of the plots is the average of the y-axis and x-axis Υ^{λ} value from the same measurement. The data point at zero is from our measurement with no vapor cell in the path. For the fitted line we left both the intercept and slope be free parameters. We verified that the intercept was zero within its uncertainty (or nearly), as large deviations from zero would be indicative of a systematic effect we did not consider. We show the results for the R_1 measurement in Table A.3 and for R_2 in Table A.4. For R_2 we separate our data into three different categories, one set for all

Table A.3. Values for the intercept, slope, and reduced χ_r^2 from the fit to the data in Fig. A.9. These uncertainties are not expanded by $\sqrt{\chi_r^2}$.

Parameter	Value
Intercept	$3.6\ (43) \times 10^{-5}$
Slope	0.016239 (21)
χ_r^2	1.29

Table A.4. Summary of fit results from our data sets of Υ^{459} against Υ^{456}. The listed uncertainties for the slope and intercept are not expanded by $\sqrt{\chi_r^2}$. Data sets 1-2 were collected with the shorter $\sim$ 6 cm cell. Data for set 3 was recorded using the longer $\sim$ 30 cm cell.

Data Set	Intercept	Slope	χ_r^2
Set 1, F=3	$-5.8\ (41) \times 10^{-5}$	0.23380 (29)	1.95
Set 2, F=4	$-2.4\ (42) \times 10^{-5}$	0.23477 (32)	1.95
Set 3, F=3	$-1.4\ (51) \times 10^{-5}$	0.23593 (48)	1.52

of the data taken with the 6 cm vapor cell and starting ground state of F=4, one set for all of the data taken with the 6 cm vapor cell and starting ground state of F=3, and lastly one set for data taken in the 30 cm vapor cell and starting ground state of F=3. We separated the different starting ground state F values as we found slight differences from a magnetic effect depending on the starting F value, discussed in the next section. We also separated the two different vapor cell size data to verify that there was no systematic effect due to any possible difference in the chosen vapor cell.

A.5.4 Systematics

Before we calculate our final values of R_1 and R_2 from the slopes of Figure A.9 and Figure A.10, we investigate the possible effects of different systematic errors and uncertainties on the final value. As stated above, we investigated possible effects of impurities in the vapor cell and potential effects of different temperature/density ranges by using two different vapor cells for the R_2 measurement. We found no significant variation between the two cells. The uncertainties we investigated are summarized below and in Table A.5.

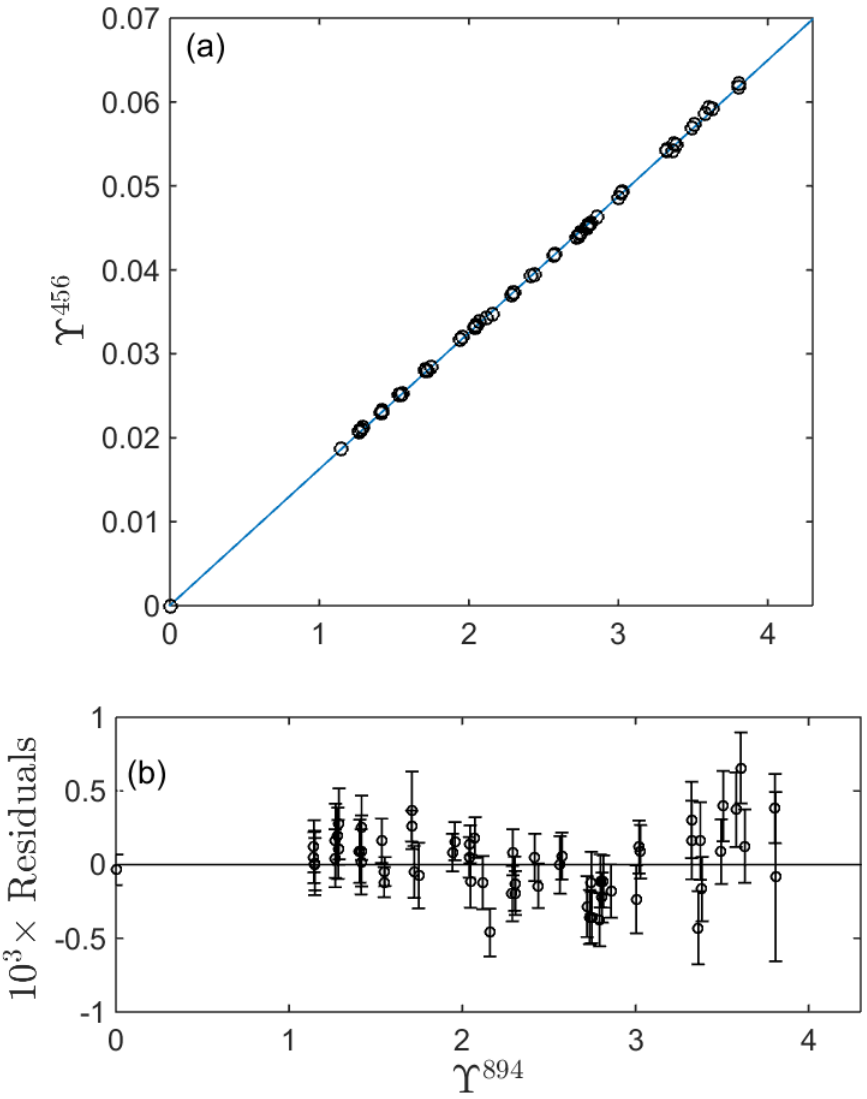

Figure A.9. Plot of Υ^{λ} for the 456 nm and 894 nm lasers against each other for R_1. The x-axis is the Υ^{894}, while the y-axis in (a) is the Υ^{456} and for (b) is the residual between the data point and the fitted line. In (a) the circles are the data points and the blue line is the fitted line. There are error bars on each point, but they are too small to be seen. In (b) we represent the error bar as the combined one sigma uncertainty in Υ^{456} and Υ^{894}.

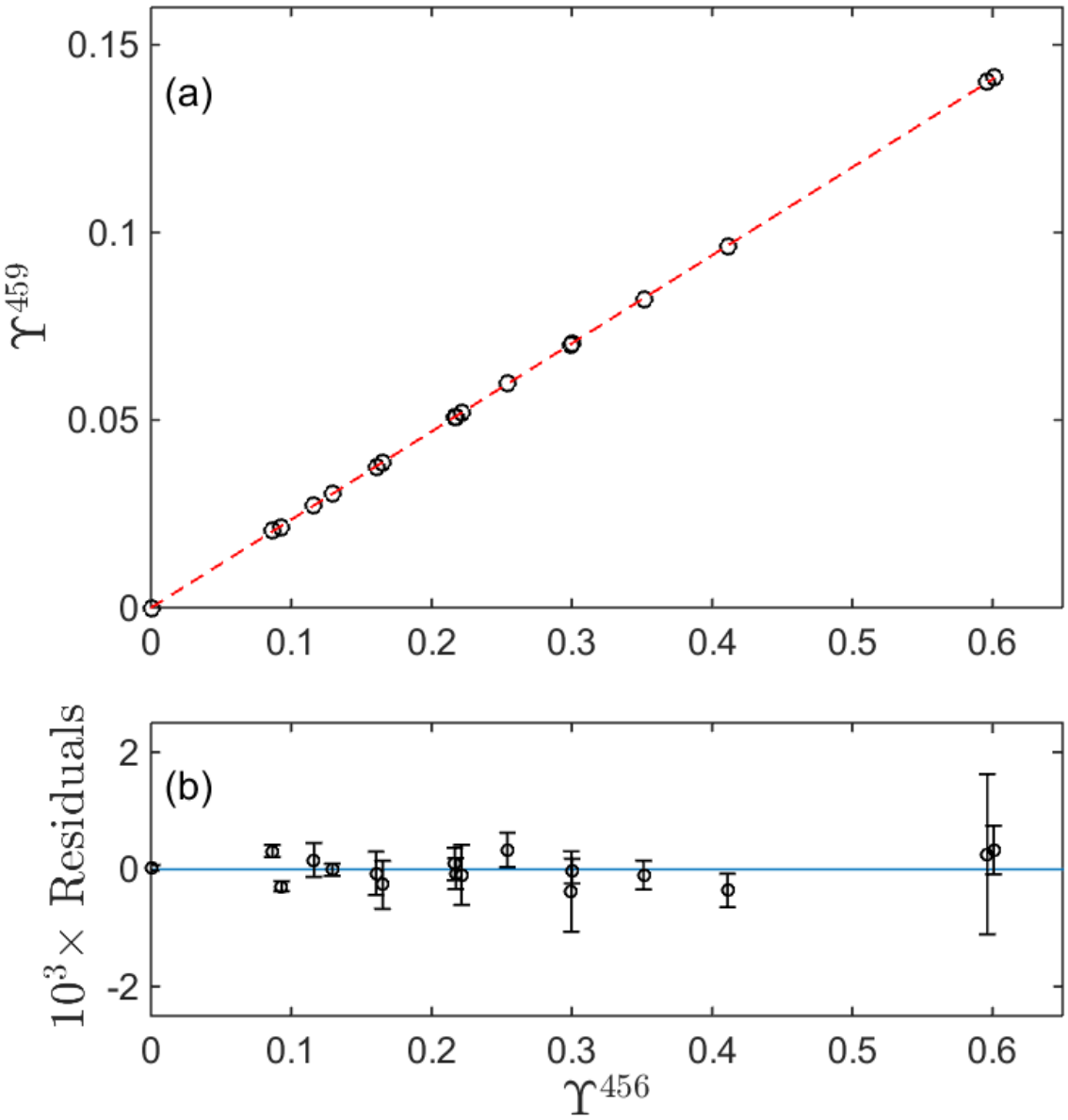

Figure A.10. Plot of Υ^{λ} for the 456 nm and 459 nm lasers against each other for R_2 from data set 2. The x-axis is the Υ^{456}, while the y-axis in (a) is the Υ^{459} and for (b) is the residual between the data point and the fitted line. In (a) the circles are the data points and the dashed red line is the fitted line. There are error bars on each point, but they are too small to be seen. In (b) we represent the error bar as the combined one sigma uncertainty in Υ^{456} and Υ^{459}.

Additionally, we investigated the effects a magnetic field would have on the measurement. We measured a $\sim$ 1 G field at the spot of the 6 cm vapor cell and a $\sim$ 0.5 G field at the 30 cm vapor cell spot. The main contributor of the magnetic field comes from the optical table, so since the 30 cm vapor cell was higher up from the table, due to the length of the cold finger, it's field was less. For a 1 G field, the Zeeman splitting for each hyperfine component is 2 MHz or less. To approximate the effect of Zeeman splitting we added the appropriate Zeeman splitting to each of the individual hyperfine component's natural linewidth (Lorentzian linewidth in the fitting formula Equation A.11). After observing the effect on the spectra and Υ^{λ} value, we calculated the change in R_1 or R_2. We found for the R_2 measurement that the starting F state effected the correction needed. For the F=4 set it changed such that we need to correct R_2 by multiplying by 0.9999 and for the F=3 set we need to correct R_2 by multiplying by 1.0001. For both we estimated an uncertainty due to this correction and effect to be about 0.02%. For the R_1 measurement we found that there was no need for a correction but the uncertainty due to the Zeeman splitting effect was about 0.03%.

We also investigated the impact of our uncertainty of the FSR value of the Fabry-Pérot cavities on the final determination of R_1 and R_2. The change in FSR value affects our frequency scan calibration from the time domain, which affects the value of Υ^{λ}. We find

Table A.5. The percentage uncertainties for the different sources of error for the measurement of R_1 and R_2. The final uncertainty is the individual uncertainties added in quadrature. The 'Fit' uncertainty comes from the fitted value of the slopes of the Υ^{λ} values.

Source	$\sigma_1/R_1(\%)$	$\sigma_2/R_2(\%)$
Fit	0.07	0.09-0.13
Freq. scan calibr.	0.04	0.01
Zeeman	0.03	0.02
Beam overlap	0.01	0.01
Saturation	0.02	0.02
Linewidth	0.02	0.02
Total uncertainty	0.09	0.09-0.13

that the uncertainty in R_2 is small, at most a change of 0.01%, due to the fact that both of the transitions are using the same Fabry-Pérot cavity and both of their Υ^{λ} change at similar rates to any variations in the FSR value. Therefore, since we assume that the FSR should not differ between the 459 nm and 456 nm laser scans, even if the FSR is off it does not heavily effect the value of R_2 since both values of Υ^{λ} are effected at the same rate. The effect is greater for R_1 as the transitions use two different Fabry-Pérot cavities and as such we must account for the whole range of different values of Υ^{λ} for both the 894 nm and 456 nm scans. We found there was no need for a correction but our uncertainty in the final value of R_1 is 0.04% due to our uncertainty in the FSR values and as such the frequency scan calibration uncertainty.

We also had to account for our uncertainty in the linewidth of each of the lasers. We checked for this effect by adding the uncertainty of 200 kHz of the linewidth to the Lorentzian linewidth of all of the hyperfine components. This uncertainty in the laser natural linewidth causes an uncertainty of 0.02% in the final values of R_1 and R_2.

In our experiment we went to great lengths in order to assure ourselves of the fact that both of the laser beam's paths overlapped, such that they passed over the same density of cesium over the same length. The best of our capabilities assured us that they were overlapped to within a change of path length of 0.5 mm. Therefore the uncertainty in the beam's overlap and path is at the 0.02% level. This change in Υ^{λ} causes a beam overlap uncertainty in R_1 and R_2 at the 0.01% level. Additionally, we lowered the power of all of the lasers to avoid the transition saturating. We estimate that the laser intensity we are using, considering the power level and the size of the beam, is less than 2 x 10^{-4} times the saturation intensity for all of the transitions. The effect of the saturation intensity could at most cause a 0.02% effect on both R_1 and R_2, leading us to assign our uncertainty at this value.

To calculate our final uncertainty we add in quadrature all of the systematic uncertainties described above along with our statistical uncertainty from the fitted value of the slopes of the Υ^{λ} values. We then obtain our final values and uncertainties for R_1 and R_2 for each of the sets. The final result for R_1 is $R_1 = 7.8474\,(72)$. For R_2 all of the final values for each set of data are shown in Table A.6 and plotted in Figure A.11. We then take the values of

Table A.6. Values of R_2 after the Zeeman correction with the final uncertainty after including the systematic uncertainties. Data sets 1-2 were collected with the 6 cm cell. Data for set 3 were collected in the 30 cm cell. The χ_r^2 of the weighted mean of the three sets is 4.2 and the weighted mean's error has been expanded by $\sqrt{4.2}$ to help account for the unknown variation effect's source. The individual values and final weighted mean are shown in Fig. A.11.

Data Set	R_2
Set 1, F=3	2.0684 (19)
Set 2, F=4	2.0637 (21)
Set 3, F=3	2.0591 (27)
Weighted Mean	2.0646 (26)

the 3 sets of data for R_2 and calculate the weighted average of the three. Our final value of R_2 is $R_2 = 2.0646\,(26)$.

A.5.5 Matrix Element Values

To first determine the $6s\ ^2S_{1/2} \rightarrow 7p\ ^2P_{3/2}$ transition matrix element value we use the below equation with our newfound knowledge of R_1 and previous knowledge of the value of $\langle 6s_{1/2} \,||\, r \,||\, 6p_{1/2} \rangle$.

$$\langle 6s_{1/2} \,||\, r \,||\, 7p_{3/2} \rangle = \frac{\langle 6s_{1/2} \,||\, r \,||\, 6p_{1/2} \rangle}{R_1} \tag{A.19}$$

Using $R_1 = 7.8474\,(72)$ and $\langle 6s_{1/2} \,||\, r \,||\, 6p_{1/2} \rangle = 4.5057\,(16)\ a_0$, the weighted average of the transition matrix element for the D_1 line from Refs. [88]–[98], our result is

$$\langle 6s_{1/2} \,||\, r \,||\, 7p_{3/2} \rangle = 0.57417\,(57)\ a_0. \tag{A.20}$$

Now that we have obtained the value of the $6s\ ^2S_{1/2} \rightarrow 7p\ ^2P_{3/2}$ transition matrix element, we can then use this value as the reference along with R_2 using the equation:

$$\langle 6s_{1/2} \,||\, r \,||\, 7p_{1/2} \rangle = \frac{\langle 6s_{1/2} \,||\, r \,||\, 7p_{3/2} \rangle}{R_2}. \tag{A.21}$$

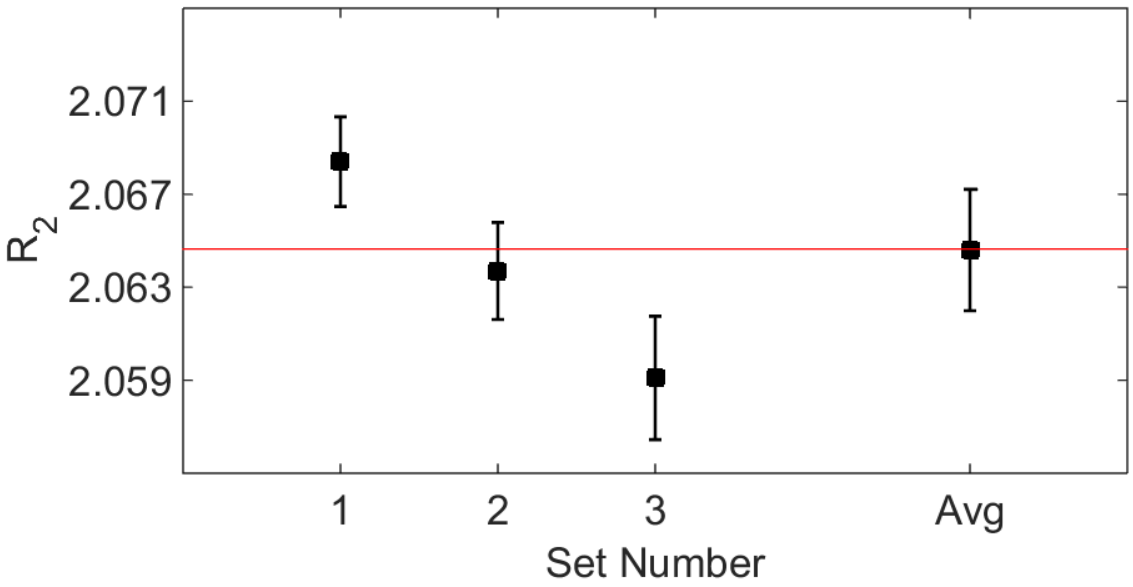

Figure A.11. Plot of different final values the 3 sets of R_2 data. Values found in Table A.6. The final weighted average value's error bars have been increased by the $\sqrt{4.2}$ to account for the variation in the different sets.

We find our final result to be

$$\langle 6s_{1/2} \,||\, r \,||\, 7p_{1/2} \rangle = 0.27810\,(45)\ a_0. \tag{A.22}$$

We compare our results with previous results in Table A.7 for R_1, R_2, $\langle 6s_{1/2} \,||\, r \,||\, 7p_{1/2} \rangle$, and $\langle 6s_{1/2} \,||\, r \,||\, 7p_{3/2} \rangle$. We find reasonable agreement between our values and previous values, as seen in Figure A.12 and Figure A.13. One interesting note is from Ref. [112]. In that work they separate the different methods of calculating the matrix element value and we found that our measurement could distinguish between the single-double (-SD) and scaled (-sc) values. We found that our matrix element values matched up well with the scaled values in comparison to the single double values.

The details of this experiment are written up in Ref. [105].

A.6 Calculating the Vector Polarizability, β

One of the main goals of all the reduced dipole matrix elements is to recalculate β. There are currently two techniques to obtain β. The first one is using the theoretical calculation of the hyperfine changing magnetic dipole amplitude $\mathrm{M1}_{hf}$ from Ref. [117] and an experimental value of $\mathrm{M1}_{hf}/\beta$ from Ref. [118] to find $\beta = 26.957\,(51)\ a_0^3$. This has been the best value until we started measuring more reduced dipole matrix elements to improve the uncertainty on the second method. For the second method one uses a sum-over-states calculation to find the scalar polarizability, α, from all of the reduced dipole matrix element. One can then take a measured value of the ratio α/β (we are currently using the measurement from Ref. [85] but our group is working on another measurement of α/β to verify the results of this method), to obtain $\beta = 27.043\,(36)\ a_0^3$ [103].

Table A.7. Experimental and theoretical results for the reduced dipole matrix elements of the cesium $6s\,^2S_{1/2} \rightarrow 7p\,^2P_J$ transitions. The matrix elements are given as factors of a_0. For Ref. [112], we list both the single-double (-SD) and scaled (-sc) values.

Group	R_1	R_2	$\langle 6s_{1/2} \,\|\| \, r \,\|\| \, 7p_{3/2} \rangle$	$\langle 6s_{1/2} \,\|\| \, r \,\|\| \, 7p_{1/2} \rangle$
Experimental				
Shabanova *et al.*, 1979 [113]	7.76 (14)	2.052 (38)	0.583 (10)	0.2841 (21)
Vasilyev *et al.*, 2002 [87]		2.124 (24)	0.5856 (50)	0.2757 (20)
Antypas and Elliott, 2013 [104]	7.796 (41)	2.072 (12)	0.5780 (7)	0.2789 (16)
Borvák, 2014 [114]		2.0635 (53)	0.5759 (30)	0.2743 (29)
This work	7.8474 (72)	2.0646 (26)	0.57417 (57)	0.27810 (45)
Theoretical				
Dzuba *et al.*, 1989 [115]	7.708	2.12	0.583	0.275
Blundell *et al.*, 1992 [86]	7.83	2.057	0.576	0.280
Safronova *et al.*, 1999 [101]	7.873	2.065	0.576	0.279
Derevianko, 2000 [116]				0.281
Porsev *et al.*, 2010 [58]				0.2769
Safronova *et al.*-SD, 2016 [112]	7.452	2.016	0.601	0.298
Safronova *et al.*-sc, 2016 [112]	7.873	2.065	0.576	0.279
Ginges *et al.*, 2023 [66]	7.848 (15)	2.070 (35)	0.5741 (89)	0.2776 (75)
Dervianko *et al.*, 2023 [69]	7.8832 (278)	2.0727 (132)	0.5704 (19)	0.2752 (18)

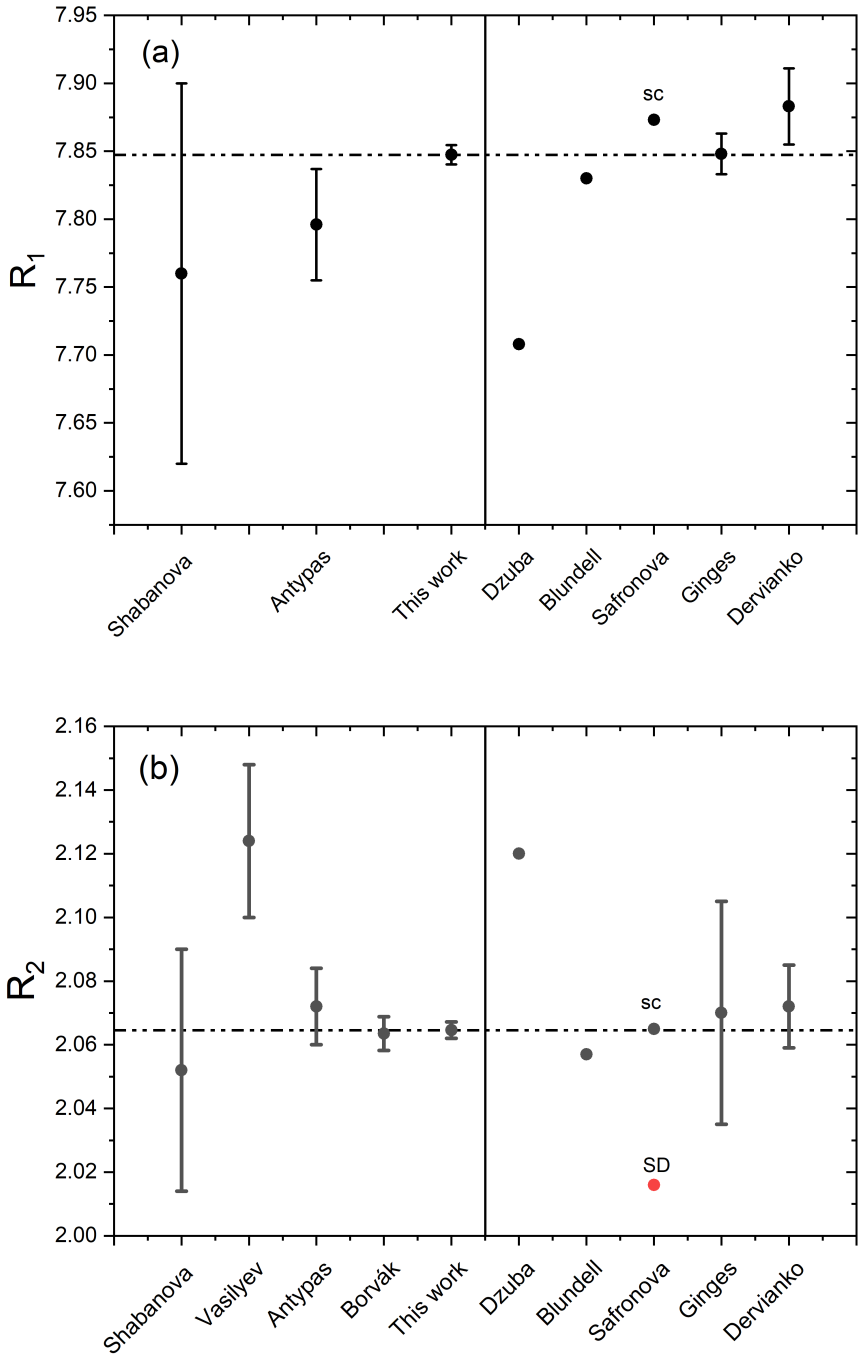

Figure A.12. Comparison of R_1 and R_2 with different experimental and theoretical past results. (a) $R_1 \equiv \langle 6s_{1/2} \,||\, r \,||\, 6p_{1/2}\rangle / \langle 6s_{1/2} \,||\, r \,||\, 7p_{3/2}\rangle$ plot and (b) $R_2 \equiv \langle 6s_{1/2} \,||\, r \,||\, 7p_{3/2}\rangle / \langle 6s_{1/2} \,||\, r \,||\, 7p_{1/2}\rangle$ plot. See Table A.7 for references to these data. Experimental values are on the left, while theoretical values are shown on the right.

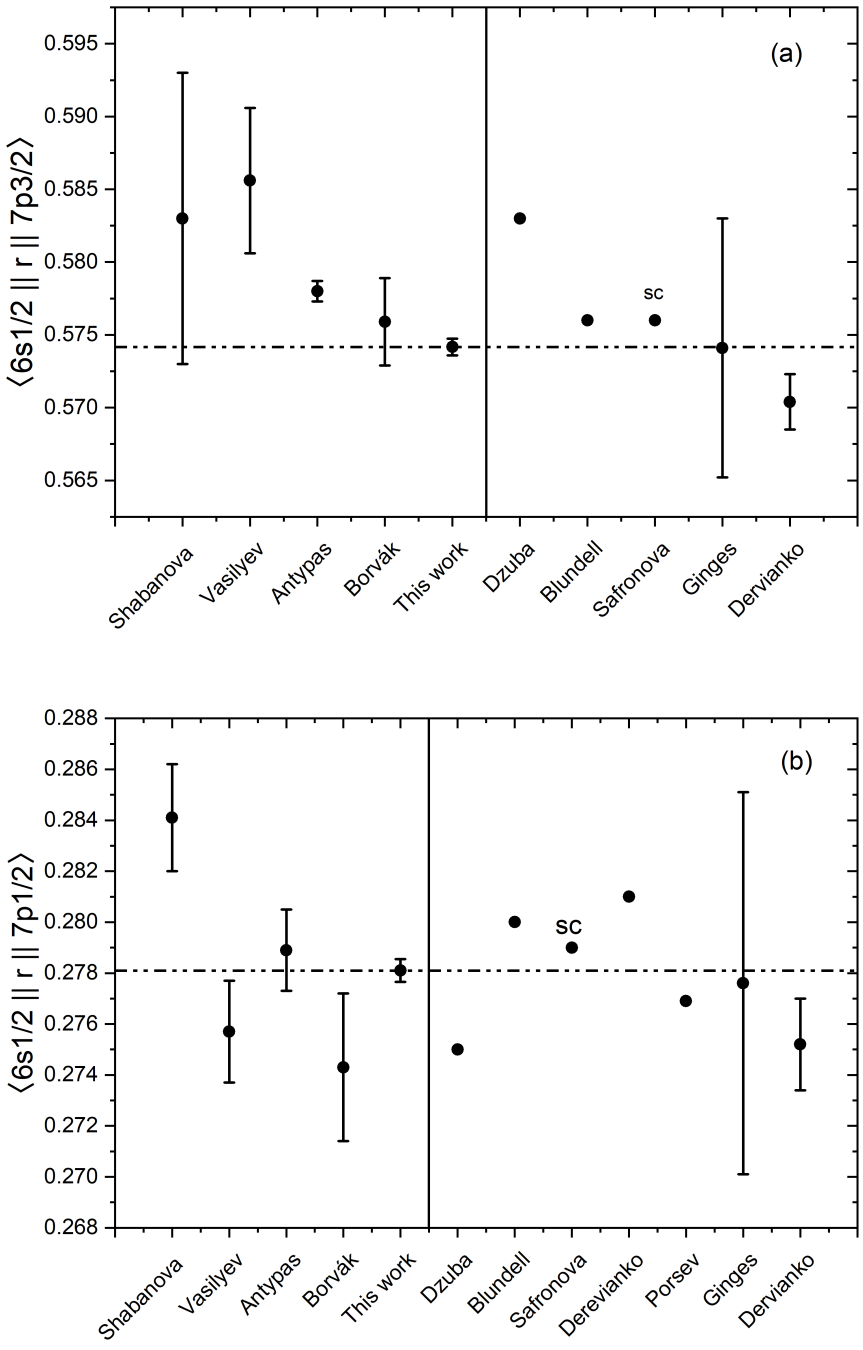

Figure A.13. Comparison of (a) $\langle 6s_{1/2} \parallel r \parallel 7p_{3/2} \rangle$ and (b) $\langle 6s_{1/2} \parallel r \parallel 7p_{1/2} \rangle$, with past theory and experiment. References and values are listed in Table A.7. Experimental values are on the left, while theoretical values are shown on the right. See Table A.7 for references to these data. For Safronova *et al.* (Refs. [101], [112]), we have plotted only the scaled (sc) values as the SD values were off the scale.

B. PREVIOUS RF DESIGNS

B.1 PPTL

Our original design to create a rf field was using a parallel plate transmission line (PPTL). Jungu Choi performed COMSOL simulations to help guide his construction of the PPTL. The two plates used for the PPTL are made out of copper to help support the rf field. He chose the separation between plates and the width of the plates such that the impedance of the transmission line was about 50 Ω. The copper plates are separated by 1 cm, with each having a width of 7.5 cm. In order to support a rf field of $\sim$ 9.2 GHz, we placed reflectors about 11.9 cm apart with radius of curvature at 12 cm. To insert the rf power we used two antennas (fed through transmission lines). The ground shield is soldered to the copper plate, and the center conductor is inserted inside of the PPTL. Using Comsol, Jungu found that the most efficient coupling was when the length of cable inside the PPTL was at 0.5 cm (half the separation distance of the copper plates). We used two input ports to help reduce the effects of loses on the reflection and to optimize the standing wave pattern in the PPTL cavity. A photograph of the finished PPTL, constructed by Jungu Choi, is seen in Fig. B.1.

We characterized the supported frequencies of the PPTL by using a two-port scattering measurement with a vector network analyzer. We can connect both ports of the PPTL and observe the transmission and reflection between the ports. The results of the test are seen in Fig. B.2. There is a clear peak/dip at 9.2 GHz that illustrates that the PPTL supports transmission at 9.2 GHZ, which was the operation frequency of the PPTL.

In order to observe the rf field across the length of the PPTL, we installed it on a translation stage. We used a two inch long, fine adjust motor (Newport Picomotor 8303) to be able to move the PPTL across the atom beam. The motor is able to take steps of 30 nm or less (depending on load size), which gave us fine control over the position of the PPTL. In order to reduce the friction between the PPTL and translation stage, we placed Teflon tape along with Teflon 'bumpers' that help the PPTL move smoothly in the vacuum chamber along with ensuring it moves along a path that is always perpendicular to the atomic beam.

We used the BNC as the source of the rf power for the PPTL. The design to supply rf power to the PPTL was similar to the current design, but slight differnces with the use

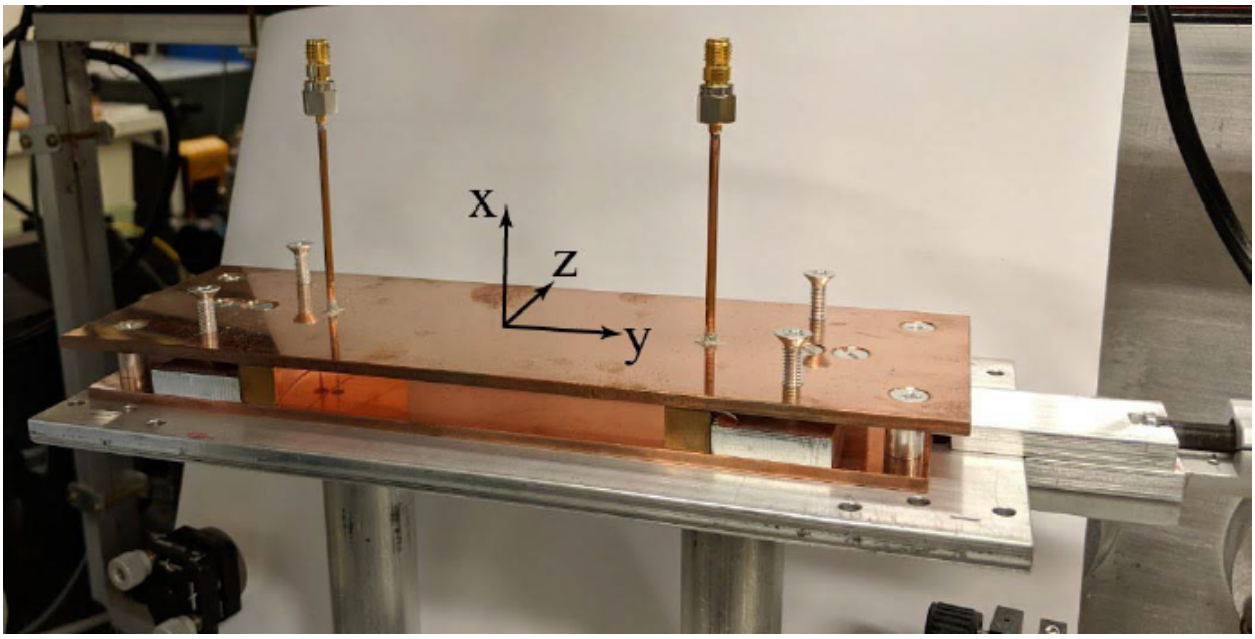

Figure B.1. Picture of our PPTL plate.

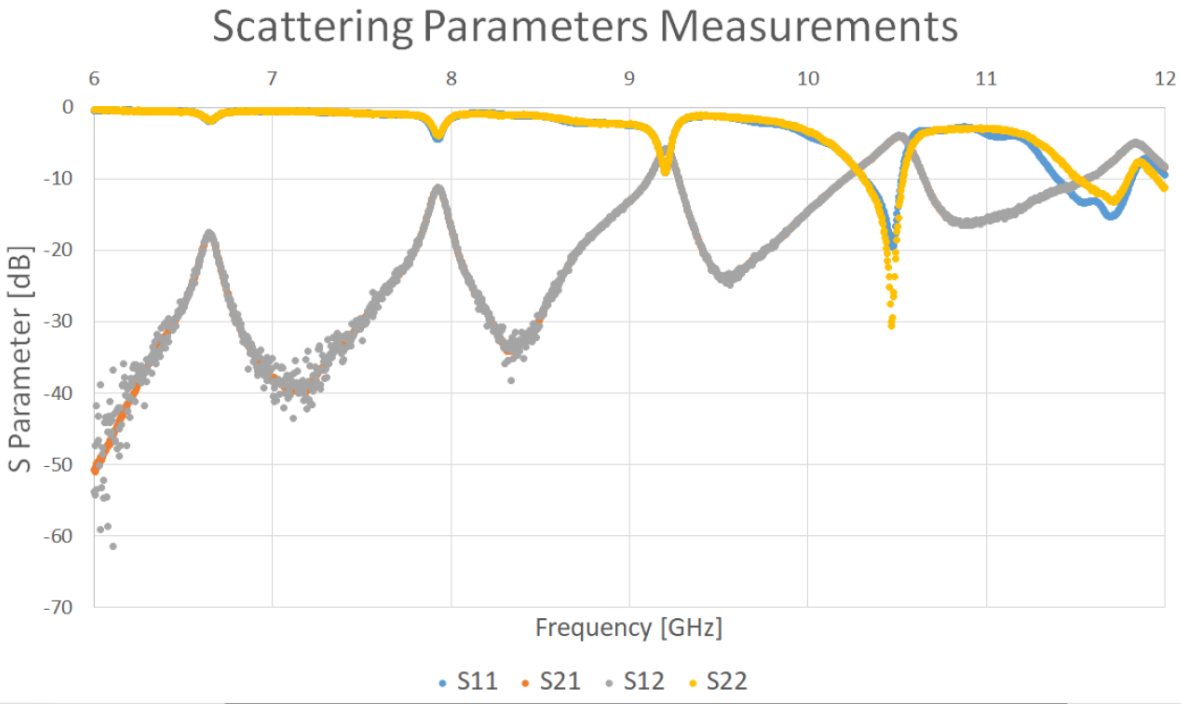

Figure B.2. Two-port scattering parameters of the PPTL. S_{11} and S_{22} are the reflections coefficients between the two ports of the PPTL. S_{12} and S_{21} are the transmission coefficients between the two ports of the PPTL. The peaks in the transmission coefficients and the dips in the reflection coefficients show frequencies that are supported by the cavity.

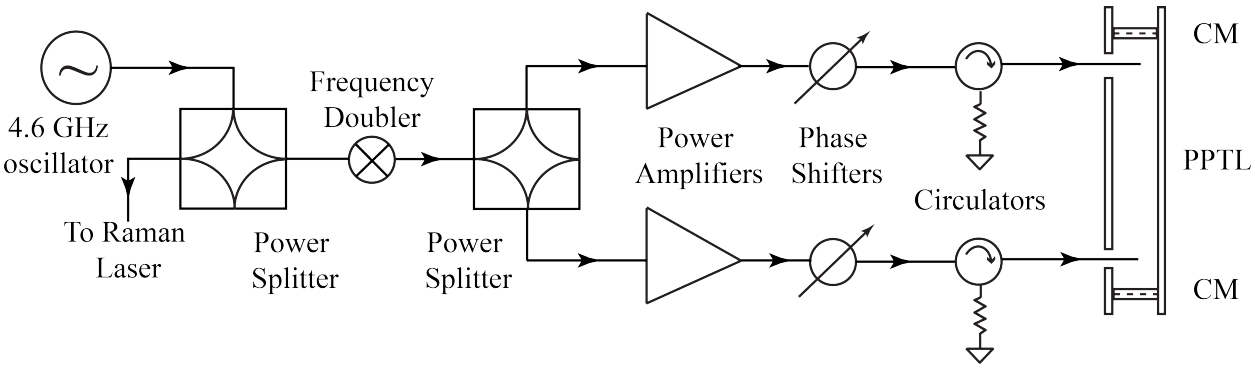

Figure B.3. Diagram of rf power to the PPTL plate.

a power splitter to pick off 4.6 GHz for the Raman lasers (injection locking three lasers together to get the 9.2 GHz splitting), as seen in Fig. B.3, and doubling the frequency to 9.2 GHz to be sent to the PPTL plate. We had phase shifters in the path to give control over the phase difference between the two inputs of the PPTL. This allowed us to optimize the phase difference between the two inputs to have the two incoming rf fields add constructively or destructively at any point in the PPTL cavity, depending on the needs at the time. The circulators act as isolators that allow rf power to the PPTL inputs and stops rf power from going back up. This helped protect the rf equipment, like the rf power amplifiers.

We also investigated the magnetic and electric fields that are created by the PPTL. Comsol simulations were completed by Jungu Choi to investigate how the magnetic and electric rf fields would look in the PPTL, whose results can be seen in Fig. B.4. The fields of interest are the electric rf field, $Re[\epsilon_x^{rf}(y,z)]$, and the magnetic rf fields, $Im[h_y^{rf}(y,z)]$ and $Im[h_z^{rf}(y,z)]$. The electric rf field is responsible for exciting the 6s F=3 and 6s F=4 PNC transition, while the magnetic rf fields are responsible for exciting the M1 transitions. $Im[h_y^{rf}(y,z)]$ will be able to excite $\Delta m = 1$ transitions while $Im[h_z^{rf}(y,z)]$ will be able to excite $\Delta m = 0$. With the application of magnetic fields in the z direction, the different transitions should be separated such that we can observe the transition individually. One of the preliminary experimental results seen in Fig. B.5, show the different appearance of the $\Delta m = 0$ and $\Delta m = 1$ transition peaks. The $\Delta m = 0$ transition peak is a single peak while the $\Delta m = 1$ transition peak has two peaks. The two peaks are due to the fact that

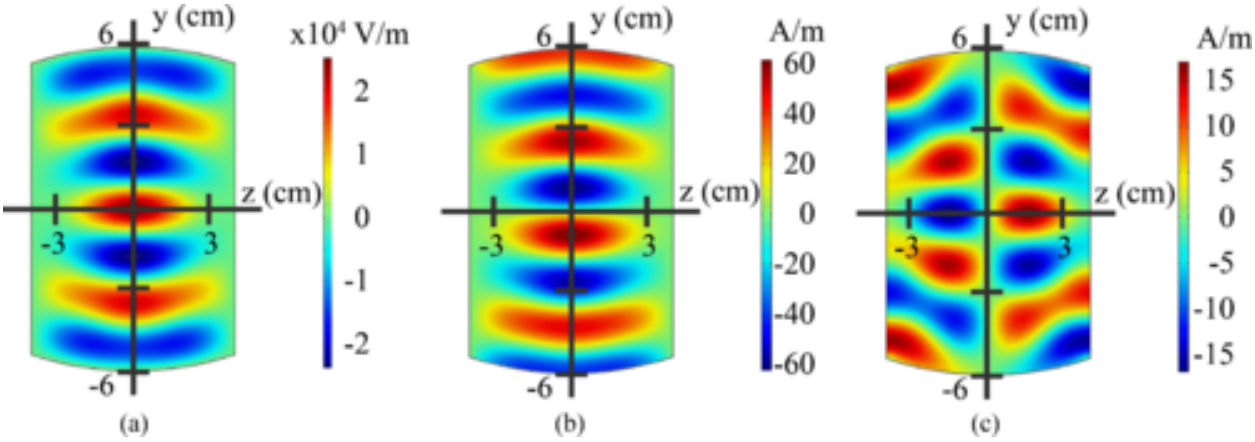

Figure B.4. Gradient maps of the rf electric field (ϵ) and rf magnetic field strength (h) for the lowest order mode supported by the PPTL cavity (a) $Re[\epsilon_x^{rf}(y,z)]$, (b) $Im[h_z^{rf}(y,z)]$, and (c) $Im[h_y^{rf}(y,z)]$.

atoms traveling directly through the node at the exact transition frequency will end up not being excited at all. This is due to the fact that the h_y^{rf} field changes sign from left to right sides of the PPTL, leading to no net interaction at zero detuning. When the rf frequency is detuned from the exact transition frequency, this cancellation is not complete, causing a double-peaked structure. The unique structure of the $\Delta m = 1$ transition peak lead us to an interesting idea to measuring the PNC effect.

Our previous plan to measure the NSD PNC effect was to interfere the PNC interaction with the magnetic dipole interaction (on the $\Delta m = 1$ transition) and Raman interactions. In this case we were planning to take advantage of the magnetic fields created by the rf field and move the PPTL to the anti-node of the electric rf field, seen in Fig. B.4, where z is the direction of the atom beam. Then the magnetic rf field $Im[h_z^{rf}(y,z)]$ causes zero interactions, while the $Im[h_y^{rf}(y,z)]$ will also end up with a net zero interaction due to cancellation of the interaction along the path of the atom beam. If the PPTL is at an angle to the atom beam, there will still be a magnetic rf interaction in the atom beam as the atom beam's path is not straight along the anti-node of the electric rf field.

When we interfere the PNC and M1 interactions we could have observed $E_{PNC}/M1$. Since M1 for the ground state is well known for cesium, we would have been able to obtain

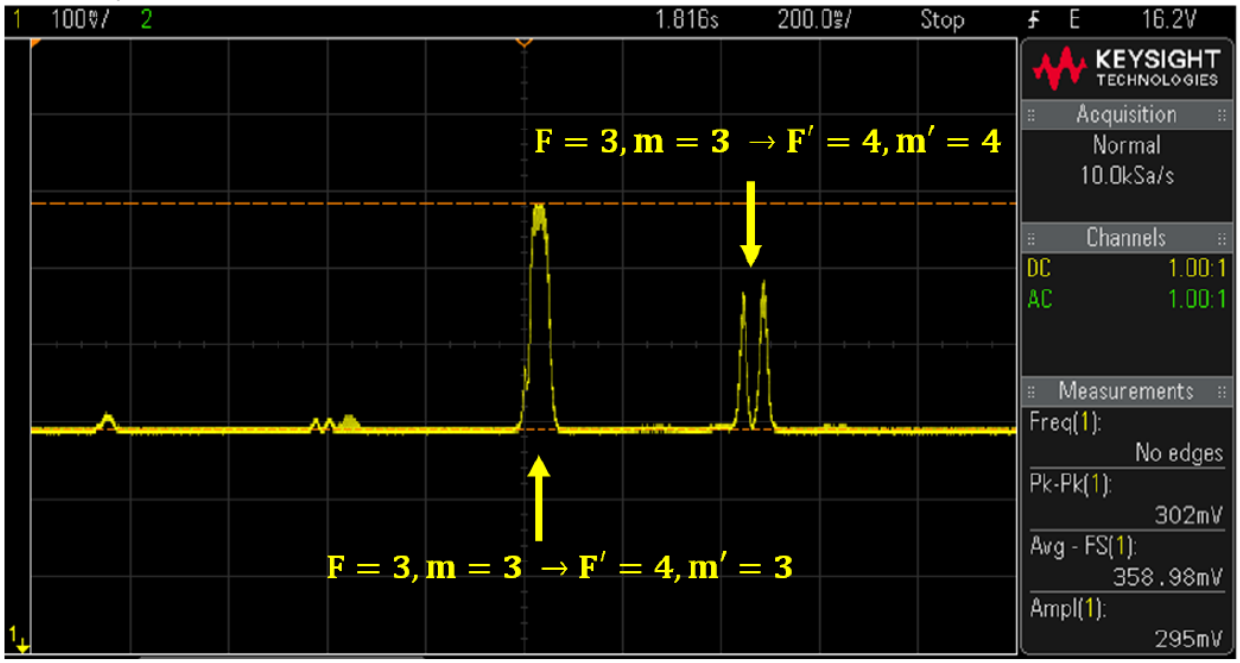

Figure B.5. Experimental examples of a $\Delta m = 1$ and a $\Delta m = 0$ transition. The $\Delta m = 1$ transition shows a double peak structure, while the $\Delta m = 0$ transition shows a single peak. From Ref. [119].

an accurate E_{PNC}. The interference between M1 and PNC would have been explored by varying the rf frequency inputted into the Raman and rf fields near the $\Delta m = 1$ transition. As we change the frequency of the rf source over the $\Delta m = 1$ transition, we would have been able to systematically observe different strengths of the M1 interaction and the PNC interaction. The M1 interaction strength is weakest at the transition frequency with it growing in strength to either side of the frequency. The PNC interaction from the rf field is strongest at the transition frequency, weakening in strength as the frequency goes to either side of the transition. We would similarly use the Raman lasers as the strong transition to interfere with the weak PNC interaction and be able to observe the effects of modulating the phase of the Raman interaction. Using our two-color coherent control technique we should have been able to obtain a high signal-to-noise ratio measurement at each rf frequency to then be able to obtain a result of E_{PNC}. During the course of simulating and experimentally verifying, we found that the sensitivity of the magnetic dipole $\Delta m = 1$ transition, to a small detuning (less than 1 Hz), was such that it completely swamped the PNC amplitude. Additionally, at high rf powers we found a significant leaking of rf power outside of the pptl, allowing for rf power to effect the signal outside of the expected location and pattern of the rf signal we needed. This led us to designing the rf cavity to keep the rf power contained.

B.2 Rectangular RF Cavity Design

Here are more details for the design of the first rf cavity we created.

The final machined the rectangular rf cavity can be seen in Fig. B.6. The science cavity was machined to to 1.990 $\pm$0.0025 cm by 2.800 $\pm$0.0025 cm by 1.80 $\pm$0.01 cm (or 0.783$\pm$0.001 inch by 1.102 $\pm$0.001 inch by 0.709 $\pm$0.005 inch). The other dimensions were only machined to a precision of $\pm$0.005 inch. We chose higher precision for the 1.99 by 2.8 cm box in the science cavity to have better control over the resonance frequency, as these two directions had the biggest impact on the resonant frequency with slight changes in value. We tested the resonant frequency of the cavity using a vector network analyzer. Luckily, on the first try, the resonant frequency of the cavity was 9.186 $\pm$0.001 GHz (the uncertainty is due to the number of points possible over a frequency scan). This is approximately 6 MHz away

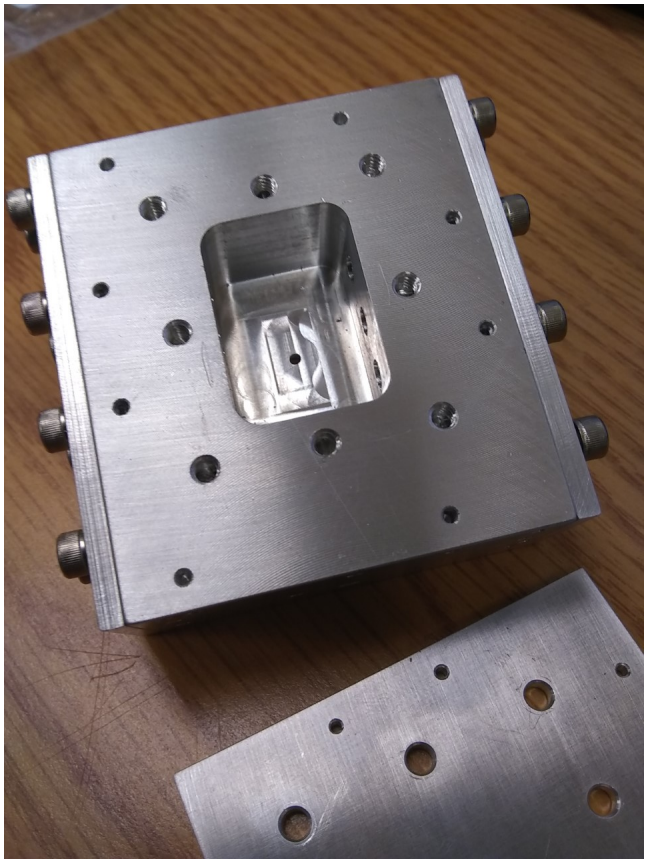

Figure B.6. Machined version of rectangular rf cavity.

from the natural frequency of the ground state hyperfine levels with no magnetic field. This is a reasonable necessary magnetic field to position the wanted $\Delta m = 0$ transition frequency at the resonant frequency. Additionally, 9.186 GHz is the only perceivable resonance peak within the range of 1-15 GHz in the rf cavity, with its full-width have peak at approximately 7 $\pm$2 MHz.

The completed Comsol simulations to investigate how the magnetic and electric rf fields would look and the necessary dimension for the rf cavity can be seen in Figures B.7- B.10. In the Comsol simulations, only one port (the bottom one in the figures) was excited with 1 W of power at a frequency of 9.196 GHz. The 9.196 GHz is near the peak of the resonance for the dimensions of the simulated cavity. The TM_{110} mode is excited, the lowest order mode. The fields of interest are the electric rf field, ϵ_z^{rf}, and the magnetic rf fields, h_x^{rf}, h_y^{rf}, and

h_z^{rf}. The TM_{110} mode in a perfect rectangular cavity, with no holes, will have the fields h_z^{rf}, e_x^{rf}, and e_y^{rf} being exactly zero throughout the whole cavity. The e_z^{rf} field will be non-zero, where in the z-direction it will be a constant value over the cavity height and in the xy-plane the field is maximum at the center of the cavity and zero at the walls. The h_x^{rf} and h_y^{rf} are zero along the z-direction at the center of the cavity, with the maximum on one of the walls. The electric rf field is responsible for exciting the 6s F=3 $\rightarrow$ 6s F=4 PNC transition. h_y^{rf} and h_x^{rf} will be able to excite $\Delta m = 1$ transitions while h_z^{rf} will be able to excite $\Delta m = 0$ transitions (the fields will be able to excite the other transition if the static B field is not purely along the z-axis of the rf cavity and atom beam). With the application of magnetic fields in the z direction, the different transitions are separated such that we can observe the transition individually.

In addition, we simulated the effect of a change in the frequency compared to the resonant frequency and found that the effect is well controlled. A figure of the simulation can be seen in Fig. B.11. We found that over a 2 kHz shift, the magnitude of the percentage chance of cesium being excited only changed by about 4%. This was found to be true for just the PNC interaction alone, just the M1 interaction alone, and the two together with varying amounts of M1 in the interaction. The biggest source of concern for this effect comes from the current changing in the B_z field coils for the interaction region.

We decided to stop using this rf cavity after observing the atomic signal, in Fig. B.12. This was the smallest the rf only signal on the $\Delta m = 0$ transition that we could be observe. After looking at how the atomic beam changed with changing magnetic fields and at the h_z^{rf} on the atom beam holes from Comsol, seen in Fig. B.13, we decided the atomic signal must be coming from h_z^{rf} on the atomic beam holes. We found after more Comsol simulations that more symmetry between the shape of the rf cavity and the atom beam hole helped reduce h_z^{rf}. This is why we decided to move to a cylindrical rf cavity, seen in Fig. 3.15.

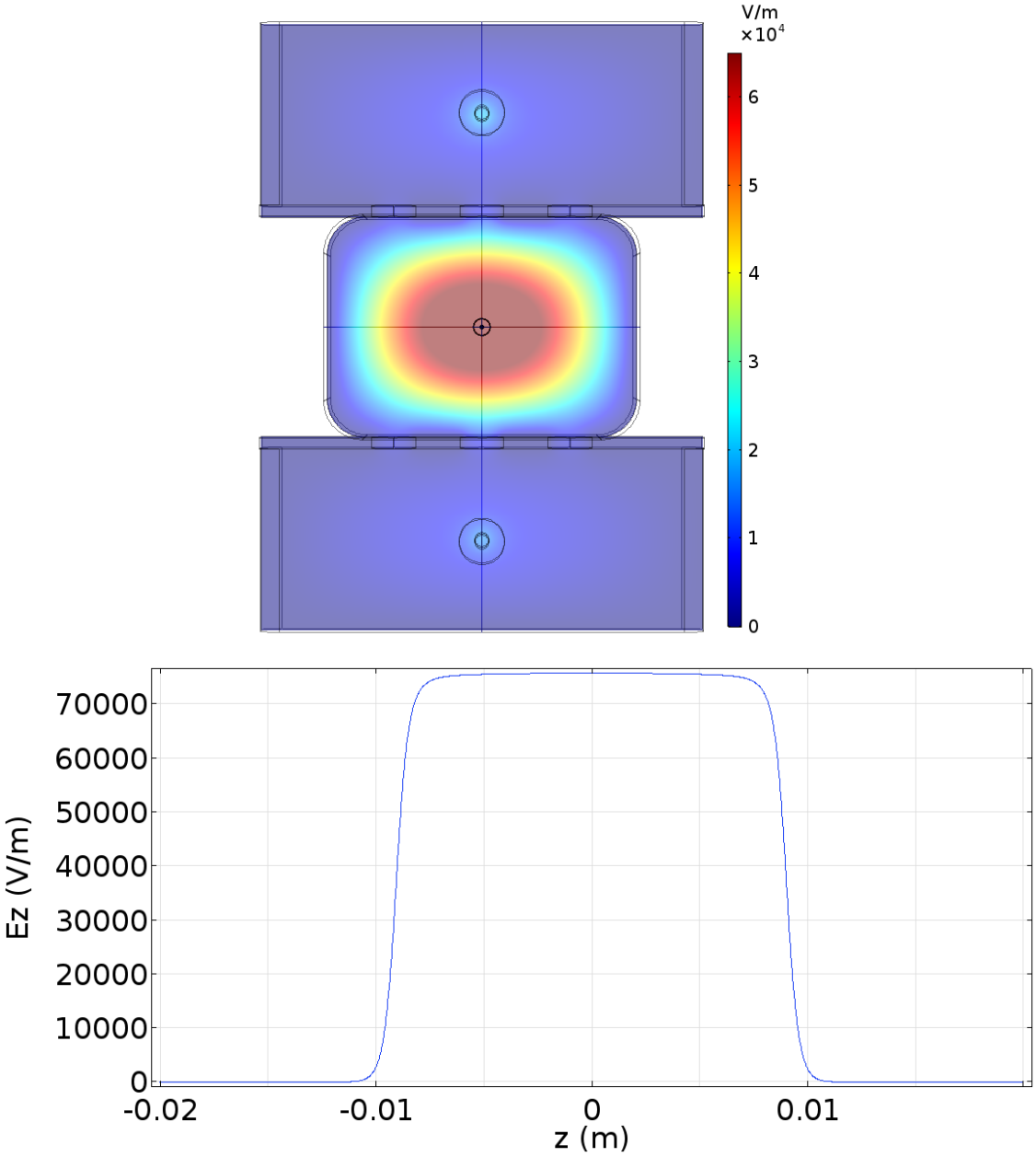

Figure B.7. (a) Gradient map of the magnitude of the rf electric field ϵ_z^{rf} and (b) electric field cut out along atom beam path (out of the page in this picture at the center, marked by two concentric circles).

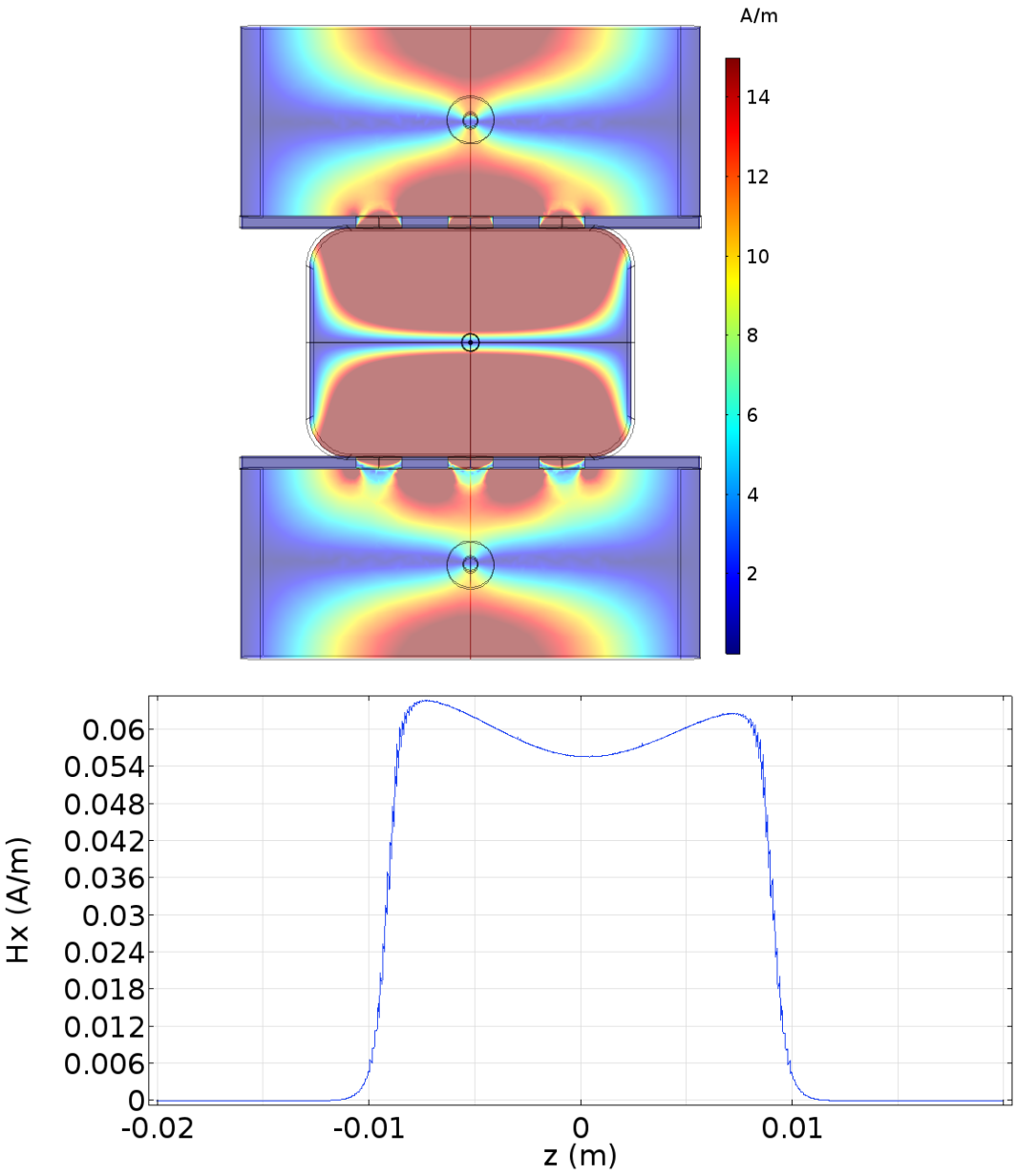

Figure B.8. (a) Gradient map of the magnitude of the rf magnetic field strength of h_x^{rf} for the lowest order mode supported by the rf cavity. The field is small, but not quite zero, along atom beam direction (out of the page in this picture at the center, marked by two concentric circles) and in (b) the field cut along the atom beam path.

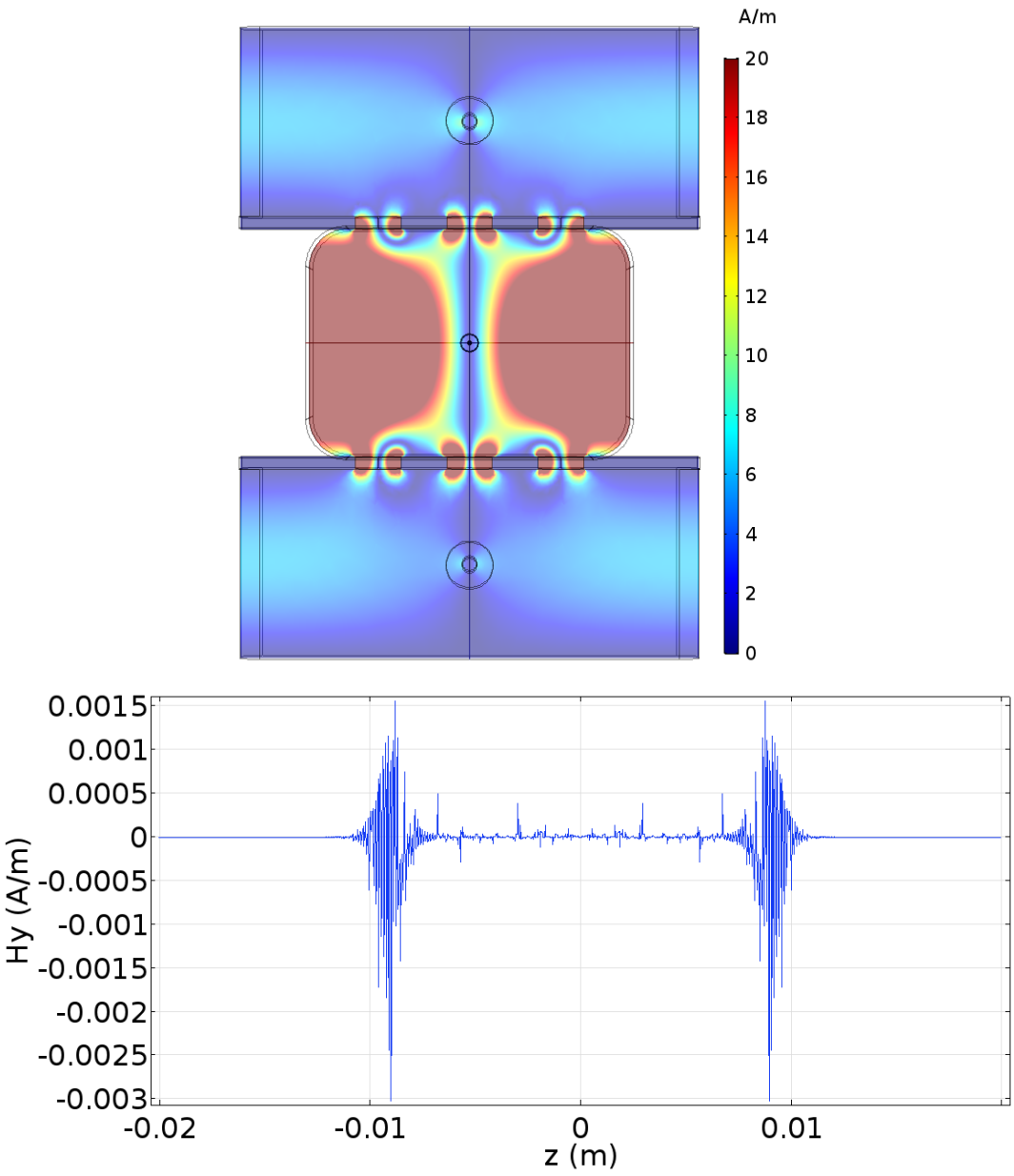

Figure B.9. (a) Gradient map of the magnitude of the rf magnetic field strength of h_y^{rf} for the lowest order mode supported by the rf cavity. The field is very small along atom beam direction (out of the page in this picture at the center, marked by two concentric circles) and in (b) the field cut along the atom beam path. The size of the noise in h_y^{rf} are small in comparison to h_x^{rf} and h_z^{rf}, meaning h_x^{rf} is the biggest possible magnetic field along the center of the atom beam path.

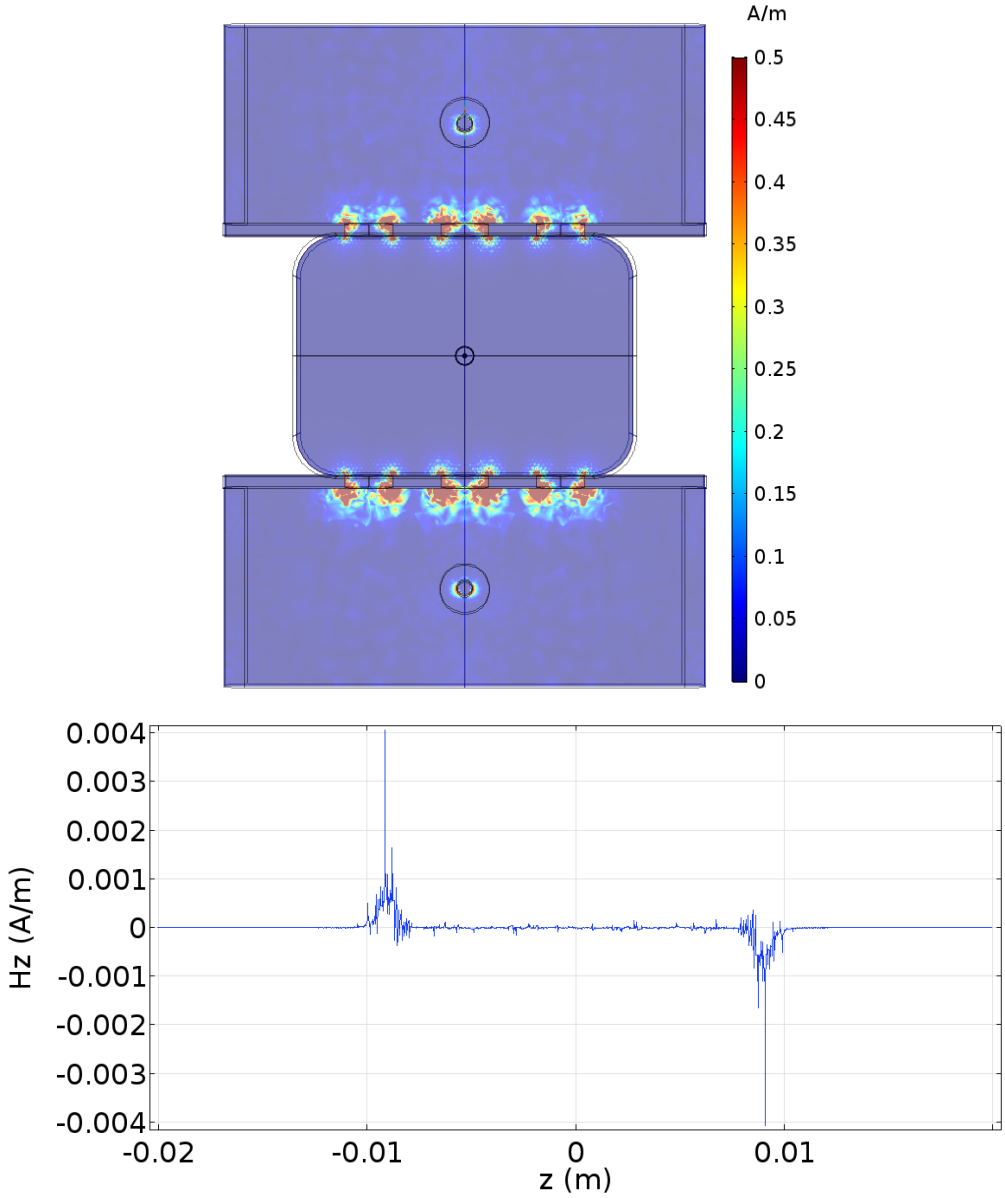

Figure B.10. (a) Gradient map of the magnitude of the rf magnetic field strength of h_z^{rf} for the lowest order mode supported by the rf cavity. The field is zero along atom beam direction (out of the page in this picture at the center, marked by two concentric circles) and in (b) the field cut along the atom beam path. The large peaks are error caused by edges of mesh surfaces. The value of the h_z^{rf} components goes above and below zero such that the sum over the whole length is tiny.

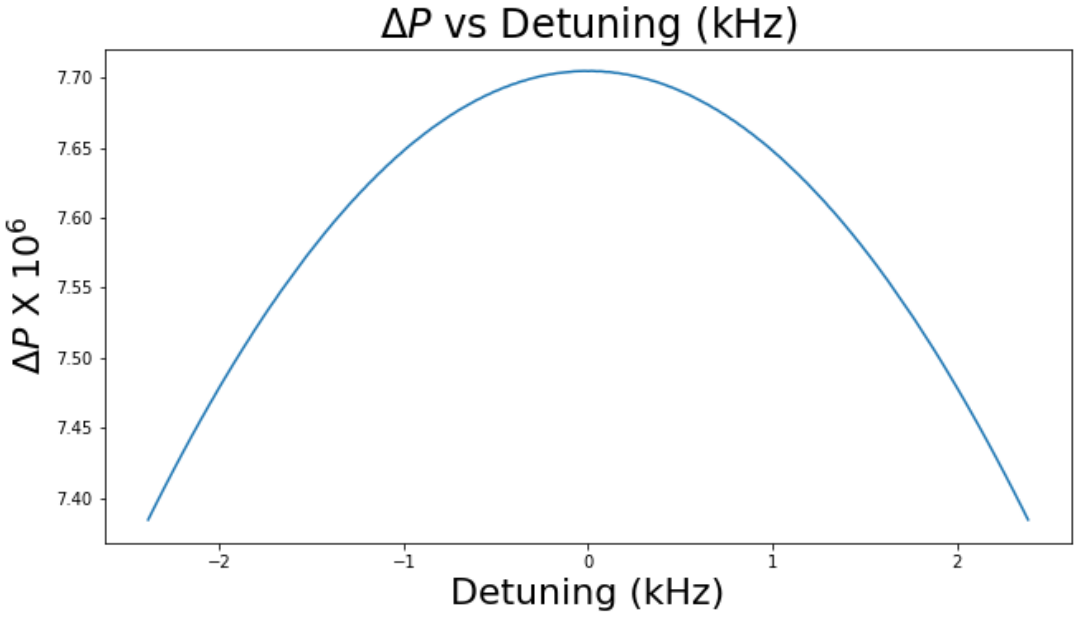

Figure B.11. The change in signal due to the detuning off of the resonant frequency of the transition. The interaction is the PNC interaction along with a 0.1 mrad angle to the static field compared to the atom beam path. The shape is similar for just the PNC interaction alone and the M1 interaction alone. The percentage changed over a 2 kHz shift is about a 4% change in the amplitude of the fraction excited as the phase changes between the Raman and rf interactions.

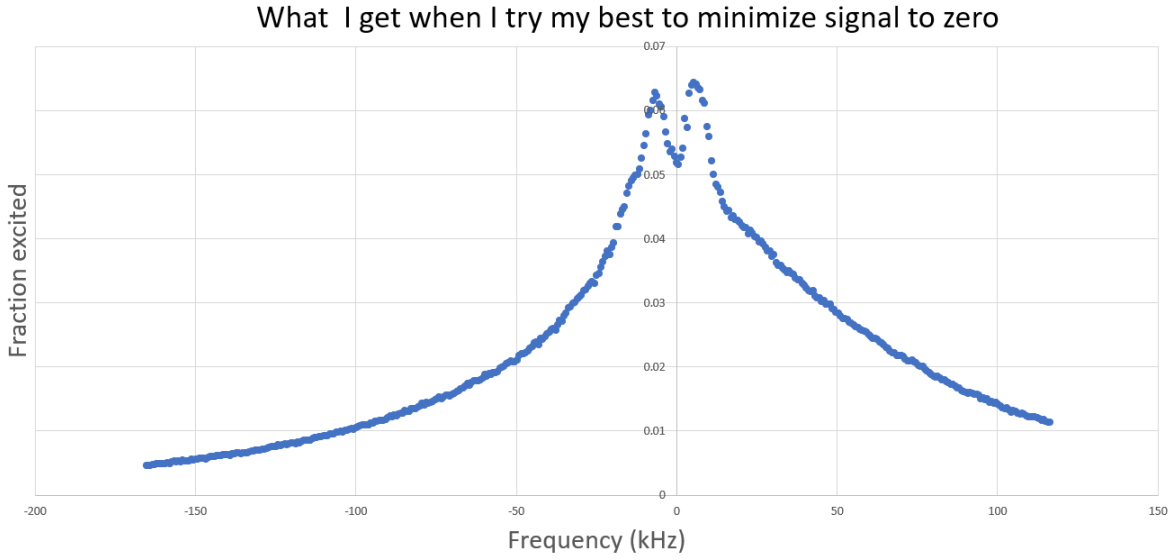

Figure B.12. Experimental atomic signal of the $\Delta m = 0$ transition using the rectangular rf cavity.

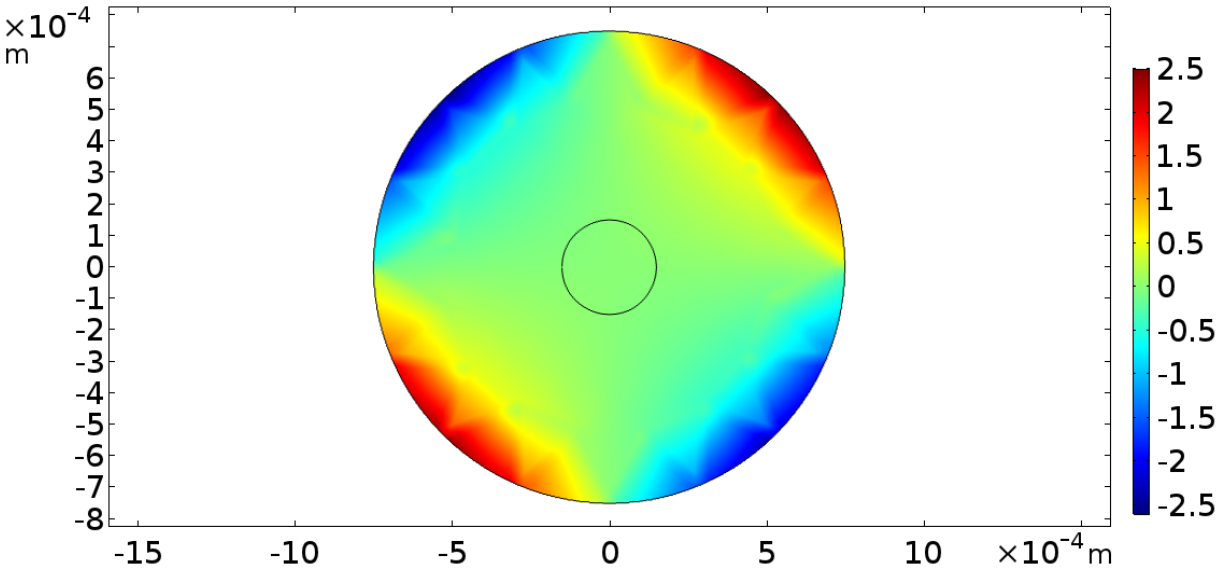

Figure B.13. Comsol simulation of h_z^{rf} on the atom beam opening in (A/m).

VITA

Amy Damitz was born in Winfield Illinois. She attended North Central College for her Bachelor of Science degree in 2015. She then joined Purdue University in Summer 2015 as a graduate student. Her research first began in an ultra-cold molecule lab laser cooling and trapping atoms then transitioned into parity non-conserving atomic research. She received a Masters degree from Purdue University in 2019.

PUBLICATIONS

George Toh, Nathan Chalus, Andrew Burgess, **Amy Damitz**, Poolad Imany, Daniel E. Leaird, Andrew M. Weiner, Carol E. Tanner, and D.S. Elliott, "Measurement of the lifetimes of the $7p^2P_{3/2}$ and $7p^2P_{1/2}$ states of atomic cesium," Phys. Rev. A 100, 052507 (2019).

George Toh, **Amy Damitz**, Carol E. Tanner, W. R. Johnson, and D.S. Elliott, "Determination of the scalar and vector polarizabilities of the cesium $6s^2S_{1/2} \rightarrow 7s^2S_{1/2}$ transition and implications for atomic parity nonconservation," Phys. Rev. L 123, 073002 (2019).

Amy Damitz, George Toh, Eric Putney, Carol E. Tanner, and D.S. Elliott, "Measurement of the radial matrix elements for the $6s^2S_{1/2} \rightarrow 7p^2P_J$ transitions in cesium," Phys. Rev. A 99, 062510 (2019).

George Toh, **Amy Damitz**, Nathan Glotzbach, Jonah Quirk, I. C. Stevenson, J. Choi, M. S. Safronova, and D.S. Elliott, "Electric dipole matrix elements for the $6p^2P_J \rightarrow 7s^2S_{1/2}$ transition in atomic cesium," Phys. Rev. A 99, 032904 (2019).

Jonah Quirk, **Amy Damitz**, Carol Tanner, and D.S. Elliott, "Measurement of the hyperfine coupling constants and absolute energies of the $12s^2S_{1/2}$, $13s^2S_{1/2}$, and $11d^2D_{\mathrm{j}}$ levels in atomic cesium," Phys. Rev. A 105, 022819 (2022).

Jonah A. Quirk, Liam Sherman, **Amy Damitz**, Carol E. Tanner, and D.S. Elliott, "Measurement of the hyperfine coupling constants and absolute energies of the $8p^2P_{1/2}$ and $8p^2P_{3/2}$ levels in atomic cesium," Phys. Rev. A 107, 012807 (2023).

Amy Damitz, Jonah Quirk, Carol Tanner, and D.S. Elliott, "Technique for a direct measurement of the cesium anapole moment using coherent rf and Raman interactions," Phys. Rev. A 109 (3), 032810 (2024).